TECHNISCHE UNIVERSITÄT WIEN

Diplomarbeit

Pulsed-laser growth of In_2O_3 thin films on YSZ(111) substrates

ausgeführt am Institut für Angewandte Physik
der Technischen Universität Wien

unter der Anleitung von
Univ.Prof. Dipl.-Ing. Dr.techn. Ulrike DIEBOLD,
Dr. Michele RIVA
und
Dott.mag. Giada FRANCESCHI

durch

Jakob HOFINGER, BSc.
Matr.Nr.: 01127429

Februar 2018

Kurzfassung

Indium(III)-oxid (In_2O_3) ist ein Halbleiter und zählt zu den transparenten, elektrisch leitfähigen Oxiden (engl. transparent conductive oxides, TCO's). Diese Materialen vereinen die normalerweise konträren Eigenschaften von hoher elektrischer Leitfähigkeit und geringer Absorption von elektromagnetischen Wellen im Bereich des sichtbaren Lichts. Zur Verbesserung der auf In_2O_3 basierenden Technologie ist ein besseres Verständnis der Oberflächeneigenschaften auf atomarer Ebene notwendig, welches durch Untersuchungen an wohldefinierten In_2O_3 Einkristallen erlangt werden kann. Undotierte In_2O_3 Einkristalle sind nicht kommerziell erhältlich und synthetisch gewachsene Kristalle sind normalerweise sehr klein, was den Einsatz von Untersuchungsmethoden bei denen über größere Flächen gemittelt wird, wie zum Beispiel Temperatur-programmierten Desorption (TPD) oder Röntgenphotoelektronenspektroskopie (XPS), einschränkt. Um den Mangel an ausreichend großen In_2O_3 Einkristallen und die damit verbundenen experimentellen Einschränkungen zu beheben, wurden atomar flache, mehrere 100 nm dicke In_2O_3(111) Filme hergestellt. Die Filme wurden mittels Laserdeposition (engl. pulsed laser deposition, PLD) auf Y_2O_3-stabilisierten Zirconia(111) Kristallen aufgewachsen. In dieser Arbeit wurden zuerst die Auswirkung der Parameter während des Laserdepositionsprozesses (Temperatur und Sauerstoffdruck in der Kammer) auf die Oberflächenmorphologie der Filme untersucht. Anschließend wurde die Struktur und chemische Zusammensetzung dieser Filme mittels Elektronen- (RHEED, LEED) und Röntgenbeugung (XRD), XPS, Rasterkraftmikroskopie (engl. atomic force microscopy, AFM) und Rastertunnelmikroskopie (engl. scanning tunneling microscopy, STM) untersucht und charakterisiert. AFM Messungen zeigten Filme mit großen, atomar flachen Terassen ($\sim$ 150 nm) getrennt durch einatomige Stufen. XRD Messungen bestätigten, dass der Film in der kubischen Bixbyite-Struktur kristallisiert und eine vergleichbare kristalline Qualität aufweist wie In_2O_3 Einkristallproben. Der Vergleich von STM Messungen von In_2O_3(111) Film- und Einkristalloberflächen zeigte eine gute Übereinstimmung auf atomarer Ebene. Diese Tatsache bekräftigt die Annahme, dass die In_2O_3(111) Filme das selbe Verhalten aufweisen wie die Oberflächen entsprechender Einkristalle und daher als gleichwertiger Ersatz in künftigen Experimenten verwendet werden können.

Abstract

Indium(III) oxide (In_2O_3) is a wide bandgap semiconductor and belongs to the class of transparent conductive oxides, which combine high electrical conductivity and optical transparency in the visible region. Achieving a better understanding of the atomic-scale surface characteristics by investigating well-defined single-crystal model systems is of paramount importance to optimize the functionality of In_2O_3-based technology. Undoped In_2O_3 single crystals are not commercially available, and synthetically grown ones are usually very small, limiting the investigation by area-averaging techniques such as temperature programmed desorption and X-ray photoelectron spectroscopy (XPS). To compensate for the lack of large In_2O_3 single crystals, we have prepared well-ordered and atomically-flat $In_2O_3(111)$ thin films, with a thickness of few hundreds of nanometres. The films were grown on Y-stabilized zirconia (111) substrates by pulsed laser deposition (PLD). Their structure, chemical composition, and morphology were characterized by electron (RHEED, LEED) and x-ray diffraction (XRD), XPS, atomic-force microscopy (AFM), and scanning tunneling microscopy (STM). By optimizing the growth parameters (temperature and oxygen background pressure) and investigating their effect on the film morphology and structure, we could obtain $In_2O_3(111)$ films exhibiting properties comparable to the best single crystalline samples available. According to AFM measurements after growth, such films exhibit atomically-flat terraces with an average terrace width of $\sim 150\,\mathrm{nm}$, which increases the typical terrace width of an In_2O_3 single crystal by a factor of $3-4$. XRD reveals that the In_2O_3 film adopts the cubic bixbyite structure. The out-of-plane lattice parameter, as well as the typical peak widths, are comparable to those of single-crystalline samples, indicating high crystalline quality. STM investigations show a very good agreement with the STM results of In_2O_3 single crystals, both on the small and on the large scale. The similarity in high resolution STM measurements strongly promotes the use of the grown films as an equivalent replacement of $In_2O_3(111)$ single crystals for different experimental setups.

Contents

1 Introduction

Surface science concerns the physical and chemical phenomena that occur at the interface of two phases. Since the development of Scanning Tunneling Microscopy (STM), Ultra High Vacuum (UHV) and, most recently, Atomic Force Microscopy (AFM), it has become a very popular field of study. Nowadays, it is possible to acquire real space images with atomic resolution and deduce atomic scale properties of solid surfaces of both metallic and insulating materials. In modern technology it is often desirable to minimize the size of components in order to make the final device smaller, lighter, and more powerful. Surfaces play a key role in these processes, because the smaller the solid, the more influence the surface has compared to the bulk. Therefore, it is important to investigate and understand surface properties, which can be considered as the main goal of surface science.

In the beginning, the main interest of surface scientists were metals and semiconductors, but in the last few years there has been a shift towards metal oxides. This arises from the fact that almost every metal surface is oxidized under ambient conditions, which is usually the case in industrial devices. Although materials used in industry are typically polycrystalline materials, the interest in single crystalline surface properties is legitimated due to the fact that these polycrystalline materials typically consist of small crystallites exhibiting predominantly the most stable, low energy surfaces. Due to this fact, most surface scientists work with single crystalline samples, which serve as an ideal model system for polycrystalline materials in industrial applications.

In addition to the fact that metal surfaces under ambient conditions are usually oxidized, metal oxides exhibit extraordinarily versatile properties, which make them interesting for various applications. These versatile properties range from very high or very low electrical conductivity, and interesting magnetic properties, to strong catalytic proper-

ties, to name but a few. One of those highly conductive oxides is indium oxide, which will be introduced in detail in the following section.

1.1 Indium oxide (In_2O_3)

Indium(III)-oxide is a transparent, yellowish chemical compound with interesting electrical and optical properties. The material is a wide band-gap semiconductor with a band gap of approximately 2.9 eV [1] and has applications in many technical fields when it is doped with tin. Sn-doped In_2O_3, indium tin oxide or ITO, belongs to the class of transparent conductive oxides (TCO), which combine the usually disparate properties of high electrical conductivity and optical transparency in the visible regime. Commercially-available ITO usually consists of 90 % In_2O_3 and 10 % SnO_2, exhibiting a resistivity of $< 10^{-5}\,\Omega$cm, which corresponds to an almost metal-like conductivity. Thus, doping with tin results in a carrier concentration of $\sim 10^{21}\,\mathrm{cm}^{-3}$, while maintaining its high transmittance ($\sim 85\,\%$) in the optical regime [2].

ITO is one of the most common TCO's and find applications in many optoelectronic devices, such as flat panel displays, solar cells or organic light emitting diodes [3–5]. Additionally to its use in optoelectronic devices, In_2O_3 is a promising candidate for chemical gas sensing applications, because its conductivity changes significantly depending on the exposure to oxidizing or reducing gases [6–8].
Moreover, recent literature [9] reports that the reverse water gas shift reaction (RWGS), whereby carbon dioxide is reduced to carbon monoxide and water, *i.e.*

$$CO_2 + H_2 \Rightarrow CO + H_2O\,, \tag{1.1}$$

can be catalysed by hydroxylated indium oxide nanocrystals, denoted as $In_2O_{3-x}OH_y[O]_z$, more readily in the light than in the dark. Thus, this material is a suitable photocatalyst for enhancing the conversion rate of the RWGS reaction exploiting solar energy. This is a first step to utilize the waste product CO_2 and reduce it to CO. In combination

with additional appropriate photocatalysts it is possible to further reduce the created CO to produce fuels, such as methane. As discussed in [10], the aim of the investigation is to realize a so called 'artificial leaf' material, which converts light energy in the form of solar photons into chemical energy stored in solar fuels. This technology would turn the greenhouse gas CO_2, the main waste product of common energy production, into a valuable resource, bringing a sustainable carbon-neutral future closer to reality.

Despite ITO's widespread use in industry, surprisingly little is known about its surface properties. This is related to the fact that in industrial devices typically polycrystalline or amorphous films are used. Nevertheless, in many applications the interface to a different material, *e.g.*, an organic layer, or to ambient conditions, plays a key role in the performance of industrial devices. A better understanding of In_2O_3 surface properties, *e.g.*, the geometric arrangement and electronic properties at the surface, the reactivity towards gaseous species, the band alignment and conductivity within heterostructures, can help to further improve the performance of ITO-based technology. Thus, achieving a better understanding of the atomic scale surface characteristics by investigating well-defined single-crystal model systems is of primary importance to optimize the functionality of devices. The most stable facet of the In_2O_3 crystal, the (111) surface, can be considered as such a single crystal model system. Thus, In_2O_3 single crystals recently were used to investigate the precise atomic-scale structure of In_2O_3(111) surfaces by Dr. Margareta Wagner from the surface physics group TU Wien, with focus on the difference between the oxidized and reduced In_2O_3(111) surface [11] as well as the behaviour of adsorbed water or molecules like para-sexiphenyl [12].

Undoped In_2O_3 single crystals are not commercially available, and synthetically grown ones are usually very small, measuring only $1-2\,\mathrm{mm}$ in diameter (see Figure 1.1). While the small size is not critical for scanning probe techniques, area averaging techniques such as temperature programmed desorption (TPD) and X-ray photoelectron spectroscopy (XPS) require larger samples of homogeneous composition for qualitative and quantitative investigations of *e.g.*, the reactivity of the surface and its electronic properties. Hence, the goal of this thesis is to grow several-hundreds-of-nanometres-thick,

well-ordered In_2O_3 films on $5 \times 5\,mm^2$ YSZ(111) substrates, with the aim to provide In_2O_3 samples, which can replace single crystals in different experimental setups. During this thesis the effect of different growth parameters for In_2O_3 growth on YSZ(111) was investigated. Based on these results, it was possible to establish a recipe to produce atomically-flat and well-ordered In_2O_3 thin films. Furthermore, the final films were characterized and compared to a In_2O_3(111) single crystal using various surface- and bulk-sensitive techniques including reflection high-energy electron diffraction (RHEED), low-energy electron diffraction (LEED), X-ray diffraction (XRD), X-ray photoelectron spectroscopy (XPS), atomic force microscopy (AFM) and scanning tunneling microscopy (STM).

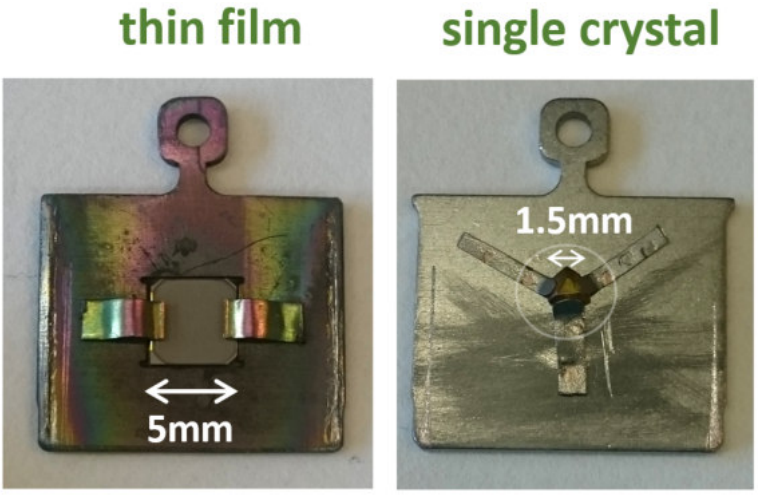

Figure 1.1: Comparison of the size of a In_2O_3 thin film on YSZ(111) (left) with a In_2O_3 single crystal (right), both mounted on a sample plate.

1.1.1 Crystal structure of In_2O_3

In_2O_3 crystallizes with a body-centered cubic lattice in the bixbyite structure under ambient conditons. The indium oxide bulk unit cell has a lattice parameter a of 1.0117 nm [15] and contains 32 In atoms (cations) and 48 O atoms (anions), which sum up to a total of 80 atoms per unit cell, as shown in Figure 1.2 a-b. According to [13], the bixbyite structure has six-fold coordinated cations (large spheres) occupying 8b high-symmetry and 24d sites. In Figure 1.2 a-b, the two different octahedral coordination sites of the

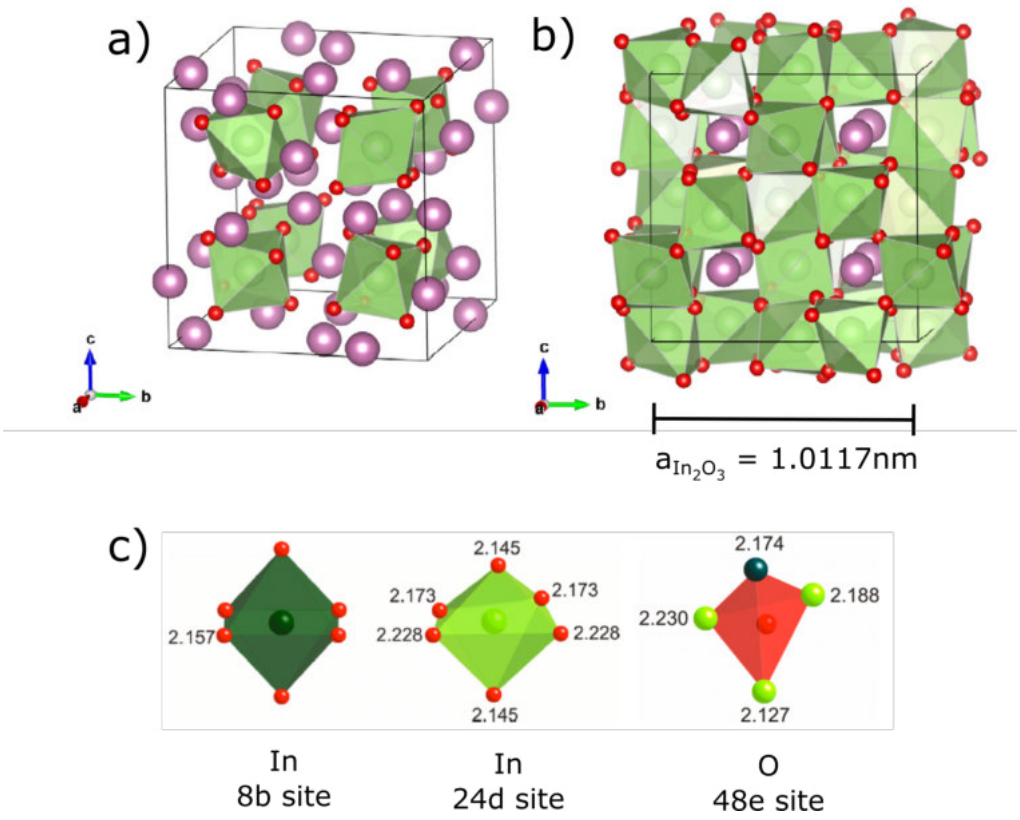

Figure 1.2: Bixbyite unit cell. a) The 8b cation sites are highlighted. They are depicted in the center of the local octahedra, connecting the 6 neighbouring anion sites. b) The 24d sites are highlighted in the same way. c) Overview of In and O sites within the bixbyite unit cell. Illustration of the octahedral In:8b (dark green), the octahedral In:24d (light green) and the tetragonal O:48e sites (red) and their bonding length in Å. Adapted from [13, 14].

cation atoms within the unit cell are highlighted. In Figure 1.2 a the 8b cation sites, and in Figure 1.2 b the 24d sites are highlighted. It should be noted that all the 48 oxygen atoms have the same tetrahedral coordination. A detailed illustration of the three different coordination sites, as well as the bonding length to the neighbouring atoms in Å is provided in Figure 1.2 c. The In:8b site with a more symmetrical octahedral coordination is depicted in dark green, while the In:24d site with highly distorted octahedral coordination is depicted in light green. The O:48e site is indicated as a red tetrahedron. In addition to the cubic bixbyite structure of indium oxide, there is an alternative polymorph at high temperatures and high pressures, which adopts a rhombohedral structure. The rhombohedral phase crystallizes in the same structure as corundum (Al_2O_3) and can be described in terms of a hexagonal cell with $a = b = 5.478\,\text{Å}$ and $c = 14.51\,\text{Å}$ [5].

1.1.2 $In_2O_3(111)$ surface

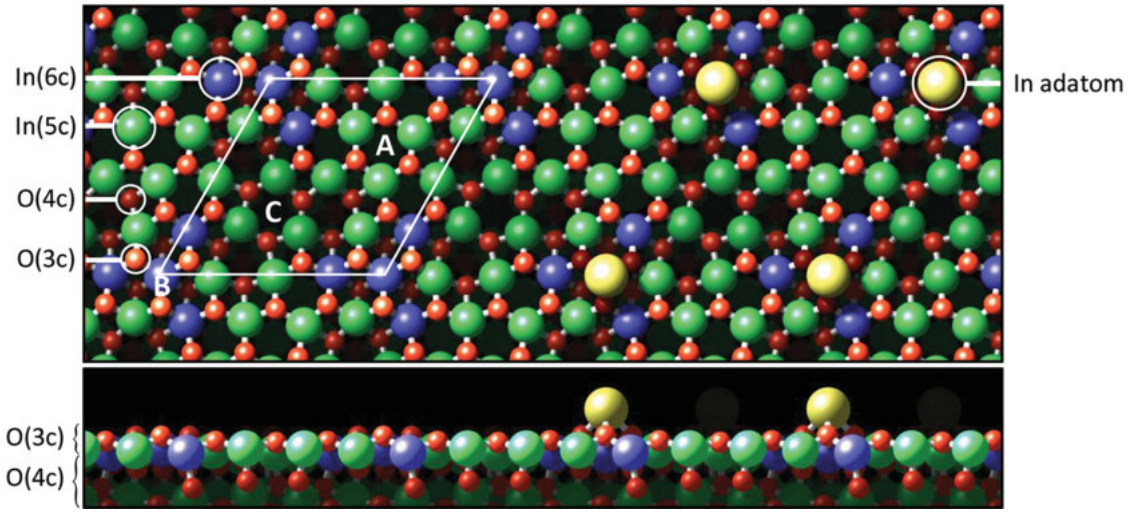

Figure 1.3: Top and side view of the Density Functional Theory (DFT) model of an oxidized (left) and a reduced (right) $In_2O_3(111)$ surface with In adatoms. Atoms are colored according to their coordination, *i.e.*, In(6c) is blue, In(5c) green, O(4c) dark red, and O(3c) light red; In adatoms are yellow. The three high-symmetry positions of the surface with a 3-fold rotational symmetry axis, *i.e.*, the center of the In(5c)-O(3c) rings, the central In(6c) atom and the center of the In(5c)-O(4c) rings, are labelled by A, B and C, respectively. Reprinted from [11].

The (111) surface is nonpolar and very stable. If one considers the structure as trilayers of alternating In and O layers, it can be characterized as a 'Tasker type 2' surface [16]. The repetition of anionic and cationic layers, with an overall composition of $\{[O^{2-}]_{12}^{24-}[In^{3+}]_{16}^{48+}[O^{2-}]_{12}^{24-}\}$ for each (111) unit cell, leads to charge neutrality and a compensated dipole moment of the O-In-O trilayers. Due to this fact the $In_2O_3(111)$ surface is stable, nonpolar and has the lowest surface energy of all low-index terminations [5]. The relaxed, bulk-terminated $In_2O_3(111)$ surface forms an unreconstructed (1×1) structure with three-fold symmetry and a unit cell containing 40 atoms. The lattice parameter is $p = \sqrt{2}a = 1.431\,\text{nm}$ and the height of one layer is $h = \frac{a}{2\sqrt{3}} = 0.292\,\text{nm}$ [11]. A DFT calculation of the (111) surface unit cell is presented in Figure 1.3 [11] and contains:

- 12 five-fold coordinated In-atoms, In(5c), in green

- 12 three-fold coordinated O-atoms, O(3c), in light red
- 4 six-fold coordinated In-atoms, In(6c), in blue
- 12 four-fold coordinated O-atoms, O(4c), in dark red

Figure 1.4 illustrates STM images of the reduced and oxidized (111) surfaces of a In_2O_3 single crystal, as well as a direct comparison with simulated STM images (bottom), showing a good agreement with the experimental results. The left column of Figure 1.4 shows an STM image and an STM simulation of the oxidized surface. The black triangles in the STM image correspond to the In(6c) atoms, which appear darker than the In(5c) atoms.

The right panel of Figure 1.4 depicts an STM image and an STM simulation of the reduced surface. The bright dot in the middle of each black triangle of the oxidized surface can be identified as a single In adatom sitting in the middle of the In(6c) atoms as reported in [11] and shown in Figure 1.3, above.

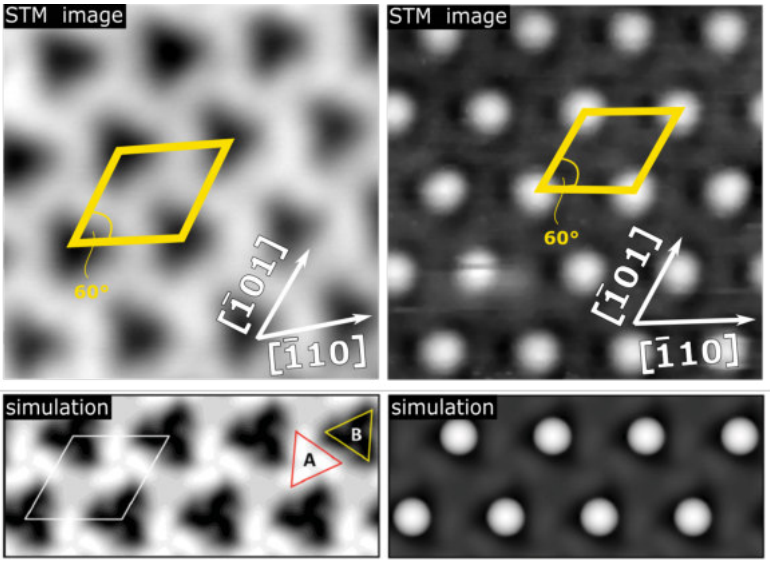

Figure 1.4: (5×5) nm^2 STM image of the oxidized (top left panel) and reduced In_2O_3(111) surface (top right panel). The unit cell of the (111) surface is depicted as a yellow rectangle in both cases. The bottom left image shows an STM simulation of the oxidized surface and the bottom right image shows an STM simulation of the reduced surface with In adatoms. The STM simulations are reprinted from [11].

1.2 Yttria-stabilized zirconia

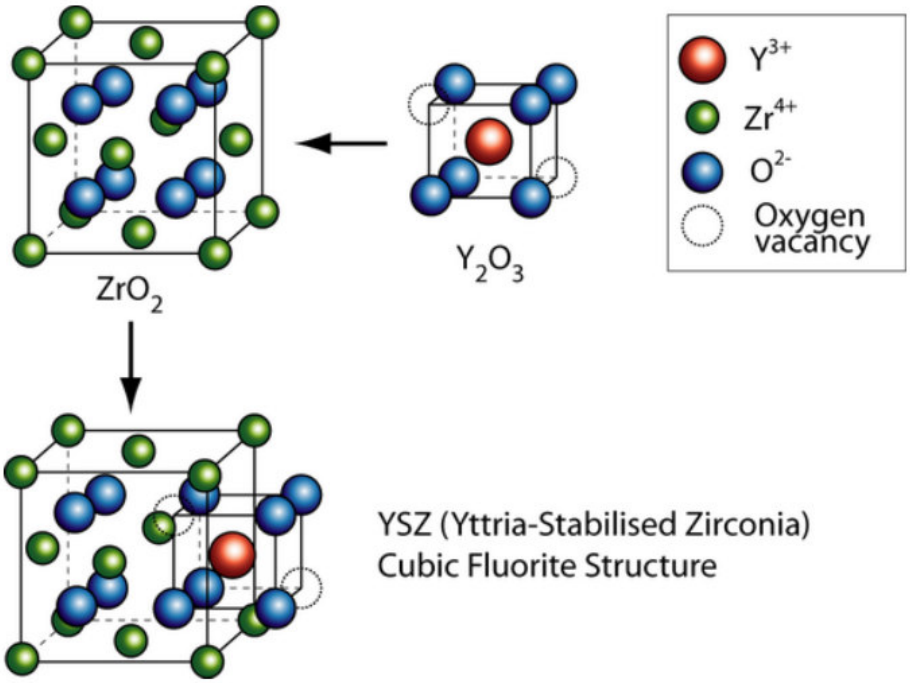

Figure 1.5: Stabilisation of cubic zirconia with yttrium oxide. Unit cells of cubic zirconia, Yttrium(III)oxide and YSZ, with the zirconium and yttrium atoms represented in green and red respectively, while the oxygen atoms are depicted blue. Reprinted from [17].

Yttrium-stabilized zirconia (YSZ) is a ceramic and a good insulator with a band gap of 4.23 eV [18]. Zirconium dioxide (ZrO_2), commonly known as zirconia, exists in three crystallographic phases. Under ambient conditions zirconia crystallizes in the monoclinic phase. Only at higher temperatures the other two polymorphs are adopted. Increasing the temperature above 1170 °C results in a phase transition to a tetragonal structure. Exceeding a temperature of 2370 °C leads to a further phase transition to a cubic structure [19].

The cubic structure can be stabilized at room temperature using Yttrium oxide (Y_2O_3) as a dopant. The replacement of Zr^{4+} ions with the larger Y^{3+} enables the crystallisation in the fluorite (CaF_2) face centered cubic crystal structure with a lattice parameter a = 0.5125 nm. The difference between the In_2O_3 lattice parameter $a_{In_2O_3}$ = 1.0117 nm [5] and the doubled lattice parameter of the YSZ a_{YSZ} = 2 × 0.5125 nm = 1.0250 nm,

equals Δa = -0.0135 nm. The lattice mismatch is calculated as

$$f = \frac{a_{\text{film}} - a_{\text{substrate}}}{a_{\text{substrate}}} = \frac{\Delta a}{a_{\text{YSZ}}}. \tag{1.2}$$

Due to a slightly bigger substrate lattice parameter, the In_2O_3 film is under tensile stress, and the lattice mismatch equals to $f = -1.3\%$, which makes YSZ an ideal substrate for epitaxial growth of In_2O_3. The YSZ(111) substrates used in this thesis where bought from CrysTec GmbH and nominally doped with 9.5 mol% of Y_2O_3 (Y0.19Zr0.81O2). The size of the samples was $5 \times 5 \times 0.5\,\text{mm}^3$ with a miscut angle of less then 0.3°. The preparation of the YSZ substrates is discussed in detail in Chapter 4.1.

2 Physical background

In order to facilitate the discussion of the following chapters, a brief introduction of the relevant physical basics is given in the following.

2.1 Thin film growth

Since one of the main aspects of this thesis is focused on In_2O_3 thin film growth, the following section should be considered as a general introduction to the basic principles and theoretical approaches of thin film growth.
In the literature [20], *epitaxy* is referred to as the growth of a crystalline film on a single-crystal substrate. Depending on whether the substrate and film material is identical or not, it is referred to as *homoepitay* or *heteroepitaxy*, respectively. In order to describe the processes within thin film growth, one has to take into account the thermodynamics, as well as the kinetics of the regarded system. A simple thermodynamic approach provides a fundamental picture of the general trends in film growth. As the name suggests, this approach covers the basic thermodynamic aspects of crystal growth, containing, *e.g.*, the interplay of relative surface energies and interfacial energies.
The kinetic approach takes into account the highly non-equilibrium conditions during thin film growth that can occur in physical vapour deposition methods such as pulsed laser deposition (PLD). To adequately describe the physical processes occurring during growth, a combination of both approaches has to be considered. The theoretical description of thin film growth can be used to explain the occurring growth modes and, thus, the structure and morphology of the grown films.

2.1.1 Thermodynamic approach

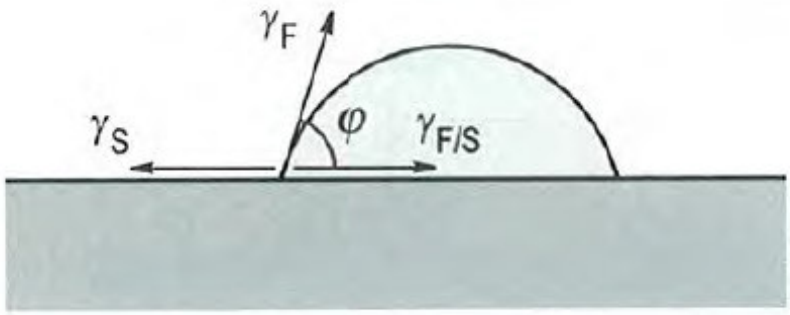

Figure 2.1: Schematic of a film island on a substrate. The surface energies $\gamma_S, \gamma_{S/F}$ and γ_F are defined in the text. Balancing the depicted forces yields to Equation 2.1. Reprinted from [20].

In simplified terms, a consideration of surface energies of a film island on a substrate can be described in a similar way to the appearance of a water droplet on a surface. Depending on the involved surface energies of surface, water and interface, the water droplet will adopt a certain shape in order to minimize its energy. In contact with an hydrophobic material, the water droplet will try to minimize its energy by minimizing the contact area with the surface. As a result the droplet will adopt a sphere-like shape. Conversely, if the substrate exhibits a more hydrophilic character, the droplet will change its appearance forming a rather flat, pancake-like shape.

The same logics apply to a film island on top of a substrate, as depicted in Figure 2.1. The figure indicates with arrows the different surface energies γ and the wetting angle ϕ of the film island. The actual shape depends on the difference in surface energy of the substrate γ_S, the surface energy of the film γ_F, and the surface energy of the interface between film and substrate $\gamma_{F/S}$. The surface energy γ is defined as the work that must be performed to create a surface of unit area, but can also be considered [20] as a force per unit length of boundary at the contact point of film island and substrate, as depicted in Figure 2.1. Therefore, it is possible to define a force equilibrium equation as

$$\gamma_S = \gamma_{S/F} + \gamma_F \cos\phi. \tag{2.1}$$

A wetting, or also called contact, angle of $\phi = 0$ is equivalent to a perfect wetting layer, where the surface is covered with a flat layer. This situation leads to the condition

$$\gamma_S \geq \gamma_{S/F} + \gamma_F. \tag{2.2}$$

The opposite situation, which is characterized by a contact angle $\phi > 0$, will be later referred as island growth and requires that

$$\gamma_S < \gamma_{S/F} + \gamma_F. \tag{2.3}$$

These considerations allow to distinguish three principal modes of film growth within the thermodynamic approach:

- *Layer-by-layer* (or *Frank-van der Merve*) growth mode:
  As the name implies, in this growth mode the film grows strictly two-dimensional, forming flat layers, where a new layer starts to grow if and only if the previous layer is completed. From a surface energy perspective, these mode occurs when the sum of the surface energy of the substrate-film interface and the film ($\gamma_{S/F} + \gamma_F$) is lower (energetically more favourable) than the surface energy of the substrate (γ_S), i.e., when Equation 2.2 holds. In other words, to attenuate the effect of the high surface energy of the substrate, during layer-by-layer growth, it is energetically more favourable for the deposited film to completely cover the substrate than to form multilayer islands. The situation for layer-by-layer growth is presented in Figure 2.2 a.

- *Island* (or *Vollmer-Weber*) growth mode:
  This growth mode is characterized by three-dimensional island growth, and it occurs when it is energetically favourable for the deposited film to expose the substrate (see Equation 2.3). In order to maximize the exposed substrate area, the deposited atoms nucleate and form islands on the substrate. Further deposition leads, on the one hand, to the formation of new islands, and, on the other hand, to the expansion of already existing islands in height and lateral dimension, as shown in Figure 2.2 c.

- *Layer-plus-island* (or *Stranski-Krastanov*) growth mode:
  This growth mode can be thought of a combination of the two previously mentioned growth modes. The initial stage of the Stranski-Krastanov growth mode is characterized by the formation of a completed single layer or several complete layers, exhibiting a layer-by-layer growth mode character. In contrast to layer-by-layer growth, the growth mode changes after a critical thickness to a 3D-island growth mode.

  To explain the change in the observed growth mode during layer-plus-island growth, a *heteroepitaxial* growth has to be considered. In *heteroepitaxial* growth the crystal lattice parameter of the substrate and the film material are not necessarily identical. As already discussed in Section 1.2, the lattice mismatch can be calculated using Equation 1.2. For relatively low misfits, a so called pseudomorphic growth is possible, where the lattice of the epitaxial film is deformed to fit the periodicity of the substrate. During this process elastic strain E_ϵ is built up in the film, which increases with each new film layer. At a critical film thickness it will become energetically more favourable to form 3D-like islands than forming another flat layer. This arises from the fact that a 3D-like object allows easier relaxation of the built up stress in comparison to a 2D-layer. Thus, during Stranski-Krastanov growth mode, the growth mode changes form layer-by-layer growth to island growth, if a critical thickness is exceeded. An illustration of the layer-plus-island growth mode is provided in Figure 2.2 b.

It should be emphasised that another possible way to reduce the stress of the deposited film caused by the substrate is to introduce defects to the crystal lattice of the film. As shown in Figure 2.3, at a critical film thickness it is energetically more favourable to release the strain and create a misfit dislocation associated with the energy E_D, than forming a new strained layer. Due to the fact that the strain energy increases with film thickness and the energy of dislocations remains constant, it is possible to observe a transition from strained pseudomorphic growth to a so-called dislocated relaxed growth if a critical film thickness is exceeded.

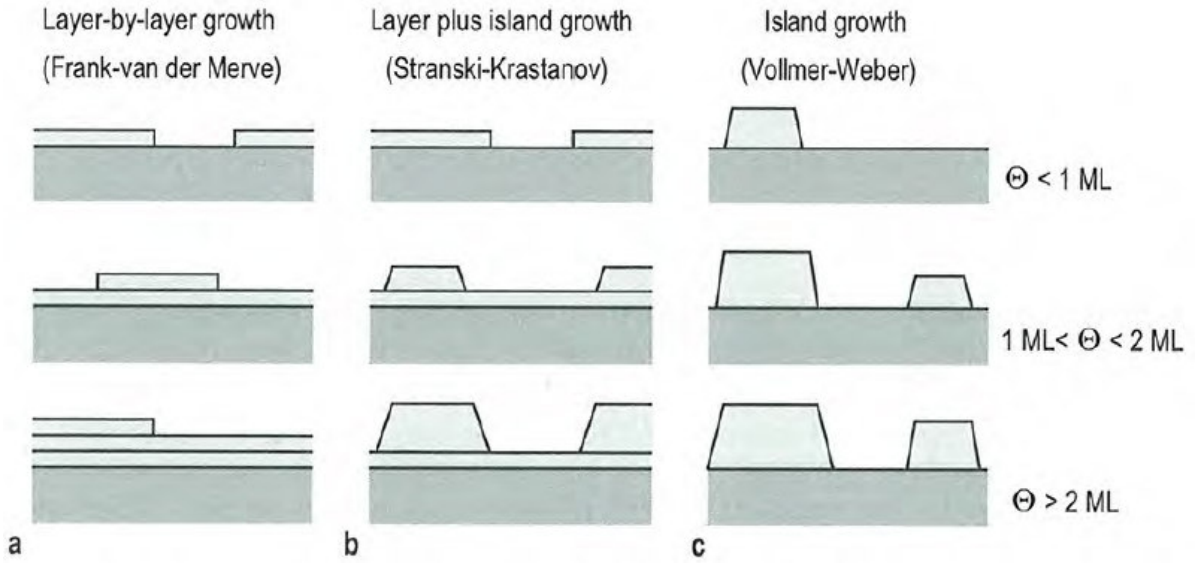

Figure 2.2: Schematic representation of the three main growth modes at thermodynamic equilibrium: a) layer-by-layer growth mode b) layer-plus-island growth mode c) island growth mode. Reprinted from [20].

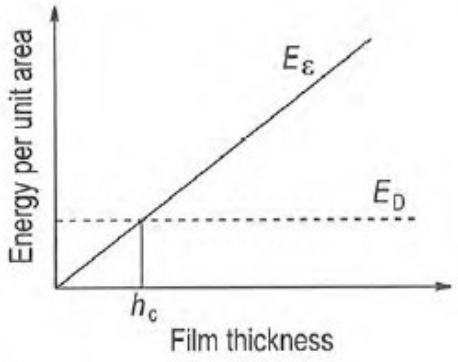

Figure 2.3: Schematic plot of the lattice energy stored in a film per unit area as a function of the film thickness. Reprinted from [20].

2.1.2 Kinetic approach

As already mentioned, a simple thermodynamic description based on the balancing of the free surface energies is not sufficient to identify the growth mode. This arises from the fact that the growth itself is usually a process very far from thermodynamic equilibrium. Thus, a combination of both thermodynamics and kinetics has to be considered. For the sake of simplicity, the kinetic effects on the growth mode are initially presented

in the case of homoepitaxial growth. A thermodynamic consideration of homoepitaxial growth strongly suggests a strict layer-by-layer growth mode. However, due to kinetic limitations, *e.g.*, the mass transport, the observed growth mode can differ significantly from the theoretical prediction. To understand the influence of the kinetics of the deposited species on the growth mode, two main effects have to be considered:

- intralayer mass transport
- interlayer mass transport

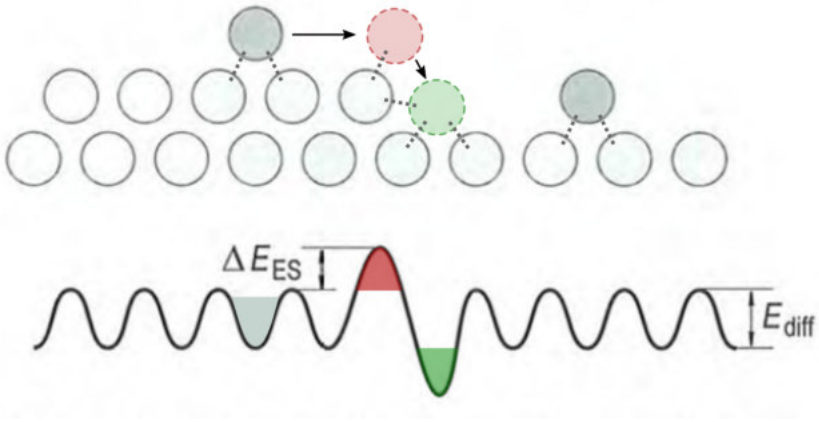

Figure 2.4: Potential energy variations caused by a monoatomic step [20]. The diffusion energy barrier is denoted as E_{diff}, and highlighted in light grey, while the Ehrlich-Schwoebel barrier is denoted as ΔE_{ES}, and highlighted in red. The diffusion process to a lower terrace is indicated with black arrows. The coordination of each specific adatom site is indicated with a dark grey, dashed line. The energetically favourable position at a step edge is highlighted in green.

In the previous considerations the substrate was assumed as a perfectly flat surface, while in the following we will refer to a more realistic situation, where the substrate is considered as a single crystal with single-atomic-step terraces.
Intralayer mass transport refers to the diffusion of deposited atoms along these flat terraces, while interlayer mass transport describes the diffusion of atoms across a step edge. The potential energy curve for an adatom on a single crystal with terraces is sketched in Figure 2.4. The adatom has to overcome a certain energy barrier (E_{diff}) to enable diffusion along the surface. If an adatom on the lower terrace reaches a step edge towards a higher terrace, the step edge position acts as a trap with a local energy minimum.

At the step edge position the adatom has an additional neighbouring atom and can increase its coordination (indicated with three dark grey, dashed lines). Higher coordination is equivalent to an energy decrease and thus stronger bonding, which is highlighted in green in Figure 2.4. Diffusion in the other direction, from a higher to a lower terrace (interlayer mass transport), requires a certain energy to overcome the so-called Ehrlich-Schwoebel barrier (ΔE_{ES}). During the transition from the upper to the lower terrace, as shown in Figure 2.4, the adatom has to temporarily reduce its coordination, which is energetically less favourable. This specific position is indicated with a red circle.

The relative rate of intralayer and interlayer mass transport has a strong influence on the observed growth mode. Depending on the kinetics and the flux of the deposited adatoms one can distinguish the following three situations:

- Step-flow growth
- Layer-by-layer growth
- Multilayer growth

In the simplest case of homoepitaxial growth, conditions close to thermodynamic equilibrium, in particular high kinetic energy and/or a low amount of the deposited species, lead to step-flow growth. High kinetic energy is equivalent to a high degree of surface diffusion, which allows the adatoms to reach the energetically favourable step edge sites. In other words, the average diffusion length of adatoms exceeds the terrace size. Furthermore the low number of deposited atoms in combination with the high surface diffusion prevent the nucleation of clusters on the terraces. The situation for step-flow growth is sketched in Figure 2.5 a.
If the adatom diffusion length is smaller than the average terrace size, the growth will proceed via nucleation of islands/clusters on the terraces. The morphology of these islands can change from monoatomic, 2D-like islands to heigh 3D multilayer islands depending on the adopted growth mode. Flat, 2D-like single-layer islands are characteristic of a layer-by-layer growth mode, while 3D-like islands indicate a multilayer growth mode. The appearance of these islands is governed by the ratio of intralayer *versus*

interlayer mass transport. High interlayer mass transport enhances the formation of flat 2D islands, since the adatoms deposited on top of the island can diffuse across the step edge to the terrace. Due to the predominantly lateral growth of film islands, this growth mode can be considered as layer-by-layer growth as shown in Figure 2.5 b. In contrast, if the interlayer mass transport is low and the mass transport is governed by intralayer diffusion, adatoms impinging on top of the island are not able to overcome the Ehrlich-Schwoebel barrier. Thus, the adatoms cannot diffuse across the step edge and are trapped on top of the island. In this case further growth will lead to the formation of 3D-islands, which can be referred to as multilayer growth as shown in Figure 2.5 c.

Which growth mode is adapted strongly depends on the deposition flux and the sub-

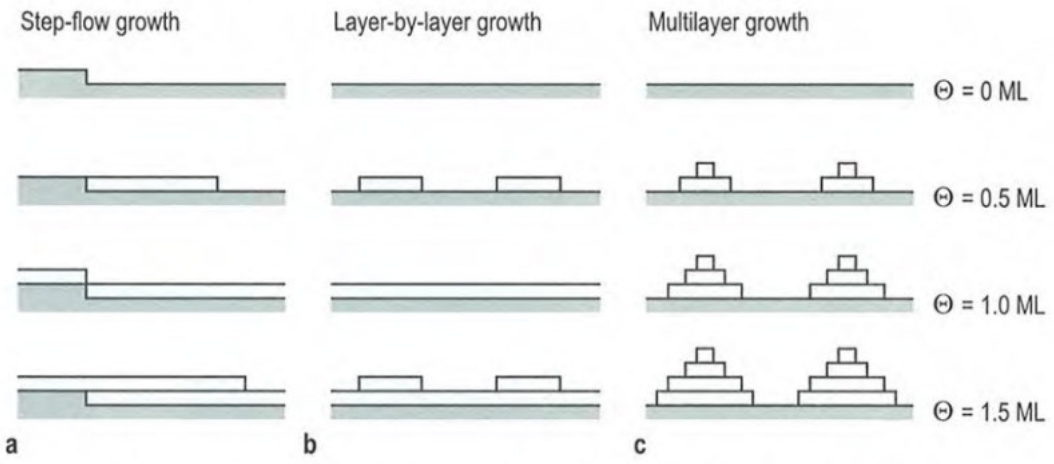

Figure 2.5: Modes of homoepitaxial growth for different coverages Θ a) step flow b) layer-by-layer c) multilayer. Reprinted from [20].

strate temperature. The former affects the rate of deposited adatoms and thus the adatom density on a terrace, while the latter controls the kinetic energy, and thus the surface diffusion of the deposited species on the surface as

$$D = D_0 \exp(-\frac{E_{\mathrm{Diff}}}{k_{\mathrm{b}} T}), \tag{2.4}$$

where D_0 is a prefactor depending on the vibrational frequencies and the lattice parameter, k_{b} is the Boltzmann constant and T is the temperature in Kelvin.

2.2 Diffraction

2.2.1 3D bulk diffraction

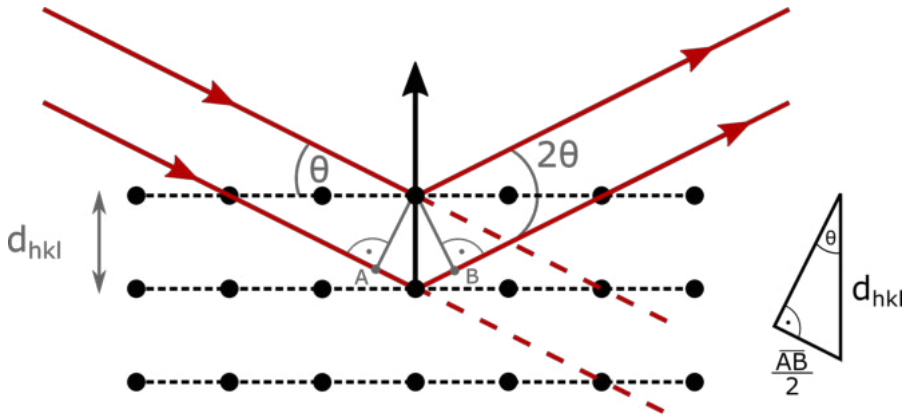

Figure 2.6: Macroscopic view of the diffraction process indicating the pathway difference for two incoming waves reflected at different crystal planes. The small triangle indicates half of the geometrical pathway difference of the two waves. Demanding the pathway difference AB to be a integer multiple of the wavelength results in Bragg's law.

Diffraction experiments of X-rays, electrons, neutrons or atoms can be utilized to investigate real space crystal properties such as lattice structure, lattice constants or surface reconstructions [21, 22]. Using the de Broglie relationship $\lambda = h/|\mathbf{p}|$, where h is Planck's constant, p is the momentum of the particle, and λ is the de Broglie wavelength, one can treat these particles as plane waves with wave vector $|\mathbf{k}| = 2\pi/\lambda$. The observed diffraction patterns provide, *e.g.*, information about the lattice structure or the interplanar distances of the crystal.

A simple way to macroscopically describe crystal diffraction is shown in Figure 2.6. The incoming beam of electrons or photons is reflected at the lattice planes of the crystal, causing the reflected beams to interfere with each other. At certain angles the path length difference $\overline{AB}$ of the reflected beams will be an integer multiple of the wavelength λ, causing the waves to interfere constructively:

$$\overline{AB} = n\lambda. \tag{2.5}$$

A combination of constructive and destructive interference explains the observation of

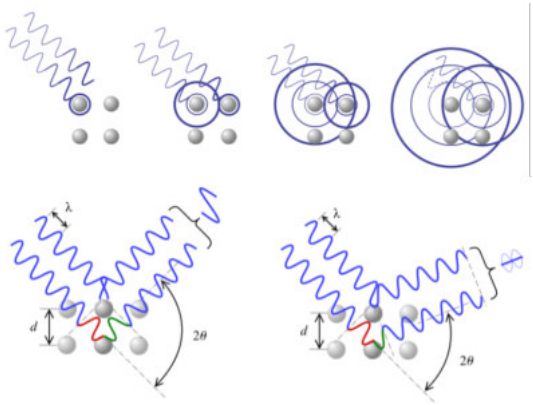

(a) Interference of scattered waves from a crystal lattice. Reprinted from [23].

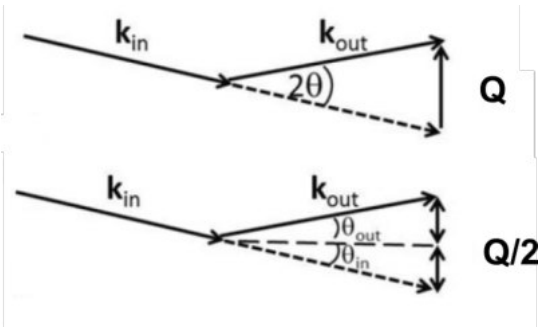

(b) Vectorial sketch of the scattering process in the reciprocal space at a crystal lattice. Reprinted from [24].

Figure 2.7: Microscopic view of the diffraction process.

diffraction patterns with high intensity spots at specific angles, where the condition of constructive interference is fulfilled. This phenomenon is described by Bragg's law [25], which relates the lattice spacing of the crystal with the angle of incidence of the X-ray or electron beam as

$$2\,d_{hkl} \cdot \sin(\Theta) = n\lambda, \tag{2.6}$$

where λ is the wavelength, Θ is the incidence angle and d_{hkl} is the inter-planar spacing of a set of planes with Miller indices hkl.

In a microscopic picture diffraction can be explained as the scattering of an incoming wave at an array of scatterers (atoms of the crystal lattice), where the back-scattered waves only interfere constructively at certain angles, which again results in the observed diffraction spots. A schematic sketch is presented in Figure 2.7 a. Rather than trying to calculate diffraction patterns resulting from scattering events at an array of thousands of atoms in real space, the problem becomes much easier if it is calculated in reciprocal space. The elastic scattering process is sketched in Figure 2.7 b, where an incoming wave with wave vector $\mathbf{k}_{\text{in}}$ and a scattered wave with $\mathbf{k}_{\text{out}}$ are shown. The scattering angle between the incoming and outcoming wave is 2Θ. The requirement for elastic scattering is that during the process no energy is lost and $|\mathbf{k}_{\text{out}}| = |\mathbf{k}_{\text{in}}|$. The change in wave vectors

is called momentum transfer $\mathbf{Q}$, and is defined as $\mathbf{Q} = \mathbf{k}_{out} - \mathbf{k}_{in}$. Considering specular scattering $\Theta_{\text{in}} = \Theta_{out}$ and $2\Theta = \Theta_{\text{in}} + \Theta_{\text{out}}$, one can calculate the momentum transfer, which is an equivalent to Bragg's law in reciprocal space

$$|\mathbf{Q}| = 2|\mathbf{k}_{\text{in}}| \cdot \sin\Theta = \frac{4\pi \cdot \sin\Theta}{\lambda}, \quad \text{where} \quad |\mathbf{k}_{\text{in}}| = \frac{2\pi}{\lambda}. \tag{2.7}$$

A combination of Bragg's law in real space (Eq. 2.6) and reciprocal space (Eq. 2.7) leads to

$$|\mathbf{Q}| = \frac{2\pi n}{d_{hkl}}. \tag{2.8}$$

Taking into account that the reciprocal lattice vector $|\mathbf{G}|$ can be defined as $\frac{2\pi}{d_{hkl}}$, Equation 2.8 shows that the condition for constructive interference is fulfilled if and only if the momentum transfer is equal to a reciprocal lattice vector or an integer multiple

$$|\mathbf{Q}| = n|\mathbf{G}|. \tag{2.9}$$

The relation between the condition of constructive interference and the reciprocal lattice of the crystal is called Laue equation and can be illustrated graphically using the Ewald's sphere synthesis. The sphere is constructed with the crystal at its center and a radius of $|\mathbf{k}_{\text{in}}|$. Considering elastic scattering, the diffracted beam $\mathbf{k}_{\text{out}}$ as well as the momentum transfer, also known as scattering vector $\mathbf{Q}$, will also lie on the sphere for arbitrary scattering angles. As described in [26], the origin of the reciprocal lattice is defined as the spot where the incoming beam intersects the Ewald's sphere. This construction shows at which scattering angles the Laue condition is satisfied for a certain crystal. Figure 2.8 shows the Ewald's sphere construction and the reciprocal lattice. It is shown that $\mathbf{Q} = \mathbf{G}$ is fulfilled if a reciprocal lattice point intersects the Ewald's sphere.

2.2.2 Diffraction at 2D-lattices

As the name implies, using surface-sensitive diffraction techniques such as RHEED (Section 3.3.1) and LEED (Section 3.3.2), it is possible to observe diffraction caused only by

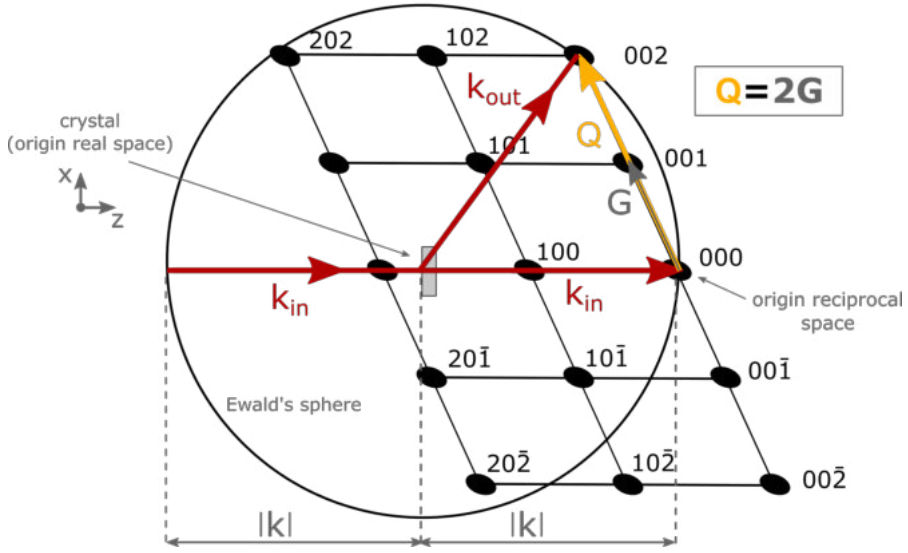

Figure 2.8: Example of an Ewald's sphere synthesis, where the 002 spot of the reciprocal lattice intersects with the sphere. A diffraction spot is observed in the direction perpendicular to the 002 planes of the crystal, because the scattering vector is equal to a reciprocal lattice vector.

the first few layers of a crystal. In an idealized situation, the diffraction at a 2D-lattice of surface atoms has to be considered. To describe such a 2D-lattice in reciprocal space, one can simply define the planes in the real space z-direction as being infinitely far apart from each other, which results in a reciprocal lattice vector $z^* = 0$. In this direction the constructive interference condition is always fulfilled, and the lattice points in reciprocal space become infinitely long rods, instead of lattice points, as shown in Figure 2.9. In principle the condition to observe diffraction spots stays the same, namely that the momentum transfer is equivalent with a reciprocal lattice vector $\mathbf{Q} = \mathbf{G}$.

2.2.3 Diffraction of electrons

Section 2.2.1 already anticipated the fact that diffraction at a crystal lattice is not only observed when it is exposed to coherent light. It is also possible to observe diffraction of electrons, *e.g.*, an electron beam, when directed onto a crystal. Quantum mechanical considerations allow to describe a free moving particle as a wave using the de Broglie

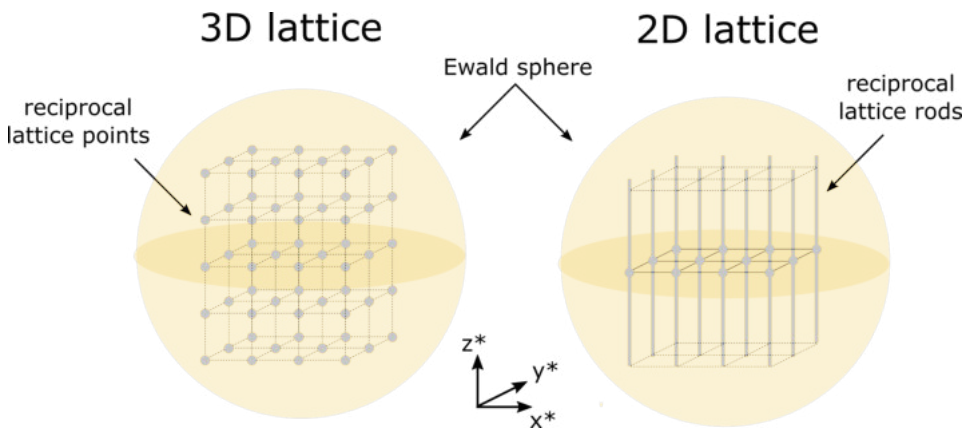

Figure 2.9: Sketch of the reciprocal space of a 3D lattice (left) and a 2D lattice (right).

relationship. Considering the definition of the de Broglie wavelength of a particle

$$\lambda = \frac{h}{p} = \frac{h}{\sqrt{2mE}}, \tag{2.10}$$

one can derive an approximate form for λ as

$$\lambda\,[\mathring{A}] \approx \sqrt{\frac{150}{E_{\text{kin}}\,[eV]}}. \tag{2.11}$$

For electrons with energies in the range of $50 - 500\,\text{eV}$, Equation 2.11 leads to de Broglie wavelengths between 1.7 and 0.5 Å. These values are in the same order of magnitude as the inter-planar distances in a crystal. Hence, electrons in this energy range are well suited for crystal diffraction experiments.
In the discussed energy range the impinging electrons interact mainly with the atomic shell electrons of the crystal atoms, due to elastic and inelastic scattering. Taking into account the inelastic mean free path of electrons, as presented in Figure 2.10, the maximum interaction is reached for electrons with energies in the range of $20 - 500\,\text{eV}$. Electrons with this energies have a typical inelastic mean free path of $< 10\,\text{Å}$.

The short inelastic mean free path in combination with an appropriate de Broglie wavelength for diffraction at crystal lattices allows to use low-energy electrons for surface-sensitive diffraction experiments (see Section 3.3.2). It should be mentioned that it is

also possible to use higher energetic electrons for surface-sensitive crystal diffraction experiments. However, in this case, a special experimental setup is necessary to achieve high surface sensitivity. The idea is to direct the high energy electron beam ($10 - 100\,\mathrm{keV}$) under very grazing angles onto the crystal surface. Due to the grazing incidence, the electrons do not penetrate deep into the surface. Furthermore, the perpendicular component of the wave vector of the incoming electrons is again roughly in the same order of magnitude as the interplanar distances of the reciprocal lattice. Thus, it is possible to investigate surface diffraction with high energy electrons, if they impinge under very grazing angles (see Section 3.3.1).

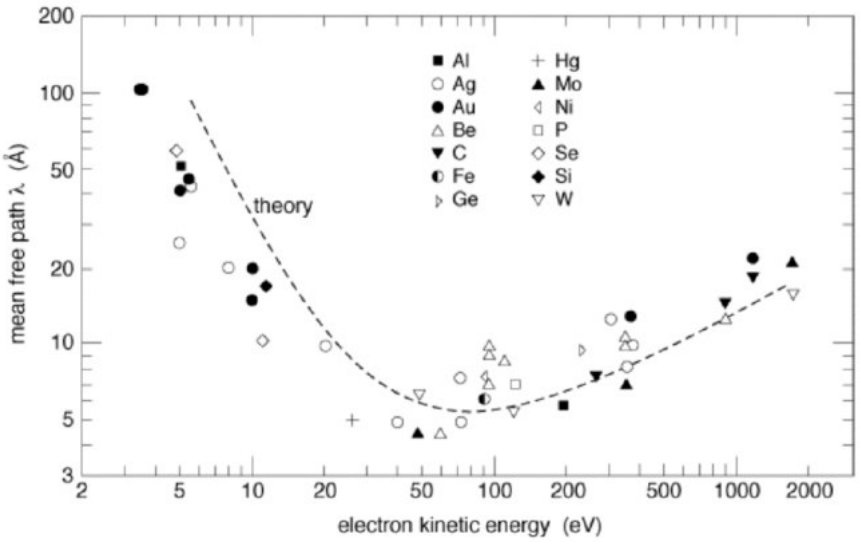

Figure 2.10: Universal curve for the inelastic mean free path of electrons. Reprinted from [27].

2.2.4 Diffraction of photons

The basic principle for diffraction of photons is exactly the same as for the previously discussed diffraction techniques. Instead of electrons the sample is irradiated with X-rays with an energy of approximately $3-8\,\mathrm{keV}$, since the wavelength of these X-rays is of the same order of magnitude as the interatomic distances of a crystal. If the X-rays are directed onto the crystal, the decreasing intensity caused by absorption can be described

using Beer-Lambert's law

$$I = I_0 e^{-\mu d}, \tag{2.12}$$

with I and I_0 being the intensity at a distance d inside the material and the initial intensity respectively, and μ the absorption coefficient. In terms of crystallographic dimensions, the X-rays penetrate deep into the bulk ($\sim \mu$m). Thus, a 3D-like diffraction is observed in contrast to the previously-discussed surface-sensitive electron diffraction methods. The investigation of bulk crystallographic properties with X-rays is referred to as XRD and is discussed in more detail in Section 3.3.3.

2.3 Photon-atom interaction

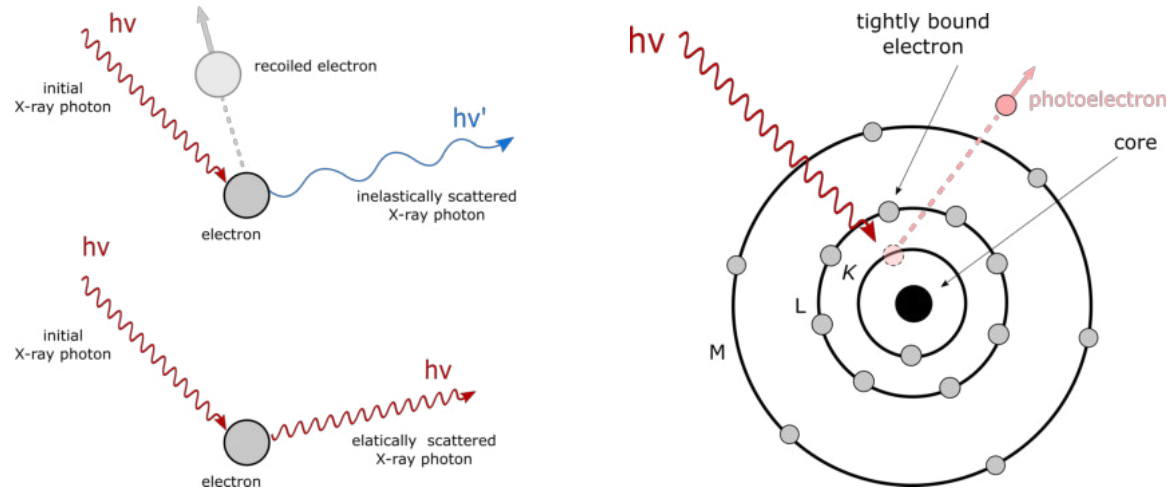

(a) Compton/Thomson scattering **(b)** Photoelectric effect

Figure 2.11: (a) Sketch of the Compton (top) and Thomson scattering (bottom). Depending on the energy of the initial photon, energy is or is not transferred to the electron during the scattering process. (b) Sketch of the photoelectric effect, where a X-ray photon is absorbed, creating a photoelectron from an inner shell. The resulting inner shell hole is depicted in pale red.

X-ray photon energies typically used for techniques such XRD or XPS are in the range of $1 - 10$ keV. In this energy range the interaction of the X-ray photons with the crystal is governed by the following three effects:

- Compton scattering
- Thomson scattering
- Photoelectric effect

Compton scattering can not be described classically, as it is a quantum mechanical phenomena. The Compton effect describes the approximated situation, where an incoming photon is scattered at a free electron at rest, as shown in Figure 2.11 a. The energy of the incoming photon is high enough to recoil the electron, resulting in an energy and momentum transfer from the photon to the electron. This leads to a reduction of the energy of the scattered photon, and thus a larger wavelength is observed. In other words, Compton scattering is an inelastic process, which is dominant in the energy range of $\sim$0.5 MeV. Since the typical photon energies involved in XRD and XPS lie in the $1 - 10$ keV range, Compton scattering has very small contributions, and will therefore be neglected in the following.

Thomson scattering is the low-energy limit of Compton scattering. If the incoming photon has low enough energy, the recoil of the electron is negligible. Due to this effect, there is no wavelength shift observed, and the energy of the incoming photon is equal to the one of the outgoing photon. Therefore, Thomson scattering is an elastic phenomenon. A classical picture to illustrate Thomson scattering is to consider the photon as an electromagnetic wave with large wavelength. The changing electric field at the position of the electron causes periodically-changing, accelerating forces, resulting in an oscillating movement of the electron. The oscillating electron can be considered as a Hertz dipole, which emits electromagnetic radiation with the same energy as the initial photon. The emitted electromagnetic radiation from each excited surface atom interfere constructively and destructively, resulting in a experimentally observable diffraction pattern.

Another atom-matter interaction relevant for the X-ray-based analysis techniques used in this thesis, is the photoelectric effect, also known as photoinoization. As depicted in Figure 2.11 b, an incoming X-ray photon with energy $h\nu$ excites an electron from an inner shell. If the absorbed photon energy is high enough, the atom is ionized and the

excited electron has enough energy to overcome its binding energy and leave the atom. In other words, in this process free electrons are created by absorbing the energy of a photon. These free electrons are called photoelectrons and are important for XPS, which is further discussed in Section 3.4. After the emission of a photoelectron the atom is left with a hole in a inner shell, which in general is an energetically unfavourable configuration. In other words, the atom is left behind in a meta-stable excited state, which tends to relax back into the ground state. An electron from a higher shell can reduce its energy and fill the hole in the inner shell, as shown in Figure 2.12a. Filling up the hole is equivalent with an energy decrease equal to the difference in binding energies of the inner- and outer-shell electrons. In order to conserve energy, two competing mechanisms can occur, namely radiative and non-radiative relaxation. In the former case, a single photon is emitted (X-ray fluorescence, see Figure 2.12a), while in the latter the energy is resonantly transferred to a third electron that, in turn, is expelled form the material (Auger effect, see Figure 2.12b).

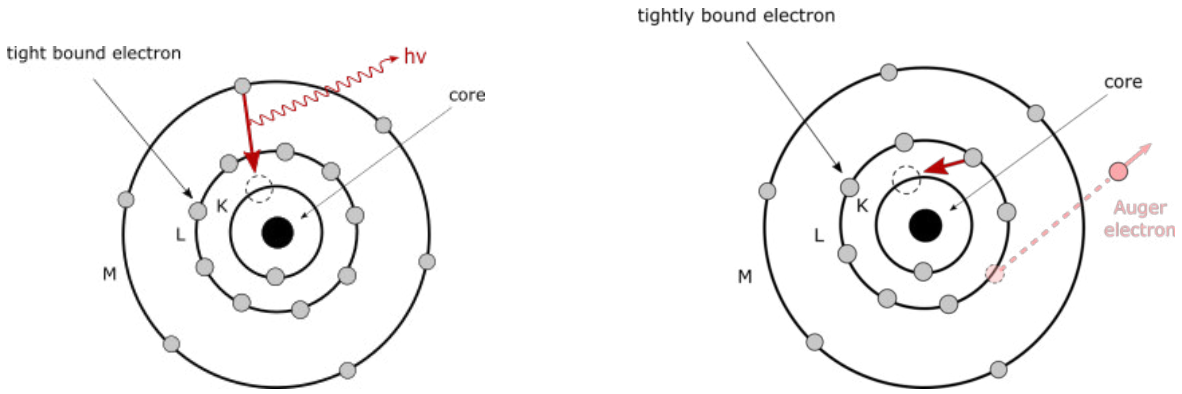

(a) X-ray fluorescence **(b)** Auger effect

Figure 2.12: Basic sketch of the two competing mechanisms for a system to relax back to the ground state after a core hole has been created.

2.4 Quantum mechanical tunneling effect

This section provides a short introduction into the quantum mechanical tunneling effect; the basis for scanning tunneling microscopy (STM), which is discussed later in Section 3.5. The quantum mechanical tunneling effect states that electrons can overcome a thin finite potential barrier, even if their energy is lower than the potential barrier, as

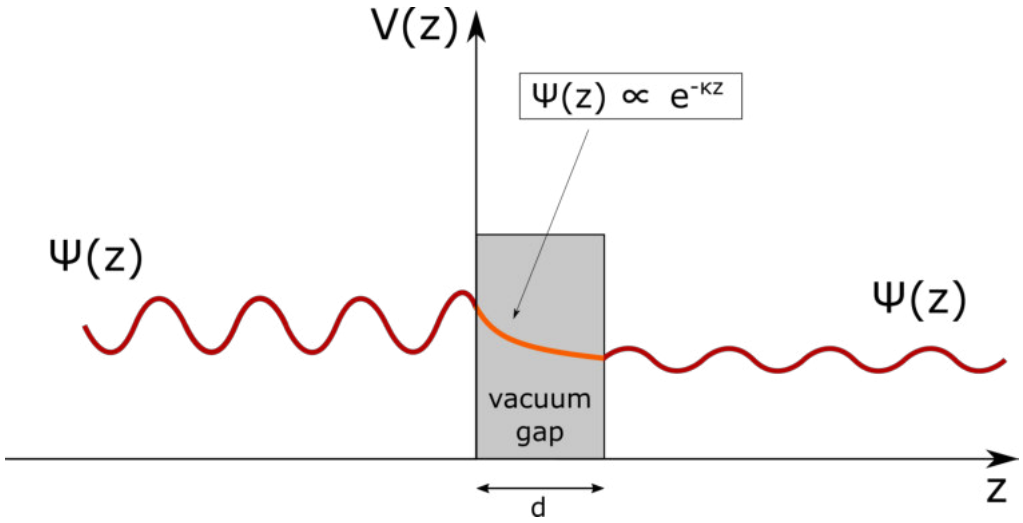

Figure 2.13: Simple sketch of the quantum mechanical tunneling effect. In the barrier the wave function is decreasing exponentially with the distance.

shown in Figure 2.13. In a classical picture the potential barrier would be high enough to prevent a transmission of the wave function through the barrier. In a quantum mechanical picture, the electron wavefunction can pass through the potential barrier, while its amplitude decreases exponentially with the potential barrier thickness d. This exponential dependence on the barrier thickness is the key to enable atomic resolution STM measurements, as is discussed later in Section 3.5. This dependence can be easily derived in a simplified case, shown in Figure 2.13, assuming the one dimensional, time-independent Schrödinger equation

$$\left(\frac{-\hbar^2}{2m}\nabla^2 + V(z)\right)\Psi(z) = E\Psi(z), \tag{2.13}$$

where Ψ is the wave function, m is the mass of the electron, $V(z)$ is the potential barrier and E is the energy of the electron. In our case this is the tunnel-barrier due to the vacuum gap between tip and sample. To simplify the calculations we assume

$$V(z) = const = V. \tag{2.14}$$

In the region of the potential barrier the solution is an exponentially decreasing wave function

$$\Psi(z) \propto e^{-\kappa z}, \quad \text{with} \quad \kappa = \sqrt{\frac{2m(V-E)}{\hbar^2}} \quad \text{and} \quad V > E. \tag{2.15}$$

The probability density $|\Psi(z)|^2$, hence the transmission T, is depending exponentially on the thickness of the barrier d and the attenuation coefficient κ

$$T \propto |\Psi(d)|^2 \propto e^{-2\kappa d}. \tag{2.16}$$

Further information and a detailed treatment of the tunneling effect in STM is provided in [28, 29].

3 Experimental setup and techniques

3.1 UHV-System

In order to achieve high-quality measurements of atomically-clean surfaces, the experiments have to be performed in ultra-high vacuum (UHV). Surfaces, *i.e.*, the topmost atomic layers of a solid, are quite reactive, and in the ambient environment they are contaminated within a fraction of a second. At a base pressure of 10^{-6} mbar each surface atom is hit every second by one gas atom. Thus, base pressures well below 10^{-9} mbar are needed to guarantee a clean sample surface. The surface-sensitive measurement techniques RHEED, LEED, XPS, STM are introduced later and were performed in UHV conditions, while AFM and XRD were performed in ambient conditions.

3.1.1 "Specs Lab" vacuum chamber

Since the key importance of a good vacuum for surface-related experiments has been already emphasized, the vacuum chambers used for this thesis will be described briefly. The main work was done in the 'Specs Lab' of the Surface Science Group from the Institute of Applied Physics of the University of Technology in Vienna. A sketch of this unique system is provided in Figure 3.1. The system consists of four UHV chambers, which are interconnected via gate valves:

- Preparation chamber
- Analysis chamber
- Transfer chamber
- PLD chamber

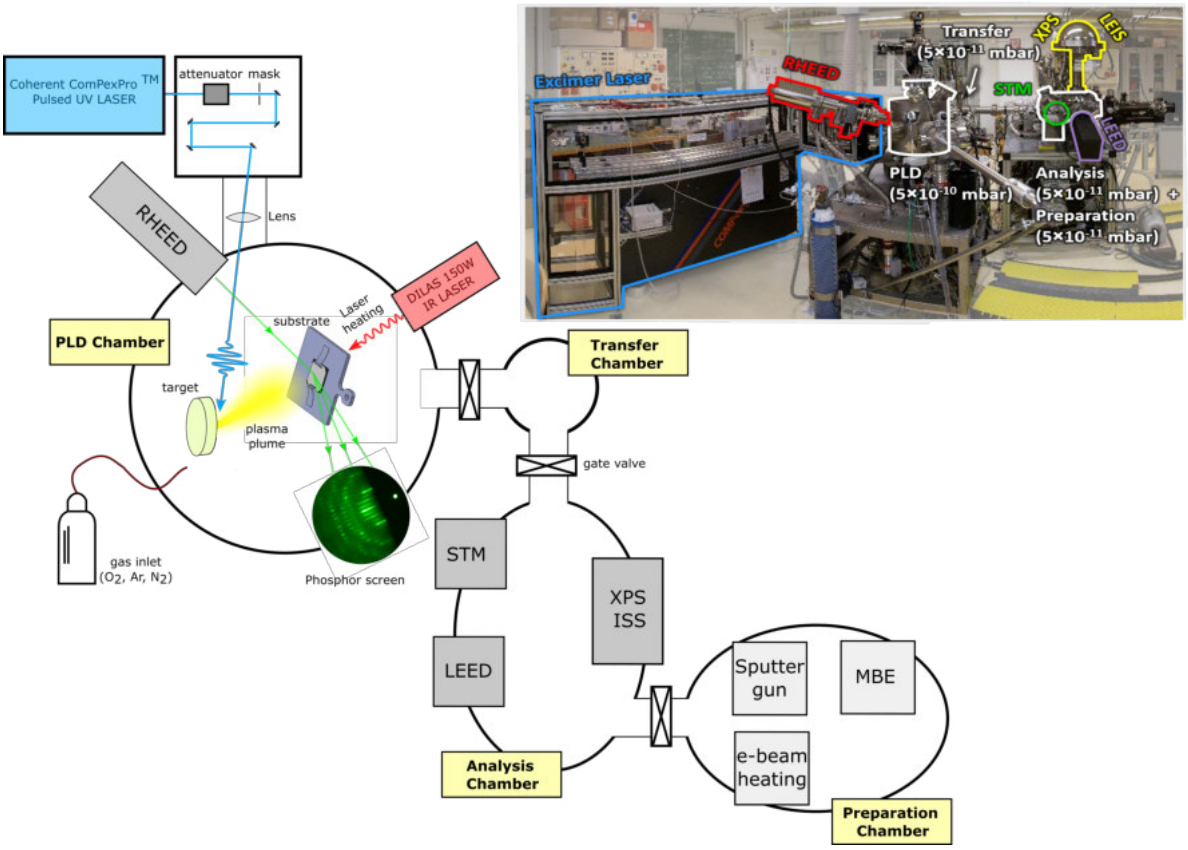

Figure 3.1: Sketch of the vacuum system that was used to prepare, grow, and analyse the samples with RHEED, LEED, and XPS.

Using a system of several manipulators and wobble sticks it is possible to move a sample from the preparation chamber, via the analysis and transfer chamber, to the PLD chamber. During this transfer the sample stays in vacuum at all times and does not get in contact with ambient air. In typical operation conditions the base pressure of all the chambers is usually in the regime of $10^{-10} - 10^{-11}$ mbar.

The vacuum is provided by a combination of scroll pumps, turbomolecular pumps, ion pumps, and titanium sublimation pumps. Usually the scroll pump provides a rough vacuum of roughly 10^{-2} mbar, which is necessary for the turbo molecular pump. The turbo pump is already able to create ultra high vacuum up to 10^{-10} mbar. The turbo molecular pump consists of a rapidly spinning bladed rotor, which transfers momentum to the residual gas atoms. The blades hitting the atoms cause a movement in a certain direction, which compresses the residual gas, which can then be pumped away more eas-

ily. Using an additional ion pump allows to improve the vacuum by at least one order of magnitude. The ion pump ionizes residual gas atoms. The ions are accelerated to the electrode, which usually consists of Ti. The impact of the residual gas ions sputters Ti, which covers surrounding surfaces. The coated Ti surfaces are very reactive and will bind reactive gases hitting the chamber walls. To additionally decrease the number of remaining gases in the UHV, a titanium sublimation pump (TSP) can be used. A Mo-Ti alloy filament is heated in periodic cycles in order to sublimate titanium. Each sublimation process coats the surrounding walls of the chamber with a titanium layer, which can react and trap reactive gasses analogously to the ion pump.

As the names already indicate, each of the chambers is dedicated to one special task. The ***preparation chamber*** is used to prepare samples, with Ar-sputtering, e-beam annealing or molecular beam epitaxy deposition with a Knudsen effusion cell, or an e-beam evaporator. Sputtering-annealing cycles allow to first clean-off, and then heal the surface. The Knudsen cell can be used to evaporate and deposit different materials on the sample surface, if needed. The preparation chamber is connected to a loadlock, which is not sketched in Figure 3.1. The loadlock is used to insert samples into the system. It is separated from the preparation chamber with a gate valve and can be pumped using a scroll and turbo pump.
The ***analysis chamber*** is equipped with various surface-sensitive analysis tools, which will be described in the following sections. In this thesis the analysis chamber was used to characterize the In_2O_3 thin films and the YSZ substrates using XPS and LEED.
The ***transfer chamber*** is only used as a sample storage, and to transfer samples from the analysis chamber to the PLD chamber, and vice versa.
The centrepiece of the whole system is the ***PLD chamber***, where the growth is performed. The PLD chamber is equipped with a UV (Coherent ComPexPro) and an IR Laser (DILAS 150 W IR-Laser), as well as a RHEED setup for growth monitoring. As depicted in Figure 3.1, it is possible to control the background pressure using a gas inlet to provide O_2, Ar or N_2. A detailed description of the PLD process is given in the Section 3.2. The In_2O_3 PLD sputter target (diameter: 25.4 mm, thickness: 5 mm) was bought from China Rare Metal Material Co., Ltd. The target has a density of 4.64 g/cm^3

($\sim 65\%$ of the single crystal density) and a purity of $\geq 99.99\%$.
At this point it should be emphasized that the STM measurements were not done in this vacuum system. Since one of the final goals of the thesis is to provide samples which can be used in different chambers, the STM measurements were performed in the so-called LT-STM vacuum chamber. Since XRD and AFM measurements were done in air, one task of the thesis work consisted in finding a recipe to re-prepare the surface of the In_2O_3 film after contact with ambient conditions in a different vacuum chamber.

3.1.2 "LT-STM" vacuum chamber

As already mentioned, for STM measurements the LT-STM (Low-Temperature Scanning Tunneling Microscope; Omicron) at the Institute of Applied Physics at the Vienna University of Technology was used. The system consists of two vacuum chambers separated via a gate valve, one for preparation and one for analysis (see Figure 3.2).
The ***preparation chamber*** has a base pressure of about 5×10^{-11} mbar and is equipped with standard surface science tools to prepare or analyse the sample. The sample manipulator is equipped with a facility for sample heating (resistive heating) up to 600 °C and cooling with liquid nitrogen to approximately 100 K. Moreover, there is a separate annealing stage (electron beam heating), an ion source for sputtering or low-energy ion scattering (LEIS) and a X-ray source for photoelectron spectroscopy (XPS) and Auger electron spectroscopy (AES). In order to detect the electrons and ions a hemispherical analyzer is used. Furthermore, the chamber is equipped with an electron source and low-energy electron diffraction optics (LEED), an electron beam evaporator for thermal deposition, a quartz crystal microbalance (QCM) for deposition rate measurements, and a residual gas analyzer (quadrupole mass spectrometer).
The ***analysis chamber*** has a base pressure of about 5×10^{-12} mbar and mainly consists of the LT-STM, which allows measurements at 5 K or 78 K (see Figure 3.2).

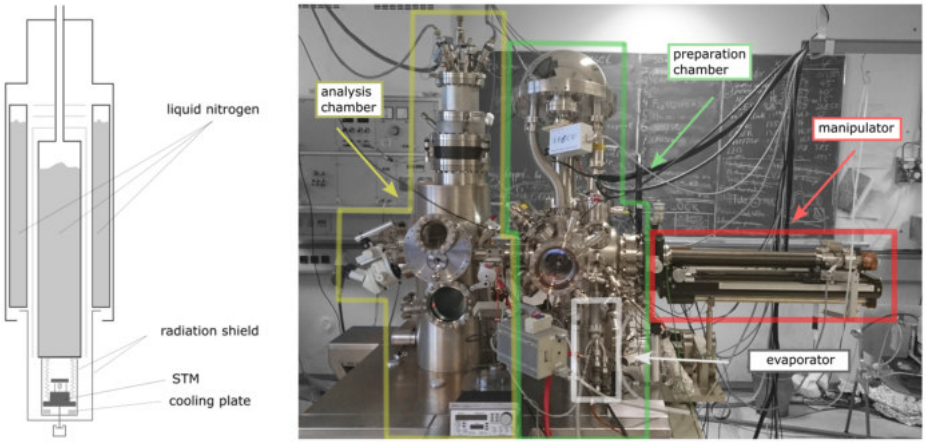

Figure 3.2: Left panel: Schematic of the bath cryostat system, which can also be filled with liquid helium in the inner cryostat instead of liquid nitrogen. Right panel: LT-STM overview - analysis chamber (yellow), preparation chamber (green), Knudsen cell evaporator (white) and sample manipulator (red).

3.2 Pulsed laser deposition (PLD)

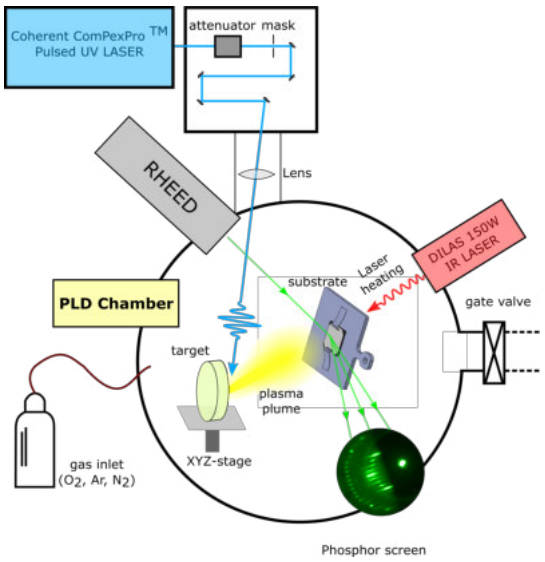

Figure 3.3: Detailed sketch of the PLD chamber.

Nowadays, alongside molecular beam epitaxy (MBE), pulsed laser deposition (PLD) is one of the most common thin film growth techniques. Both MBE and PLD belong to the class of physical vapor deposition methods. Since the discovery of the laser in the

1950s, various experiments were carried out to investigate the use of PLD as an evaporative thin film growth technique. However, in the beginning the success was limited by the less developed laser technology. Moreover, considering the demands of that time, PLD did not provide additional advantages compared to other growth techniques. This fact changed rapidly in the late 1980s with the discovery of high-T_C superconductors $YBa_2CU_3O_{7-\delta}$. These highly-complex oxide materials require high stoichiometric control of the deposited material and high oxygen background pressures. PLD is suitable for both mentioned properties and indeed, highly stoichiometric, superconducting thin films could be produced using PLD. The high interest in this field also helped to further develop the PLD technology and made it one of the most common thin film growth techniques nowadays, because of its good performance and versatility.

A detailed sketch of the PLD vacuum chamber, which was used in this thesis, is shown in Figure 3.3. A high power UV laser pulse is used to ablate atoms from a sputter target or a single crystal of the material to be deposited. The provided energy is high enough to create a plasma of highly-energetic target particles. These species will rapidly expand in the direction perpendicular to the target surface, forming the so-called plasma plume. As shown in Figure 3.3, if the substrate is positioned opposite the target, atoms in the plasma plume will be deposited equally on the substrate surface. During the process the target is scanning via a xyz-stage to avoid ablating always the same spot on the sputter target, and thus guarantee a well-controlled ablation process. A strong absorption of the target material at the used laser wavelength is a key requirement of the PLD process. In this thesis a Coherent ComPexPro Pulsed UV laser was used, which is an excimer KrF-laser with a wavelength of 248 nm. Since photons with this wavelength provide energies of roughly 5 eV, it is possible to overcome the optical bandgap of In_2O_3 (~ 3.75 eV [30]), resulting in strong absorption.

3.2.1 Detailed discussion of the PLD process

As shown in Figure 3.4 i), the laser beam is focused on the target, resulting in a high energy density in a small volume of target material. This situation is equivalent to an ablation using a high laser fluence, which can be defined as

$$\text{Fluence}(\text{J/cm}^2) = \frac{\text{laser pulse energy (J)}}{\text{focal spot area (cm}^2\text{)}}. \tag{3.1}$$

If the fluence is not high enough, the laser beam would simply heat up the target, resulting in a deposition flux due to thermal evaporation. This situation has to be avoided especially in stoichiometric PLD growth, because the different vapour pressures of the multicomponent target material would correspond to an off-stoichiometric flux of target cations. If the fluence is increased, and a certain ablation threshold is reached, the vaporisation will become almost independent of the vapour pressure of the material, because the absorbed energy by far exceeds the energy needed for evaporation. As the onset of the laser pulse reaches the target, the irradiated surface atoms become immediately vaporized. While these vaporized atoms are still accumulated close to the surface they are heated due to the interaction with the remaining laser pulse. The energy is high enough that a plasma of highly energetic target atoms, ions, or molecules is formed at the target surface, as shown in Figure 3.4 ii). Due to the high pressure in the plasma layer and the low background pressure in the

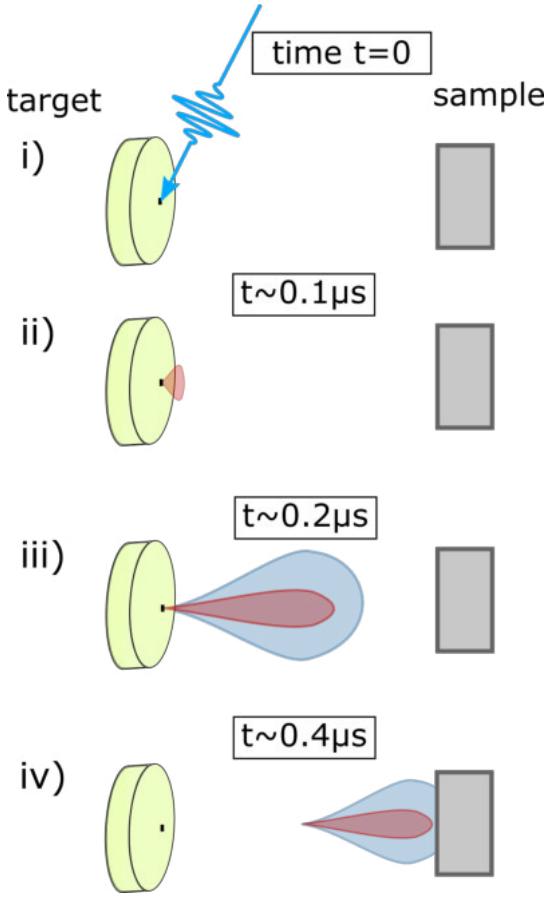

Figure 3.4: Sketch of the ablation process using PLD.

vacuum chamber, the species within the plasma will expand rapidly, forming a plasma plume. The plasma plume expands perpendicularly to the target surface, as shown in Figure 3.4 iii). Depending on the background pressure, the highly kinetic target particles are scattered differently at the gas molecules of the background gas. A high background pressure results in many scattering events and leads to a broadened appearance of the plasma plume (sketched in blue), while low background pressure is equivalent to less scattering events and a more focused plasma plume (sketched in red). Since these scattering events also include inelastic scattering, the kinetic energy of the scattered particles at lower pressures is on average much higher. In contrast, if the background pressure is high and the ablated species experiences a sufficient number of scattering events, the ablated atoms will become thermalized and reach the sample surface with minimum energy.

3.2.2 PLD growth characteristics

As already discussed at the beginning of this section, PLD allows a highly stoichiometric growth of complex oxide materials. Further advantages of PLD growth compared to other growth techniques will be discussed in the following.

The most important difference with respect to growth techniques like MBE is that PLD growth can be considered as a discontinuous deposition technique. Increasing the instantaneous deposition rate leads to more off-equilibrium conditions than for MBE. This property can affect the adopted growth mode, although the time averaged growth rate is comparable to MBE. In addition, PLD growth can be viewed as short deposition events followed by a long annealing time, in contrast to MBE growth, where a constant flux of deposited material is observed. Every laser pulse is depositing a certain amount of material onto the surface. The deposition takes place rapidly ($\sim \mu$s) compared to the time in between two laser pulses (1 s, if a typical frequency of 1 Hz is used). The actual deposition rate can be controlled by various factors, *e.g.* fluence, target-sample distance, background pressure or repetition frequency of the UV laser. It should be mentioned that in this thesis typical deposition rates of ~ 0.01 nm/sec were used.

Another key advantage of PLD is the possibility to grow at high background pressures,

which is especially relevant for oxide materials. In fact, the oxygen background pressure is one of the most important growth parameters in oxide thin film growth. On the one hand, the ablated target atoms, ions and molecules are scattered at the oxygen molecules from the background gas. Due to scattering with the oxygen, the metallic target atoms or ions can become oxidized and form some oxidized species, which can be crucial for the film growth. On the other hand, the scattering with the background gas atoms reduces the kinetic energy of the ablated species, as already described in the previous section. The ablated species can exhibit kinetic energies up to several hundreds eV. By increasing the background pressure it is possible to tune the kinetic energy of the particles impinging the substrate surface, which can have a dramatic effect on the growth mode and the final morphology of the grown film.

3.3 Diffraction techniques

3.3.1 Reflection high-energy electron diffraction (RHEED)

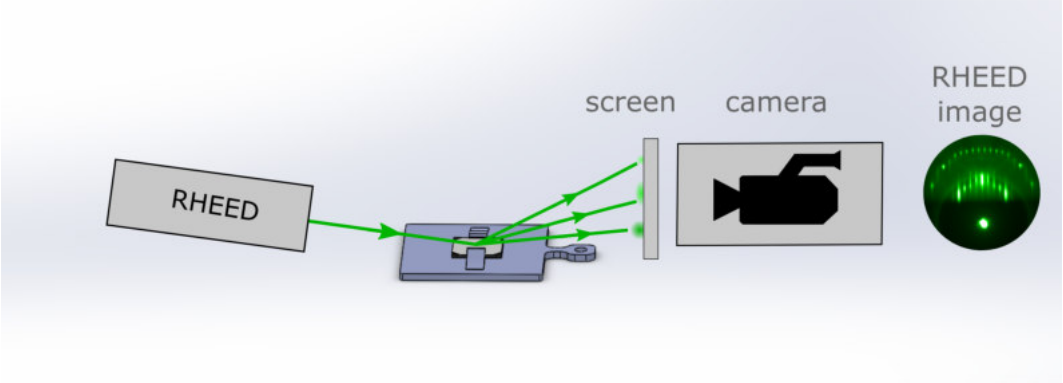

Figure 3.5: Sketch of a typical RHEED setup.

As the name suggests, reflection high-energy electron diffraction (RHEED) exploits the effect of electron diffraction to investigate the structure of crystalline surfaces. The physical basics of electron diffraction have already been discussed in Section 2.2.3, while in this section the most important measurement methods and technical details will be

discussed. More detailed information about RHEED is provided in [21, 24].
In a typical RHEED setup a high-energy electron beam of approximately 10 - 100 keV impinges on the surface under very grazing angles ($< 5°$). In order to detect the RHEED pattern, a phosphor screen combined with a camera is mounted opposite to the RHEED gun, as depicted in Figure 3.5. The diffracted electron beam illuminates the phosphor screen, which can be live-captured by the camera.
The Ewald's sphere construction of such a RHEED setup is shown in the left panel of Figure 3.6. As discussed in Section 2.2.2, 2D-like diffraction results in diffraction spots where the lattice rods intersect the Ewald's sphere. The sketched lattice rods should be considered as planes of lattice rods perpendicular to the x-axis, which cut out circles from the Ewald's sphere. As a result, the diffraction spots appear along these so-called Laue circles, which are a characteristic indication for 2D-diffraction. The right panel of Figure 3.6 presents a typical RHEED diffraction pattern, featuring the direct beam and the 0^{th} and 1^{st} order Laue circles.

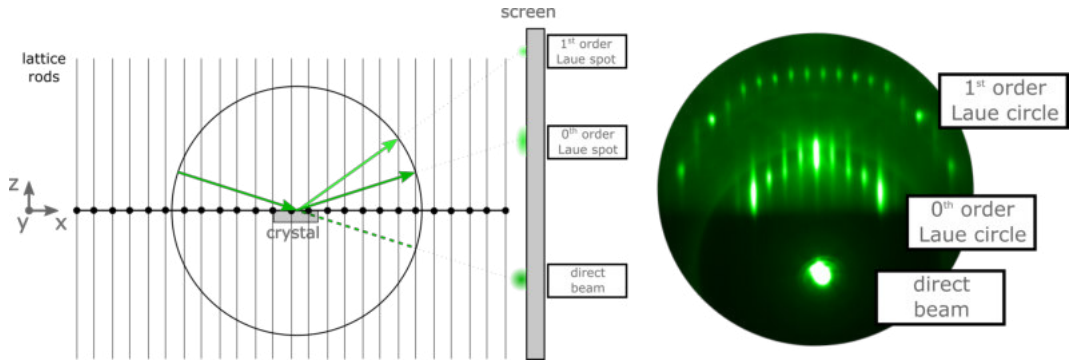

Figure 3.6: Simplified image of an Ewald's sphere construction for a typical RHEED setup (left). The sketch is drawn in the $x - z$ plane. Taking into account the y-component of the reciprocal lattice explains the transition from Laue spots (left) to Laue circles (right).

RHEED is probably the most fundamental *in-situ* surface-sensitive analysis tool for growth experiments. In almost all thin film growth methods the direction of the deposition is perpendicular to the sample surface. Due to its grazing incidence alignment, the RHEED does not occupy the space opposite to the sample, as can be seen in Figure 3.5. Thus, it is possible to investigate the crystalline quality of the grown film surface *in situ*

and even during the growth. The analysis of the RHEED pattern of an unknown film can give a first rough indication on how the surface will look like.
As indicated in Figure 3.7, a perfectly flat surface would result in sharp diffraction spots arranged in the previously addressed Laue circles. A more realistic sketch, taking into account a stepped surface, results in broadening of the Laue spots. Especially for high electron energies, the radius of the Ewald's sphere becomes large ($r \propto \frac{1}{\lambda}$). As a result the lattice rods intercept the sphere in a very grazing fashion, which results in streaks in the observed RHEED pattern. At the bottom of Figure 3.7 the effect of a surface with a high coverage of 3D islands is shown. The resulting RHEED pattern is characterized by sharp spots arranged in a regular 2D lattice, which result from 3D-bulk-like diffraction. Each island acts as a small bulk crystal, which explains the observed sharp diffraction spots.

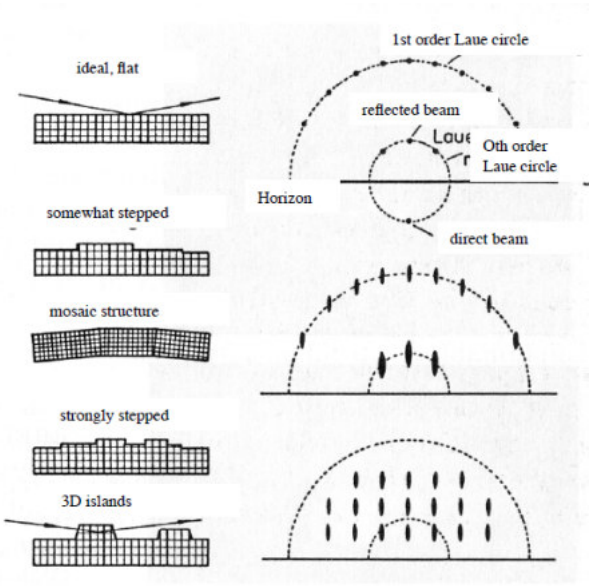

Figure 3.7: Effect of not ideal surfaces on the appearance of the RHEED pattern. Reprinted from [31]

The second and probably even more important, area of application of a RHEED system is real-time growth monitoring. For this purpose, the intensity of a single diffraction spot is measured during the growth. During growth the surface morphology changes, which leads to an increase or decrease of the diffraction spot intensity, because

the measured intensity is strongly dependent on the flatness of the surface. How the diffraction spot intensity changes is characteristic for the adopted growth mode. The different modes for crystal growth have already been discussed in Section 2.1 and their characteristic RHEED intensity behaviour are discussed in the following:

- *Layer-by-layer growth:* During the first stages of growth, the surface will become rougher, as the first deposited atoms adsorb and form small islands on the surface. This leads to a decrease in the measured intensity. If enough material has been deposited to almost complete a first, flat layer of the growing film, the measured RHEED intensity starts to increase again. Ideally speaking, the first, complete layer of the adsorbed film should exhibit the same flatness and surface morphology as the substrate. Thus, the measured intensity should be comparable to the initial intensity before growth, when the first layer is completed. Due to this behaviour, a periodic increase and decrease of the measured diffraction spot intensity can be observed during growth, as presented in Figure 3.8 a. Counting the maxima of intensity oscillations is equivalent to counting the numbers of complete monolayers, which were deposited. Hence, if a layer-by-layer growth mode is adopted, RHEED can be used as a tool to evaluate the film thickness in real time with sub-monolayer precision.

- *Multilayer growth:* The first stages of growth are similar to the layer-by-layer growth, where an increasing disorder on the surface leads to a decrease of the measured diffraction spot intensity. After these first stages of multilayer growth, the surface does not recover the initial surface morphology, since further growth leads to the nucleation of 3D-like islands. Thus, the film surface becomes rougher and leads to a continuous decrease of the diffraction spot intensity, as indicated in Figure 3.8 b.

- *Layer-plus-island growth:* As already discussed in Section 2.1, the so called Stranski-Krastanov growth mode is a combination of layer-by-layer and multilayer growth mode. Thus, the behaviour of the observed diffraction spot intensity is also a combination of both growth modes, as presented in Figure 3.8 c. At the begin-

ning, a layer-by-layer-like oscillation is observed until the growth mode changes to multilayer growth, which results in a steady decrease.

- *Step-flow growth:* Since in an ideal case, a step-flow growth mode preserves the surface morphology (see Section 2.1), the diffraction spot intensity should be constant, apart from the time when a plume of ablated atoms hits the surface. The almost-instantaneous deposition causes disorder on the surface, leading to a rapid intensity decrease. As the adatoms diffuse to the step edges, recovering the initial flatness of the film, the diffraction spot intensity slowly increases again, as depicted in Figure 3.8 d.

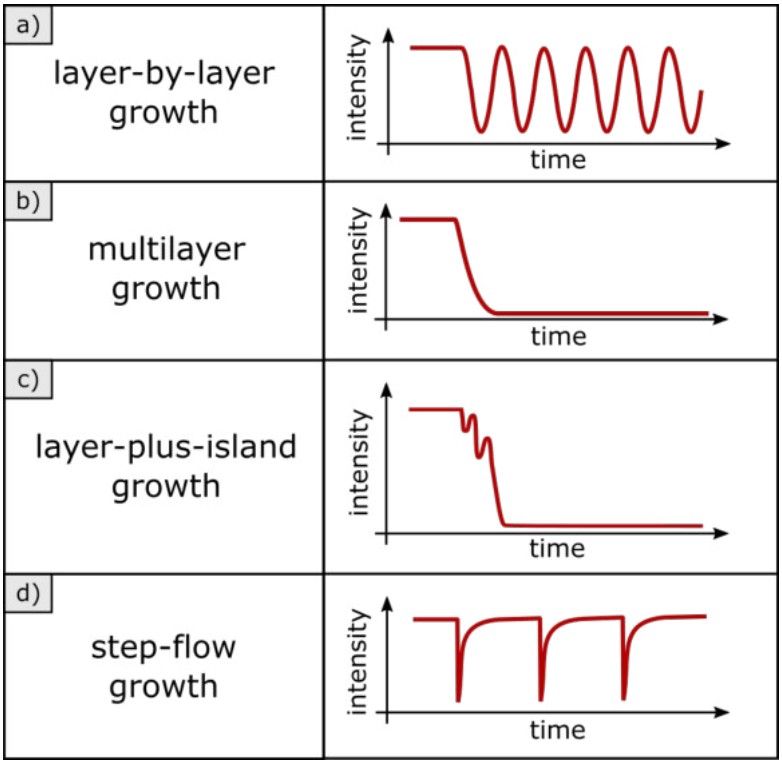

Figure 3.8: RHEED growth monitoring: Idealized dependence of the diffraction spot intensity on the adopted growth mode.

3.3.2 Low-energy electron diffraction (LEED)

Considering the basic principle, this technique is very similar to RHEED, where diffraction is utilized to gain information about the structure of the investigated surface. In

contrast to RHEED, LEED uses low energy electrons (in the range of $50 - 500\,\mathrm{eV}$) to investigate crystal surfaces. As discussed in Section 2.2.3, the small inelastic mean free path of low-energy electrons ($\sim 1 - 10\,\mathrm{nm}$) allows to investigate the crystal structure of the first few layers, because only electrons scattered near the surface can leave the crystal without energy loss.

A typical LEED setup is shown in Figure 3.9. The electron gun consists of a cathode and several focusing units, including a Wehnelt cylinder and focusing lenses. As depicted in Figure 3.9, the electron beam is impinging perpendicular to the sample surface and the backscattered electrons are detected by a phosphor screen. In this setup the electron gun hides the bright, specular (0,0) spot. The LEED setup which was used in this thesis, was additionally equipped with a micro channel plate in front of the screen, to further amplify the incoming electrons. Analogously to the RHEED setup, the illuminated phosphor screen can be captured by a camera.

Figure 3.9 shows the Ewald's sphere construction of this specific LEED setup. Diffraction spots occur where the reciprocal lattice rods intersects the Ewald sphere. Again the sketch is presented in the $x - z$ plane (the diffraction caused by the atoms along the y-direction of the crystal surface is not shown). In this setup, the image of the diffraction pattern on the phosphor screen is simply a two dimensional projection of the reciprocal space, which simplifies the identification of diffraction spots. This feature is the reason why LEED is a widespread technique to characterize the crystalline quality of surfaces or surface reconstructions. For further information about LEED, the reader is invited to read [21, 32].

At the end of this section, it should be emphasized once again that only the elastically scattered electrons contain information about the surface structure. The inelastically scattered electrons have to be filtered, because their almost continuous energy distribution below the initial energy would illuminate the screen uniformly and would hide the diffraction spots caused by the elastically scattered electrons. Therefore, a high-pass filter is needed to prevent all the inelastically scattered electrons with a kinetic energy lower than the initial energy to reach the phosphor screen. Experimentally, this can be realized using a retarding field analyser (RFA), where an arrangement of several grids, 2 grounded (same potential as sample) and 2 held at a negative potential, is used to re-

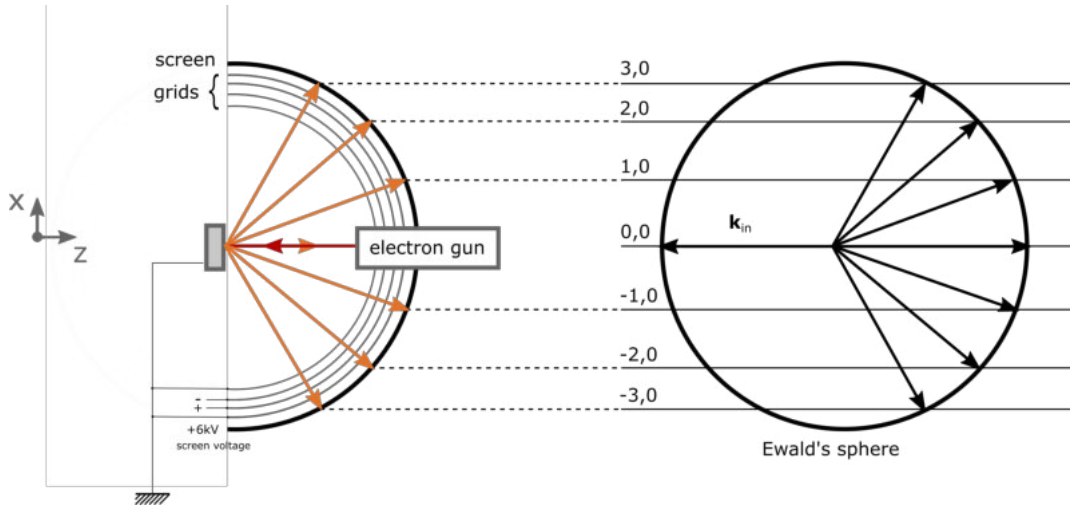

Figure 3.9: Typical LEED setup (left) and its Ewald sphere synthesis in reciprocal space (right).

tard the scattered electrons. The retarding potential is usually set right below the initial energy, which only enables elastically scattered electrons to pass. The screen is held at positive potential, because after the grids the elastically scattered electrons would have too little energy to illuminate the screen.

3.3.3 X-ray diffraction (XRD)

In contrast to the previously-discussed surface-sensitive electron diffraction techniques LEED and RHEED, X-ray diffraction is a tool to investigate the structure of bulk crystals [22]. The basic principle of XRD is exactly the same as for any other diffraction technique. The main difference to the previously discussed methods is that photons instead of electrons are used to irradiate the crystal. As discussed in Section 2.3, X-rays with an energy of approximately $3 - 8\,\mathrm{keV}$ are used in crystal diffraction measurements. In XRD the elastically scattered photons (Thomson scattering) are used to investigate structural crystal properties. The deep penetration depth of X-rays in this energy regime ($\sim \mu\mathrm{m}$) is responsible for the bulk sensitiveness of this measurement method. In XRD, the interpretation of bulk diffraction patterns or investigation of single diffraction spots allow to draw conclusions about diverse crystallographic bulk properties of polycrystalline as well as single crystalline samples. In the next section the measurement methods,

which were used in this thesis, are described briefly.

In this thesis all the XRD measurements were carried out with an Empyrean machine from PANalytical at the TU Wien X-ray Center. A monochromated Cu K-α radiation was used as a X-ray source, which provides photons with an energy of 8.04 keV. The penetration depth of these photons is usually in the range of $0.1 - 10\,\mu$m.

Coupled symmetric scan: Θ-2Θ scan

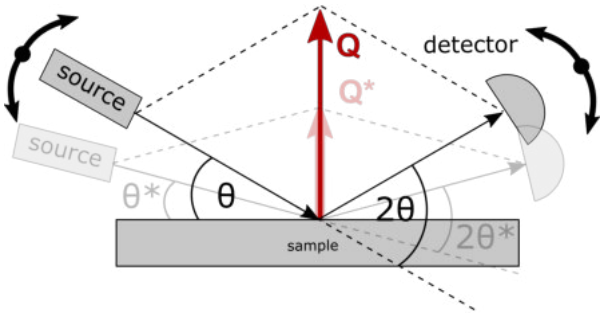

Figure 3.10: Sketch of the Bragg Brentano measurement geometry. The curved black arrows and the transparent sketch indicates the movement of source and detector.

The coupled symmetric scan, also known as Θ-2Θ scan, is a basic measurement method for polycrystalline and single crystalline samples. The simplest setup of a coupled symmetric scan is the Bragg Brentano geometry, where the Q-vector is kept perpendicular to the sample surface (see Figure 3.10).

The angle between the incoming and the outgoing wave is commonly defined as 2Θ and the angle between the incoming wave and the sample surface is usually called ω. If the angle between incoming and outgoing wave is 2Θ, the source can be positioned in such a way that $\omega = \Theta$. Considering a flat sample, which is not tilted, this condition will be satisfied if the source and the detector are at the same height, as depicted in the sketch. During the measurement the source and the detector are moved simultaneously up or down along a circle to keep the distance to the sample and thus the focus constant, as indicated via the black arrows and the transparent sketch in Figure 3.10. Scanning by moving the source and the detector simultaneously, guarantees that the condition $\omega = \Theta$ is always fulfilled, while the value of Θ is permanently changing during the scan. Scanning the source and the detector simultaneously up or down along a circle changes

the magnitude of the momentum transfer (Q-vector). It should be emphasized that the direction of the Q-vector does not change, because $\omega = \Theta$ all the time. This setup allows to probe the interplanar distances of the crystal planes parallel to the sample surface in single-crystalline samples. Considering In_2O_3(111) films, the interplanar distance between the (111) planes can be measured. At some specific angle of $2\Theta_B$ the Q-vector will be equivalent to the (111) reciprocal lattice vector of the crystal, resulting in a peak of the measured intensity, which corresponds to the Bragg reflection from the (111) crystal planes.

Grazing incidence detector (GID) scan

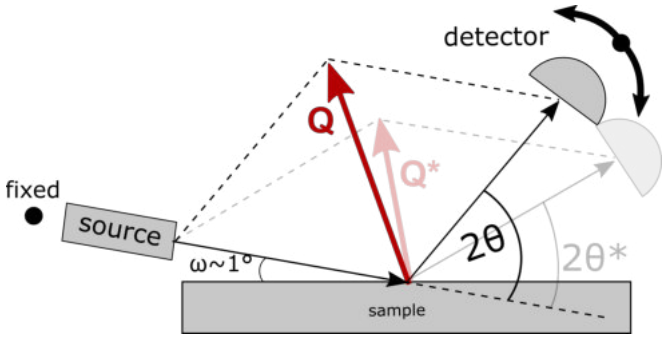

Figure 3.11: Sketch of the GID scan setup. Again the transparent sketch represents the motion of source and detector. The red arrow indicates the momentum transfer.

The measurement setup for this specific technique is shown in Figure 3.11. As the name implies, the incoming beam irradiates the surface under very grazing angles. For this measurement the source is fixed with $\omega \sim 1°$, while only the detector is moved up or down along a circle to scan different 2Θ values. As depicted this leads to a change in the Q-vector. In the GID measurement not only the magnitude, but also the direction of the momentum transfer changes. Thus, the GID scan allows probing different lattice planes, which are not parallel to the sample surface.

Rocking curve measurements

Rocking curve measurements are usually performed to investigate the crystalline quality of single crystalline thin films or single crystals. The measurement schematic is shown

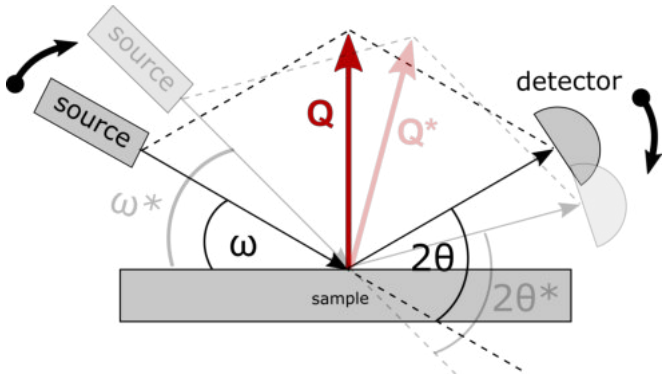

Figure 3.12: Sketch of the rocking curve measurement setup. In this case source and detector are moved to keep 2Θ constant, while varying ω.

in Figure 3.12. As depicted, this measurement requires to keep the value of 2Θ constant throughout the measurement. In order to keep the value 2Θ constant during the measurement ($2\Theta = 2\Theta^*$), the source is moved up if the detector is moved down, or vice versa. If ω is varied, while 2Θ is kept constant, the measurement setup allows to change the direction of the momentum transfer, while keeping its magnitude constant (see Figure 3.12).

Prior to a rocking curve measurement, the initial values for ω and 2Θ are set to measure a certain Bragg reflection. One can then investigate the sharpness of the specific Bragg reflection in reciprocal space by slightly changing the value of ω. Measuring a very sharp peak is equivalent to a very sharp diffraction spot in reciprocal space, indicating a high crystalline quality.

Reciprocal space mapping

A reciprocal space map is obtained by a combination of a symmetric or asymmetric coupled scan and a rocking curve scan. Reciprocal space mapping is used to create a 2D illlustration of the investigated diffraction spot in reciprocal space. This 2D map consists of a series of rocking curve scans at specific 2Θ angles. After each rocking curve measurement the angle of 2Θ is changed by a small amount. Repeating this procedure several times makes it possible to generate a 2D-map of the reciprocal space. Investigating a small area around a diffraction spot allows to draw conclusions about the shape of the diffraction spot. Thus, reciprocal space mapping is an advanced technique

to investigate the crystalline quality of, *e.g.*, heteroepitaxial thin films, as well as the strain within grown films. Reciprocal space maps are usually presented using the in-plane and out-of-plane components of the Q-vector $q_{\parallel}$ and $q_{\perp}$ as coordinates. The following transformation relates the instrumental coordinates ω and 2Θ with the components of the Q-vector $q_{\perp}$ and $q_{\parallel}$ with $K = 2\pi/\lambda$

$$q_{\perp} = K[\cos(\Theta - \omega) - \cos(\Theta + \omega)], \tag{3.2}$$

$$q_{\parallel} = K[\sin(\Theta - \omega) + \sin(\Theta + \omega)]. \tag{3.3}$$

3.4 X-ray photoelectron spectroscopy (XPS)

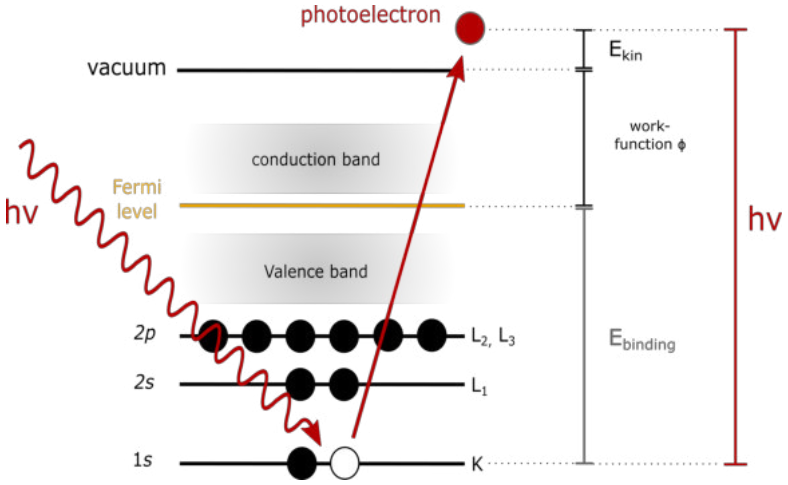

Figure 3.13: Detailed sketch of the Photoeffect. A photoelectron is created by the absorption of a X-ray photon, because the photon energy is high enough to overcome the binding energy of the electron and the workfunction of the material. The atom is left behind with an inner shell hole.

Another highly-used, surface-sensitive analysis tool is X-ray photoelectron spectroscopy [33]. This technique belongs to the class of electron spectroscopy methods, as the measured quantity are the photoelectrons emitted from the sample.

The underlying physical effects (Photoelectric effect and Auger effect) exploited in XPS measurements have already been discussed in Section 2.3. A more detailed consideration of the energies involved in the photoelectric effect is provided in Figure 3.13. The kinetic energy of the photoelectrons E_{kin} depends on the binding energy E_{binding}, the

workfunction Φ and the photon energy $h\nu$

$$E_{\text{kin}} = h\nu - E_{\text{binding}} - \Phi, \tag{3.4}$$

$$E_{\text{binding}} = h\nu - E_{\text{kin}} - \Phi. \tag{3.5}$$

The binding energy of the electron within an atomic orbital is discrete and element-specific, while $h\nu$ and Φ can be assumed constant. Thus, analysing the kinetic energy of the photoelectrons allows to identify the binding energy of their originating atomic orbital.

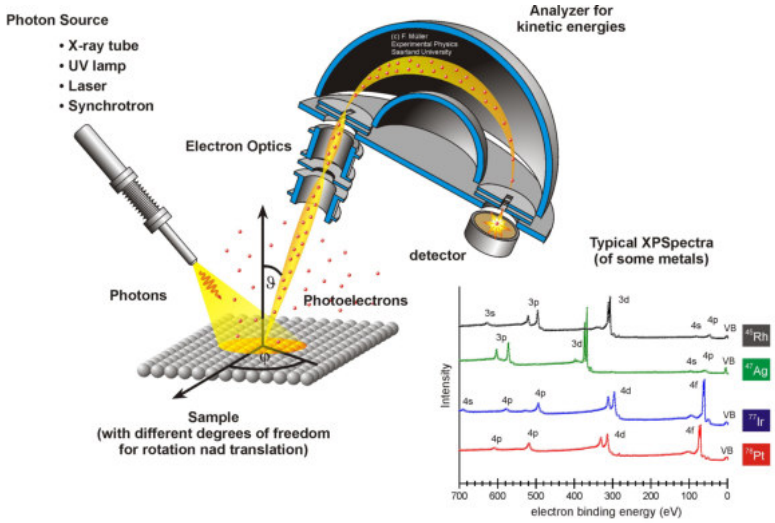

Figure 3.14: Sketch of a typical XPS setup. Reprinted from [34].

A typical experimental XPS setup is shown in Figure 3.14. The sample is irradiated with X-ray photons with a well-defined, and high enough energy to create photoelectrons due to the photoelectric effect. In the measurements used in this thesis an Al K-α source was used, which provides photons with an energy of 1486.6 eV. The kinetic energy of the photoelectrons leaving the surface is measured with an hemispherical analyser. The settings can be tuned to allow only electrons with a specific kinetic energy to pass the analyser. By scanning through the kinetic energy range between the excitation energy and 0 eV, while measuring the amount of electrons detected, it is possible to plot the measured intensity over the kinetic energies of the electrons (see Figure 3.15). As it

can be seen from the illustrative XPS spectrum of a 190 nm-thick In_2O_3 film, sharp peaks, indicating a high amount of measured photoelectrons, are observed at specific binding/kinetic energies. Due to the element- and orbital-specific binding energy it is possible to identify the elements present on the investigated surface. Comparison with XPS databases allows an easy identification of the observed peaks. As shown in Figure 3.15, indium $3s$, $3p$, $3d$, $4s$, $4p$, $4d$, as well as oxygen $1s$ are clearly visible in the presented spectrum. In addition the carbon $1s$ peak is visible, indicating a slight carbon contamination of the surface. Since in a XPS setup free electrons are measured, not only photoelectrons contribute to the XPS spectrum but also Auger electrons. Therefore, additional Auger peaks of In and O are present in the presented spectrum, labelled with In MNN and O KLL. The three letters symbolize the shells, which are involved in the Auger process. In case of the oxygen KLL peak the hole is created in the K shell. An electron from the L shell fills the K shell and an electron from the L shell gains enough energy to leave the atom.

XPS is a very surface-sensitive technique and investigates only the first few nanometres

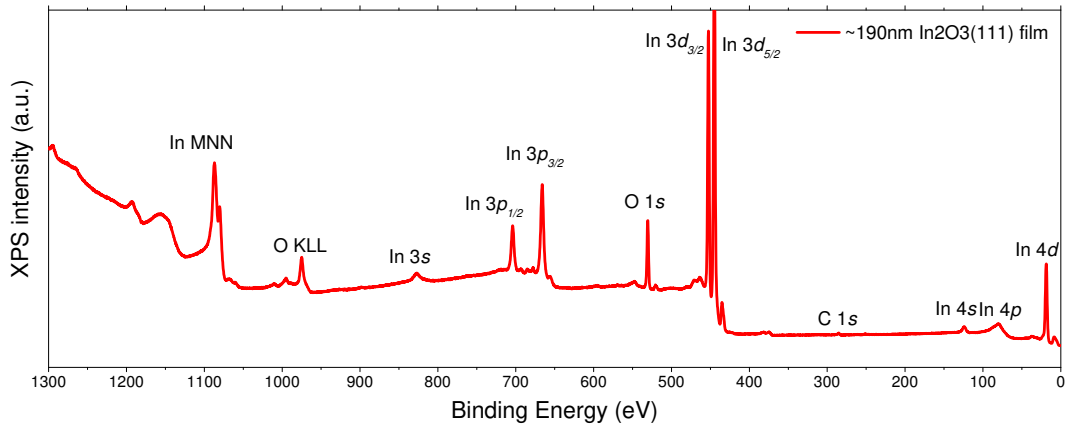

Figure 3.15: XPS spectrum of a 190 nm In_2O_3 thin film on YSZ substrate. It should be noted that the energy axis is denoted in binding energy.

of a solid. The surface sensitivity of XPS is strongly related to the inelastic mean free path of the photoelectrons. The X-rays may penetrate deeper into the bulk, but only photoelectrons which are created in a close distance to the sample surface (in the magnitude of the inelastic mean free path of the photoelectrons, see Figure 2.10) can leave the sample without energy loss. In other words, only the elastically scattered

electrons result in sharp peaks in the XPS signal and can be used to analyse the chemical composition of the surface. Inelastically scattered electrons lose a randomly distributed amount of their kinetic energy and, therefore, exhibit kinetic energies in a broad range, which results in a broad, continuous background signal in XPS measurements.
In general, XPS is used to investigate the chemical composition of the irradiated surface with a detection limit of approximately 0.05 atomic % [33]. It should be noted that it is not possible to detect H or He, due to their small cross section [33]. Furthermore, XPS allows to investigate the chemical environment of the surface atoms. For instance, it is possible to distinguish between the reduced and oxidized form of metal atoms on the surface. Oxidation or reduction causes a slight shift of the binding energies and thus, a slight shift in the measured spectrum.

3.5 Scanning tunneling microscopy (STM)

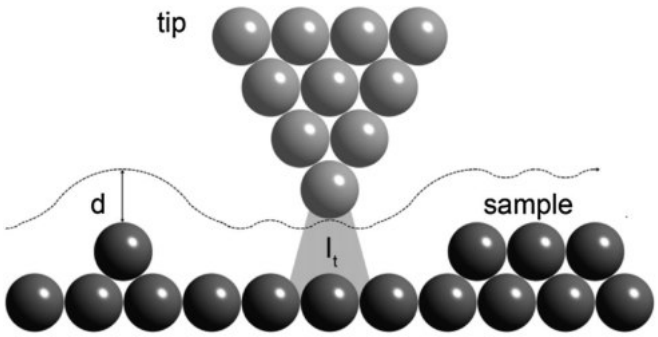

Figure 3.16: Sketch of an atomically sharp tip and atoms of a surface. The tunneling current is shown as I_t. Reprinted from [35].

In contrast to most other surface-sensitive measurement techniques, scanning tunneling microscopy (STM) does not depend on scattering processes and therefore, is an important tool to provide additional information about the surface. STM allows to acquire real space images with atomic resolution of conducting sample surfaces, using a small metal tip that is scanned across the sample. A reasonably flat surface and a conductive sample are the only restrictions for STM samples. The tip is positioned in very close distance to the sample surface ($\sim 1\,\mathrm{nm}$), enabling electrons to overcome the

remaining vacuum gap because of the so called tunneling effect [36, 37]. A theoretical description of the tunneling effect has already been given in Section 2.4. In an STM setup, the surface and the tip are not in direct electrical contact, but due to the tunneling effect, electrons can overcome the thin potential barrier (vacuum) between them [38]. If a voltage is applied between tip and sample, it is possible to measure a small current, as depicted in Figure 3.16. This tunneling current is strongly related to the transmission coefficient and exhibits the same exponential dependence

$$I_{\mathrm{T}} \propto e^{-2\kappa d}. \tag{3.6}$$

STM exploits the high sensitivity of the tunneling current towards changes in the tip-sample distance to gain information about the electronic surface topography.

There are two common operation modes for acquiring STM images, the constant-height mode and the constant-current mode. In constant-height mode the tip is kept at a close and constant position in the direction orthogonal to the sample surface. Scanning across the surface will change the tip-sample distance, resulting in a modulation of the measured tunneling current, which corresponds to the change in the actual surface topography. In constant-current mode the current is kept constant all the time by suitable variation of the distance between tip and sample. These adjusting movements in the z-direction can be realized with piezo electronics in combination with a control feedback loop. The z-signal from the piezo scanner is used to reproduce the topography of the surface. During the imaging process the tip scans the sample surface line by line. At each point, depending on the measuring mode, either the value of the tunneling current or the z-movement of the piezos is measured to record the topography of the surface. It should be noticed that the final STM data show a combination of both, the geometric and electronic topography of the sample surface. The tunneling current is found to be proportional to a convolution of the local density of states of tip and sample surface and the position of the tip [29].

Typical operation conditions are a tunneling current of $0.1 - 1\,\mathrm{nA}$, a gap distance

of $0.5 - 1.5\,\mathrm{nm}$ and a bias voltage of $\pm(1\,\mathrm{mV} - 10\,\mathrm{V})$. If the tunneling current is kept constant in the order of 1-2%, a resolution in z-direction of about 1 pm is possible. The lateral resolution is about 100 pm, which makes it possible to achieve atomic resolution. Due to the high sensitivity of the STM, a proper vibration insulation for optimal performance is required. The system used in this thesis, is equipped with inflatable air-cushions in order to minimize vibrations in the LT-STM.
All the STM images during this thesis were acquired with a low-temperature STM in constant current mode. Typical operation conditions were a gap voltage of $\sim 1.3\,\mathrm{V}$ and a tunneling current of $\sim 0.2\,\mathrm{nA}$.

3.6 Atomic force microscopy (AFM)

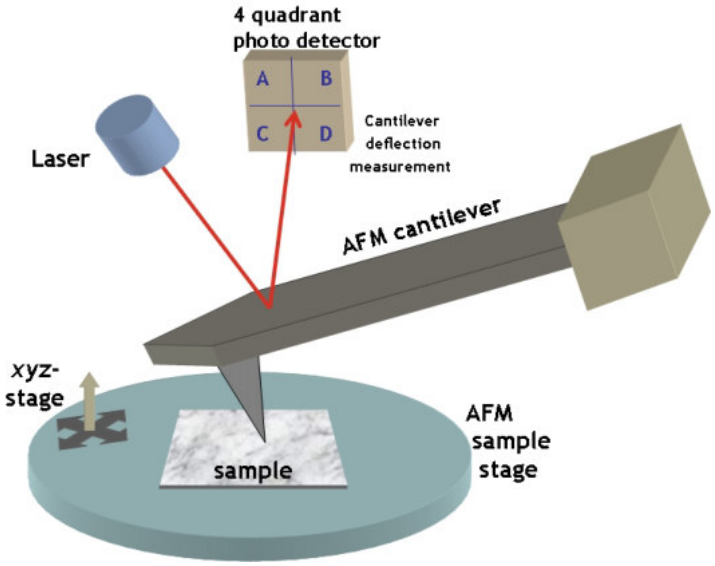

Figure 3.17: Basic sketch of a typical AFM setup using a laser and a position sensitive photo diode to measure the deflection of the cantilever. Reprinted from [39].

Another important surface-sensitive tool to enable high-resolution measurements of non-conductive samples is the atomic force microscope (AFM). The basic principle of the AFM is to exploit the effects of atomic forces, which appear if a tip is placed in very short distance to a sample surface [40]. A basic AFM setup is shown in Figure 3.17. The AFM tip is fixed at the end of a long and flexible cantilever. If the tip is brought close enough to the sample surface, atomic forces will cause a deflection of the cantilever.

Depending on the distance, the cantilever experiences attractive or repulsive forces, as

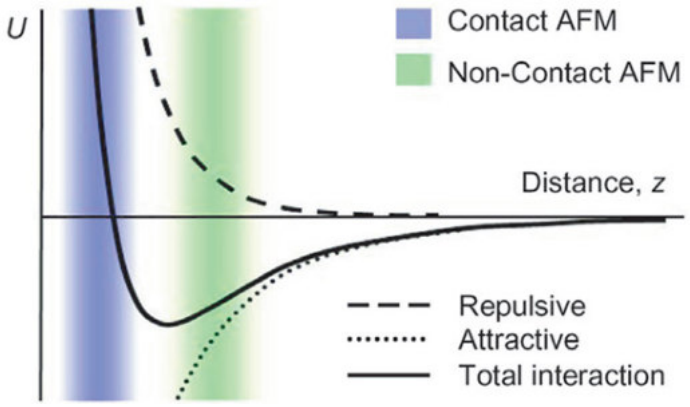

Figure 3.18: Dependence of the effective force on the cantilever as a function of the distance between tip and sample. The green area indicates the typical distance used for non-contact AFM, while the blue area indicates the sample-tip distance used for contact AFM measurements. Reprinted from [41].

shown in Figure 3.18. When the tip-surface distance is small enough ($1 - 10\,\text{nm}$), Van der Waals forces are dominating the tip-sample interaction. The surface atoms and the atoms from the tip are polarized, which results in an attractive potential. If the tip-sample distance is further reduced, the interaction changes to a repulsive potential. The tip-surface atoms are so close to each other that their orbitals overlap. The Pauli exclusion principle prevents the electrons to be in the same state, which results in a strong repulsive force. In this case tip and sample can be considered in contact, so that AFM measurements in the repulsive regime are commonly called 'contact mode' measurements. In this mode the tip is dragged across the surface and the cantilever is bent according to the surface morphology. The deflection of the cantilever is usually detected with a laser and a position sensitive photodiode (4 quadrant photodetector). The laser is reflected from the backside of the cantilever directly onto the 4 quadrant photodetector. A deflection of the cantilever will result in a movement of the reflected laser beam. A controlled feedback loop allows changing the sample-tip distance in order to keep the deflection of the cantilever constant during the measurement. The movement in the z-direction to keep the deflection constant is related to the actual morphology of the surface. Similarly to STM, a combination of the (x, y) scanner position with the measured z-value leads to a 3D-image of the actual surface. Depending on the

surface rigidity, this measurement setup may cause severe damage of the measured area. To avoid a destruction of the sample the non-destructive 'non-contact' mode was used for AFM measurements in the present thesis. In this mode, the the tip is positioned $> 10\,\mathrm{nm}$ apart from the sample surface, where the attractive Van der Waals forces are dominant. The cantilever is forced to oscillate close to its resonance frequency with a certain frequency ω. If the oscillating cantilever is brought close to a surface, the appearing atomic force causes a shift of the resonance frequency. Since the difference between resonance frequency ω_0 and oscillation frequency ω is influencing the oscillation amplitude $A(\omega)$, it is possible to detect the change in amplitude with the position-sensitive photodetector. Again, the oscillation amplitude is kept constant by changing the z-value of the tip position. Further information about AFM is provided in [42]. In this thesis the AFM measurements where performed in air or in an ambient chamber with argon atmosphere in non-contact mode using a silicon tip.

4 Results and discussion

4.1 Preparation of the YSZ(111) substrates

The YSZ samples were first cleaned to get rid of possible contaminations from the industrial polishing process. The 'out of the box' samples were cleaned by sonication in a mixture of Extran (3%) and purified water twice for 30 min (2×30 min), followed by a sonication in purified water (1×10 min).

A simple recipe to achieve well-ordered substrate surfaces, suitable for In_2O_3 growth, was reported in [43] and applied to all prepared YSZ samples presented in this thesis. Following the recipe, the YSZ samples were annealed in a box furnace in air for 1h at 1350 °C (ramp: 8 °C/min) inside alumina crucibles. This recipe produces well-ordered, stepped YSZ surfaces, as it is seen in the AFM images presented in Figure 4.1. After the annealing treatment the YSZ surface is well-ordered in straight, parallel step terraces. The terrace width is dependent on the overall miscut of the YSZ crystal. The measured average terrace size of $\sim$ 100 nm (see line profile at the bottom of Fig. 4.1) corresponds to a miscut angle of 0.17°, consistent with the manufacturer specification ($<$ 0.3°). Furthermore, the step height of the YSZ terraces has been found to be $\sim$ 250 pm. Technical issues with the annealing and the grounding of the In_2O_3-YSZ samples required further preparation of the YSZ crystals, which will be discussed in Sections 4.1.1 and 4.1.2, respectively.

For the sake of completeness it should be mentioned that an additional, short version of the sonication procedure is repeated right before the sample is mounted and inserted into the vacuum chamber. The sonication time is reduced to 2×10 min in Extran and 1×5 min in purified water.

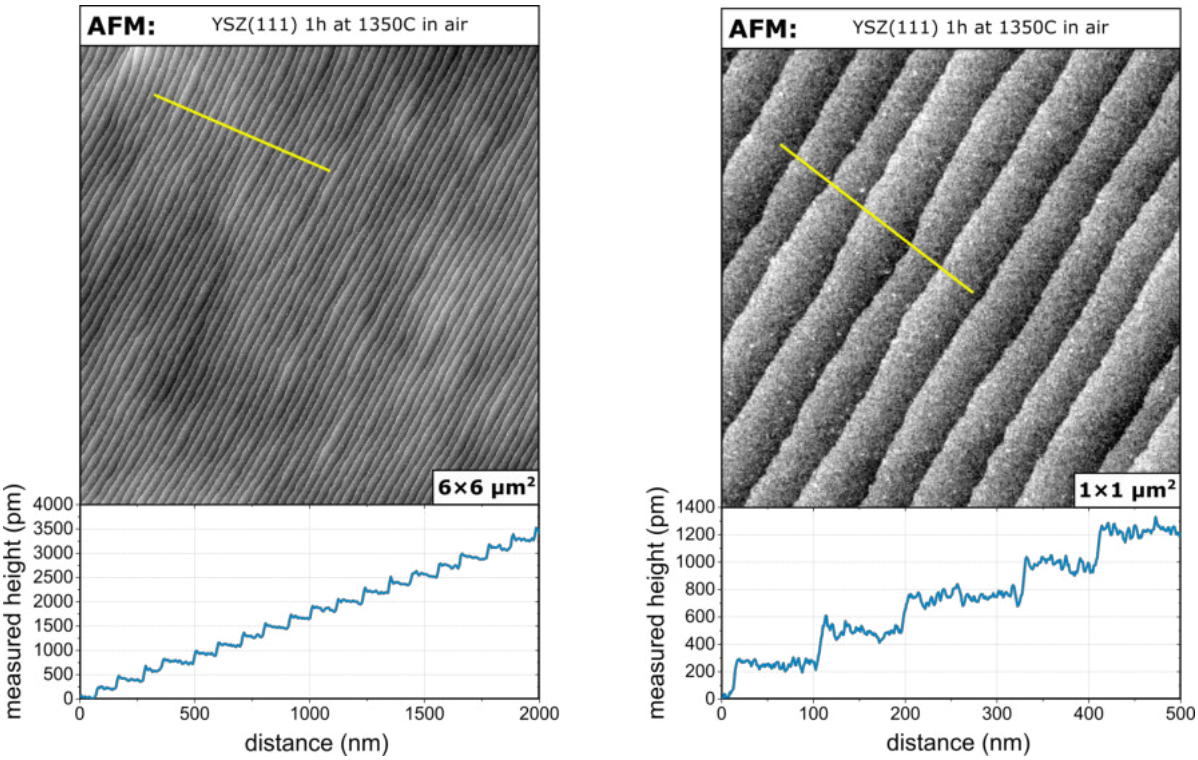

Figure 4.1: AFM images of a clean YSZ substrate after the described pre-cleaning and annealing recipe. The yellow arrows are indicating the position of the line scans.

4.1.1 In-situ annealing of YSZ(111) substrates

As mentioned in Section 3.1, the PLD chamber is equipped with a diode infra-red (IR) laser ($\lambda = 980\,\text{nm}$), which is used to heat up the sample and perform growths at high temperatures. According to the literature, ideal growth temperatures for In_2O_3 growth range from 700 °C to 900 °C [43, 44]. Due to the very weak absorption coefficient of YSZ in the infra-red regime, heating the sample with the IR-laser is not possible. In order to reach the desired growth temperature, a 100 nm platinum layer was deposited on the backside of the YSZ to act as an absorbent layer. Platinum was chosen because it is stable up to more than 1000 °C and because of its good absorption in the infra-red regime. Since the infra-red laser is absorbed by the platinum layer, which is in direct thermal contact to the sample, we were able to reach a stable and uniform temperature distribution across the sample.

To improve the stability of this Pt layer a ∼10 nm-thick titanium interlayer was sputter-deposited between the YSZ surface and the Pt layer. The titanium sticks better to

the flat YSZ surface than the platinum and therefore helps improving the sticking of the absorbing layer. In fact, we observed that sonication of YSZ samples with Pt, but without an additional Ti layer, caused severe damage to the Pt coating. It turned out that applying the deposition procedure twice gives the best results: overall, a 10 nm/100 nm/10 nm/100 nm Ti/Pt/Ti/Pt layer was deposited on the backside of the YSZ substrates.

Thanks to the permission of Prof. Fleig and his group from the Institute of Chemical Technologies and Analytics, the deposition was performed with their magnetron sputtering machine. In order to deposit Ti and Pt on the backside without contaminating the front side we designed a mould with a square hole in the middle to avoid contact with the sample surface. The material of our choice was Teflon because of its high chemical resistance, which allows to clean off the platinum with *aqua regia*. A sketch of the mould and the deposition process is presented in Figure 4.2. It should be emphasized that due to the geometry of the mould, also the sides of the sample become coated with platinum, as presented in Figure 4.2.

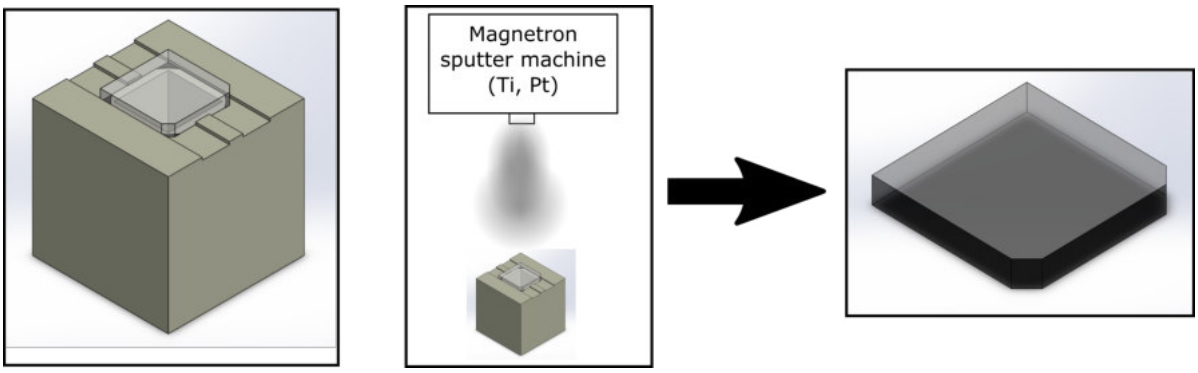

Figure 4.2: Left: Teflon mould with YSZ sample. The polished surface is facing down. Middle: Sketch of Ti/Pt deposition of backside. Right: Sample with Pt at the backside and the sides (depicted in black).

4.1.2 Electrical grounding of In_2O_3–YSZ(111) thin films

The YSZ sample with the Pt layer at the back, mounted on a sample plate, is sketched in the top panel of Figure 4.3. As described in Section 1.2 YSZ is a good insulator. Although, the YSZ is covered with a conducting material during In_2O_3 growth, charging

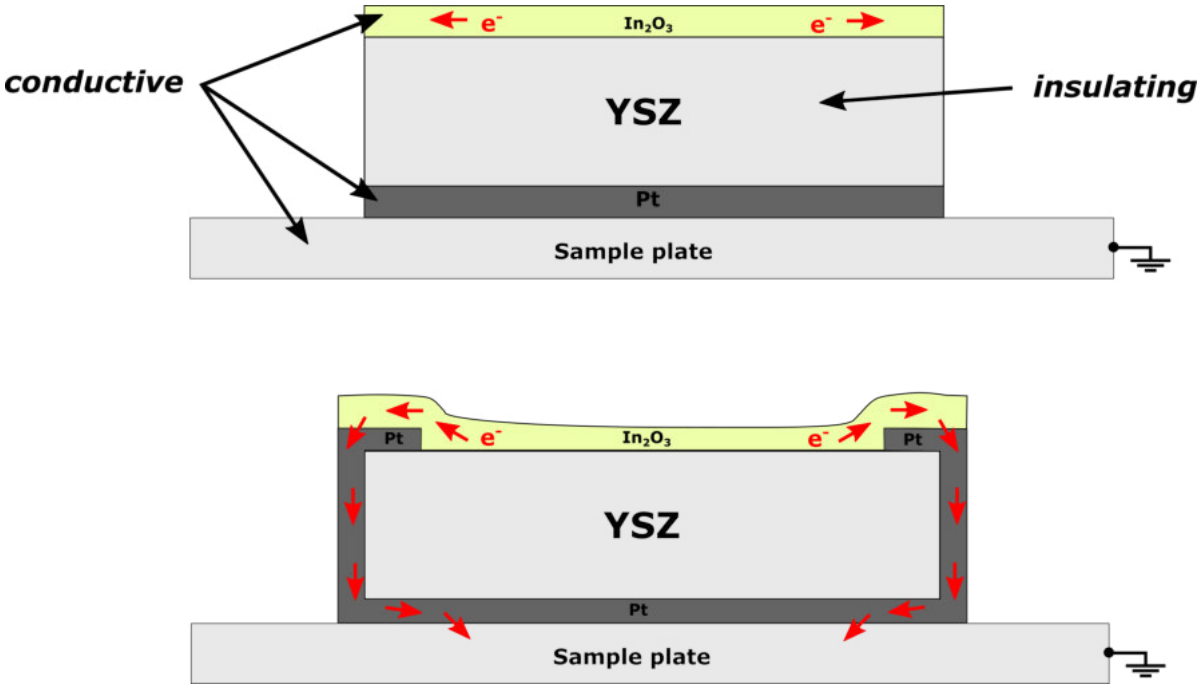

Figure 4.3: Top: Sketch of In_2O_3 thin film on top of a YSZ(111) sample with a Pt layer at the backside. Due to the insulating YSZ the In_2O_3 film is not grounded. Bottom: Sketch of a YSZ(111) substrate with Pt electrodes covered by a In_2O_3 thin film. The grounding of the film is achieved via the Pt electrodes and the platinum-covered sides and backside of the YSZ substrate. The possible electron flow is indicated with red arrows.

of the sample is still a big issue for surface-sensitive techniques such as LEED or XPS. As depicted in the top panel of Figure 4.3, the charging arises from the fact that the In_2O_3 film is electrically insulated due to the YSZ crystal. During LEED measurements for example, the sample is bombarded with low energy electrons, which can not discharge towards the sample plate because of the insulating YSZ.

To avoid these charging problems we came up with the solution of implementing four small Pt electrodes on the polished surface of the YSZ crystal. The idea was to implement the platinum electrodes at the corners of the YSZ sample. Thus, the electrodes would be in electrical contact with the Pt-coated sides and the backside of the sample, as illustrated in the bottom panel of Figure 4.3. Once the In_2O_3 is deposited, the film will bury the Pt electrodes and will ensure electrical contact via the Pt coated sides and the Pt coated backside of the sample to the sample plate, indicated with red arrows in the bottom panel of Figure 4.3.

To implement the Pt electrodes two different approaches where successfully tested in this thesis: a lithographic approach, which uses PMMA, and a mechanical approach, which uses a PEEK mask.

Lithographic approach: Implementing Platinum electrodes using PMMA

The first idea how to implement the platinum electrodes at the corners, while protecting the rest of the polished front surface, was to use a photo resist as a capping layer. The front surface of the YSZ(111) substrates was brushed with Polymethylmethacrylate (PMMA) in such a way that a small area remained uncovered in each corner (see Figure 4.4 a). PMMA is a photo resist used in micro lithography processes. As a next step, the front surface was coated with a 2×(10 nm/100 nm) Ti/Pt layer using the magnetron sputtering machine.
After deposition, the PMMA was removed by sinking the whole sample in acetone. After a few minutes the PMMA is dissolved and removed from the front surface. AFM shows that the surface is completely covered with particles and the steps of the YSZ substrates are not visible, as presented in Figure 4.4 b. Hence, to get the sample atomically clean again a few more steps were required. The sample was too dirty to put it into the chamber to measure XPS, but mainly different carbon species, either due to remains of the PMMA or due to the low quality of the acetone, were expected.
After some failed cleaning methods, which turned out to be too harsh (heating in Piranha solution, boiling in 20% nitric acid) in the end we managed to find a proper recipe to recover an atomically clean surface:

1. Sonication in acetone for 15 min,
2. Sinking in heated acetone at 53 °C for 90 min,
3. Ozone cleaning with 2 h UV,
4. Sonication (heated) in Extran for 40 min,
5. Rinsing in purified water 5 min,
6. Sonication (heated) in Extran for 40 min,
7. Sonication in purified water for 10 min.

While performing steps 1. and 2., it is recommended to use as pure acetone as possible for PMMA removal. In the final recipe a acetone for analysis with a purity of 99.8% was used. In step 3. the sample is put into an UV ozone cleaner. The UV light decomposes the oxygen atoms in the air and forms highly reactive oxygen species *e.g.* ozone which then will interact with all the carbon species on the surface. This treatment was very effective in removing most of the particles on the surface and the residual particles were removed within the next sonication steps. An AFM image of the surface after removal of the PMMA and after the cleaning procedure is provided in Figure 4.4 c.

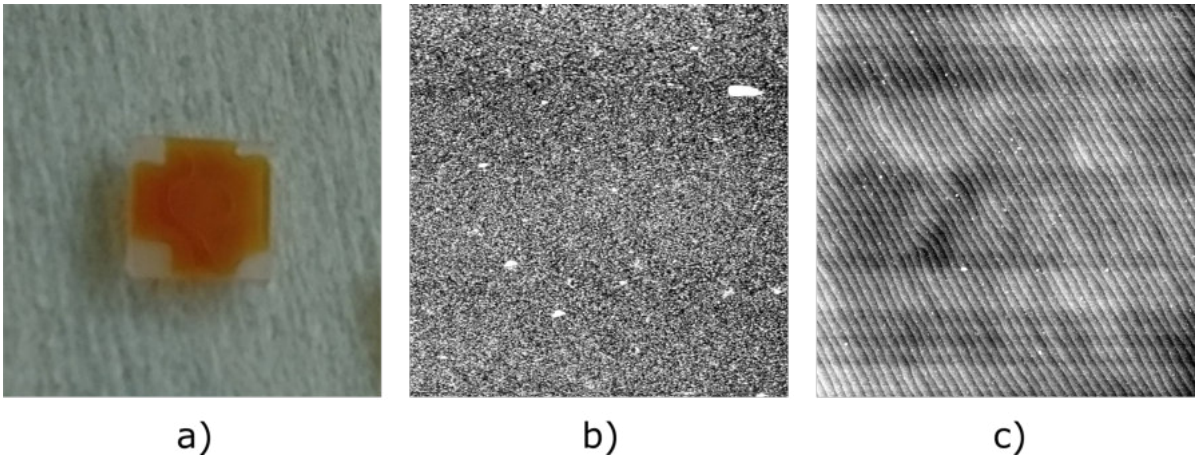

Figure 4.4: a) YSZ sample brushed with PMMA to protect the front surface. Corners are left free b) $6 \times 6\,\mu m^2$ AFM image of a YSZ(111) surface after removal of the PMMA with aceton. c) $6 \times 6\,\mu m^2$ AFM image of a YSZ(111) surface after the cleaning procedure described in the text.

Mechanical approach: Implementing Platinum electrodes using PEEK mask

As described in the previous section, the PMMA solution worked fine and protected the YSZ surface from being covered with platinum. Nevertheless, to clean off the residues from the PMMA and to make the surface atomically clean again was quite involved and time demanding. Thus, we thought of a different and cleaner solution to implement the Pt electrodes. The idea was to simply put a mask on top of the sample, which shades the front surface, except for a small area at each corner. Therefore, we designed a cylinder with a double pocket, to be placed on top of the sample. The cylinder should be smaller than the YSZ sample, in such a way that the corners of the sample protrude

and get coated with platinum. Due to the double pocket, the front surface is touching the mask only at the edges of the sample, which, on the one hand, will not be measured anyway and, on the other hand, will prevent the platinum from creeping underneath the mask onto the YSZ front surface. The mask is presented in Figure 4.5. We decided to use polyether ether ketone (PEEK), because it is harder than Teflon, which makes the production (milling) easier. Furthermore, PEEK (similarly to Teflon) has a very high chemical resistance, which makes it possible to clean off the platinum with aqua regia without etching the mask.

As shown in Figure 4.5, the YSZ sample is put into the mask pocket facing with the polished side downwards. Prior to the deposition, the mask is flipped upside down in such a way that the uncovered corners of the polished YSZ surface are facing the magnetron sputtering machine. This procedure allows to implement the Pt electrodes at each corners, as shown in the bottom right panel of Figure 4.5.

The main advantage of the PEEK mask compared to the PMMA solution is that the polished front surface is not contaminated at any time. The simplicity of the design, the avoidance of complicated cleaning cycles and the achievement of overall cleaner surfaces were decisive to prepare all the presented substrates with Pt electrodes using the PEEK mask.

In addition it should be mentioned that during the Pt electrode deposition the sample is placed onto a glass slide, which can worsen the adhesion of the Pt layer due to contaminations of the sample backside. Thus, the best solution was to coat the backside of the sample before implementing the Pt electrodes.

4.1.3 Mounting of the YSZ(111) substrates

After the annealing, Pt deposition and cleaning process, all the YSZ samples were mounted on sample plates with a hole, using two self-made clips to fix the crystal, as depicted in Figure 4.6. The clips were positioned halfway between the Pt electrodes, keeping two sides of the sample free. This is important to avoid shading the grazing incident electron beam of the RHEED gun. As shown in the bottom right image of Figure 4.6, using a sample plate with a pocket allows to directly heat the sample, thanks to the Pt

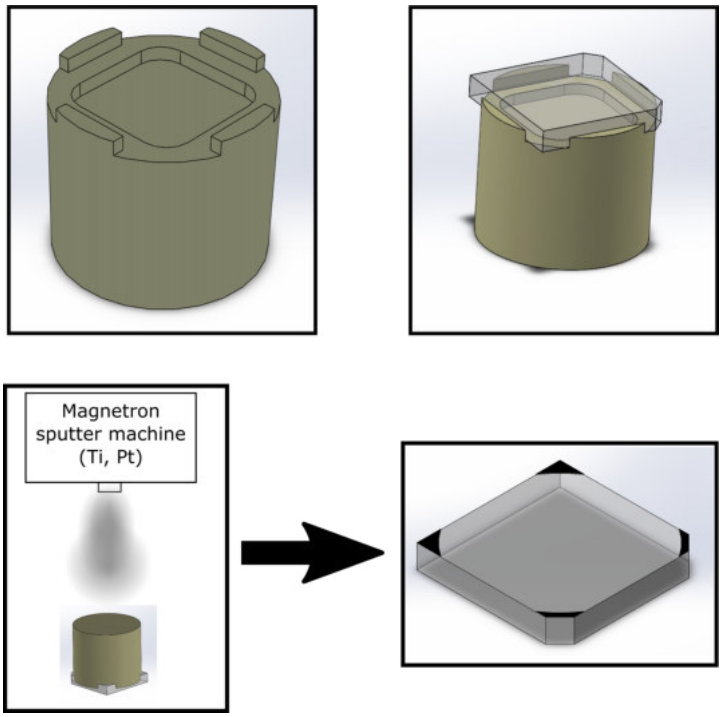

Figure 4.5: Top left: PEEK mask with a double pocket. The inner pocket guarantees that the central part of the polished YSZ surface is not in contact with the mask. Top right: PEEK mask with YSZ sample facing polished side down. Bottom left: Sketch of Ti/Pt deposition of the electrodes. Note that the corners of the sample protrude from the cylindrical PEEK mask. Bottom right: Sample with Pt electrodes (black corners).

absorbent layer, using the infra-red laser of the PLD chamber. The sample plate and the clips are made out of Nicrofer®, which is a Ni, Cr, Fe alloy, suitable to withstand the high temperatures and oxygen pressures that were used during growth.
Due to the fact that the grown In_2O_3 films are intended to be used in different vacuum chambers, the YSZ samples were mounted in such a way that they do not have to be remounted after the growth to ensure electrical contact between film and the sample plate. Mounting the samples as depicted in Figure 4.6, ensures the electrical grounding of the deposited In_2O_3 film, as discussed in Section 4.1.2, with no external grounding solution needed. Avoiding the need to remount and/or ground the In_2O_3 film several times is desired, since each of these processes unavoidably leads to small damages of the grown film.

As already mentioned, temperatures up to 900° C and high oxygen background pres-

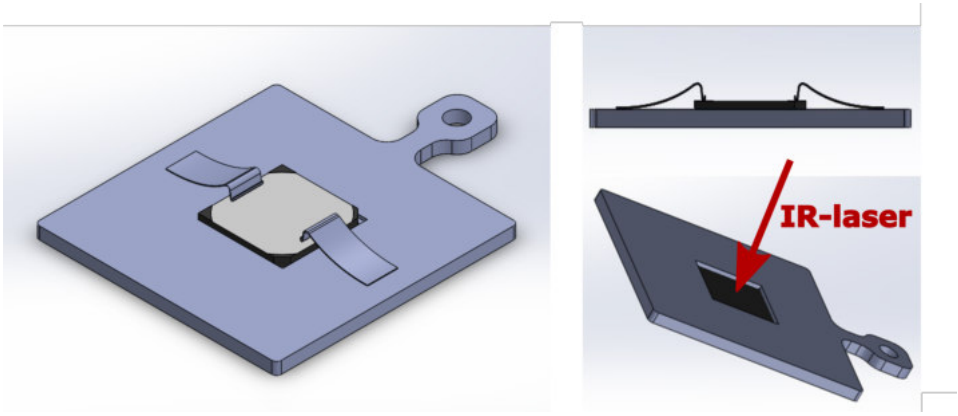

Figure 4.6: Isometric, side and backside view of a mounted YSZ(111) crystals with Pt electrodes. The crystal is mounted on a Nicrofer sample plate with hole using Nicrofer clips. It should be noted that all the samples were mounted with the notches on the right-hand side of the ear, so that the in-plane $[1\bar{1}0]$ direction is accessible by RHEED

sures up to 2×10^{-1} mbar are reached during growth. This leads to the question of the stability of the Ti/Pt layer under these extreme conditions. In general high temperature is equivalent with high diffusion. The question was, if the temperature, in combination with the high oxygen pressure, is high enough to enable diffusion of Pt atoms onto the YSZ surface. Thus, in the beginning some experiments were performed to rule out platinum contamination of the YSZ surface. A YSZ sample with Pt electrodes was heated 1 h up to 900° C in 2×10^{-1} mbar oxygen background pressure. Afterwards the surface composition was investigated with XPS. Figure 4.7 shows a comparison of the XPS data of the annealed YSZ crystal with Pt electrodes with a clean YSZ sample without platinum. The expected, most significant peaks of Pt are highlighted in the yellow box. Nevertheless, neither the YSZ sample without Pt electrodes nor the annealed YSZ sample with Pt electrodes show any suspicious peaks in the marked area. In fact, both spectra exhibit roughly the same features, which leads to the conclusion that the deposited Ti/Pt layer is stable under growth conditions.

After the samples were inserted into the vacuum chamber, they were annealed up to 550° C in UHV in order to obtain a clean sample surface. Furthermore, upon such an annealing, the ratio of Y/Zr peak intensities in XPS increased, suggesting that a partial segregation of Y occurs during the annealing.

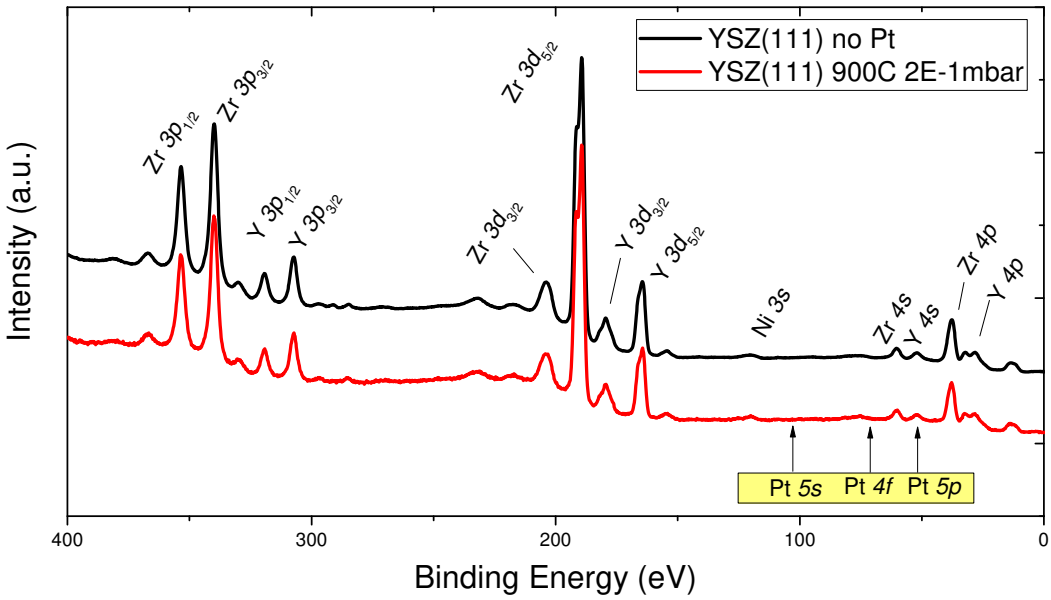

Figure 4.7: XPS spectra of YSZ(111) single crystals. The black curve indicates the spectrum of a YSZ substrate without Pt electrodes, while the red curve indicates the spectrum of the YSZ with Pt electrodes that was annealed up to 900° C in 2×10^{-1} mbar oxygen background pressure. No Pt signal is observed, meaning that the Pt electrodes are stable under growth conditions and Pt does not diffuse onto the surface. It should be noted that the Ni 3*s* from the sample plate or the clips (Ni,Cr,Fe alloy) is visible, indicating a slight misalignment of the X-ray beam.

4.2 Growth mode investigation of In_2O_3 on YSZ(111)

Due to the lack of experience with In_2O_3 growth on YSZ(111), as a starting point literature was consulted for appropriate growth parameters. According to the literature, ideal growth temperatures for In_2O_3 growth range from 700 °C to 900 °C [43, 44]. Unfortunately, [43] reports only on PLD growth of tin-doped In_2O_3 thin films on YSZ(111) substrates, while [44] reports on MBE growth of In_2O_3 thin films on YSZ(111). When trying the same PLD growth parameters, as reported in [43], the results could not be reproduced.

Since the growth parameters from the literature did not lead to the desired results, it was decided to try out different growth parameters, to obtain a better understanding on how the surface morphology is affected by changing parameters such as the growth temperature or oxygen background pressure. An overview of the grown films and a typical

RHEED intensity curve during growth is provided in Figure 4.8. The top-left part of Figure 4.8 consists of a representative RHEED intensity curve during the initial stages of In_2O_3 growth.

As it can be seen, one oscillation of the RHEED intensity is visible, followed by a steady decrease of the signal. This is indicative of a Stranski-Krastanov growth mode (see Figure 3.8). Such a first oscillation was used to estimate the growth rate of each set of growth parameters (temperature/pressure) and achieve a comparable film thickness ($\sim$15 nm). As indicated in the RHEED intensity curve, the peak-to-peak time difference can be measured to calculate the number of pulses that are necessary to grow the first complete Stranski-Krastanov layer. If a constant growth rate is assumed, the latter can be deduced by counting the number of pulses necessary to complete the first layer (p^*). Thus, by measuring the peak-to-peak time difference during growth, it is possible to predict the number of pulses that is necessary to reach a certain film thickness.
Figure 4.8 a-e shows a series of $\sim$ 15 nm-thick films, grown at different growth temperatures and different oxygen background pressures, indicated with a red and blue text color, respectively. As discussed, the number of pulses necessary to complete the first In_2O_3 layer is indicating the growth rate, and is presented in yellow above the corresponding AFM image. The films are ordered with respect to the growth rate from low to high. In the top row of Figure 4.8 two growths at 700 °C, 7×10^{-6} mbar and 900 °C, 2×10^{-1} mbar are presented. The second line of Figure 4.8 presents the AFM images of growths performed at 700 °C and high oxygen pressures ($> 5 \times 10^{-3}$ mbar). As argued in the next section, the grown films can be classified in the following three categories:

- growth at thermodynamic equilibrium conditions (Figure 4.8 a),
- kinetically-limited growth (Figure 4.8 c-e),
- growth close to thermodynamic equilibrium conditions (Figure, 4.8 b).

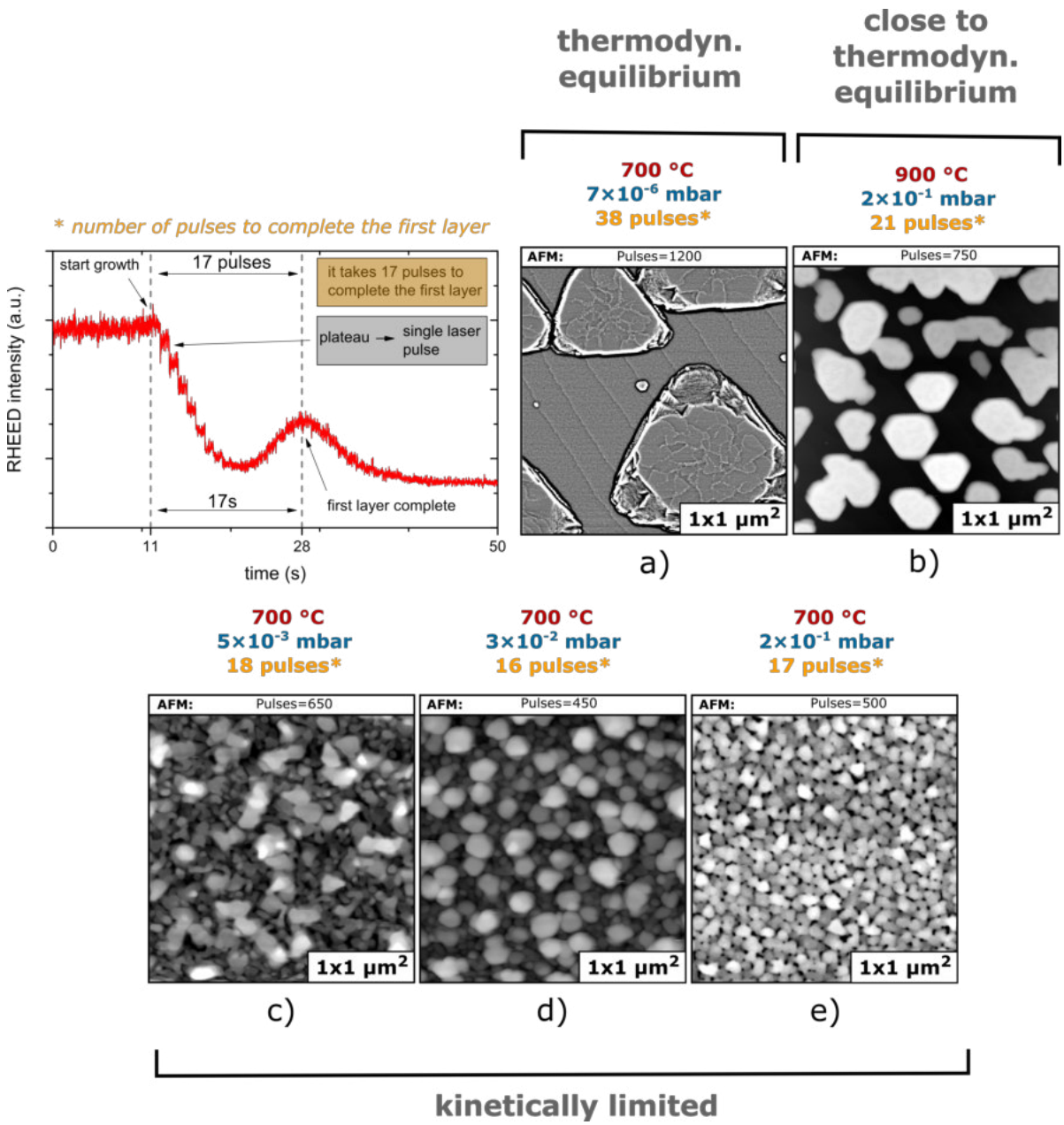

Figure 4.8: Overview of all the growths carried out, in order to investigate the effect of growth temperature and oxygen background pressure on the adopted film morphology. The graph in the top-left corner shows a representative RHEED intensity curve during growth. The number of pulses to complete the first In_2O_3 layer p^* is indicated in yellow.

Growth at thermodynamic equilibrium conditions

For the results presented in Figure 4.8 a, growth was performed at 700 °C and very low oxygen background pressures (7×10^{-6} mbar). At these low oxygen pressures a high reduction of the deposited species is expected. The AFM image presented in Figure 4.8 a shows that the deposited In_2O_3 forms large, triangularly-shaped islands under these growth conditions. The islands are clearly separated from each other and exhibit an average height of ~ 20 nm. The image in Figure 4.8 a is edited with a high-pass filter to allow an easier inspection. Applying a high-pass filter allows identifying mono-atomic steps between the big, triangular islands. The observed modulation of the RHEED intensity during growth is characteristic of a Stranski-Krastanov growth mode characterized by the formation of a flat film layer followed by 3D-island growth. Thus, the steps in the AFM image are most likely steps of the YSZ substrate covered by a single In_2O_3 layer, since the RHEED measurement shows a single oscillation.
The well-ordered appearance of the surface and the exemplary adoption of a Stranski-Krastanov growth mode strongly suggests a growth at thermodynamic equilibrium conditions. Thus, the surface diffusion of the deposited species is high enough to adopt the thermodynamically-favourable shape for In_2O_3 on YSZ(111) substrates, which is apparently equivalent with large, flat-topped triangular islands.
Due to the moderate growth temperature of 700 °C we made the assumption that the reason for the high surface diffusivity has to be related to the oxidation state of the deposited species. Furthermore, this assumption is in good agreement with growth experiments carried out at higher oxygen background pressures, as is discussed later.
The low growth rate (38 pulses to form the first layer) strongly suggest a high re-evaporation rate, leading to an overall low deposition flux Φ for these highly-reducing growth conditions.

Kinetically-limited growth

As is shown in Figure 4.8 c-e, a growth at 700 °C with a high oxygen background pressure ($> 10^{-3}$ mbar) results in a continuous film, consisting of small islands. The AFM results show that the island size decreases with increasing pressure, indicating that the

surface diffusion is reduced with increasing oxygen background pressure (highly oxidized species). In order to qualitatively explain the observed results, one must consider surface diffusion. First, on average, it is more likely for adatoms with a low surface diffusivity to start nucleating a new island, than migrating across the surface to merge with an already existing island. Second, the surface diffusion during high-pressure growth is not high enough to adopt a thermodynamically-favourable surface morphology, which is characterized by large, separated islands, where the exposed substrate surface area is maximized (neglecting the In_2O_3 Stranski-Krastanov monolayer).

Furthermore, analysis of the height profiles of the AFM images shows that the vertical span in the height profile h_{vert} of the films is decreasing from $h_{\text{vert}} = 4\,\text{nm}$ for growth at $5 \times 10^{-3}\,\text{mbar}$ to $h_{\text{vert}} = 2\,\text{nm}$ for growth at $2 \times 10^{-1}\,\text{mbar}$ oxygen background pressure. This reduction can be explained by considering the fact that the low diffusion hinders the In_2O_3 to form the thermodynamically-favourable 3D-islands.

To conclude, growth at an intermediate substrate temperature of 700 °C and an oxygen background pressure $> 10^{-3}\,\text{mbar}$ leads to a significant reduction of the surface diffusion. Thus, In_2O_3 growth at these parameters can be considered as kinetically-limited growth. In addition, Figures 4.8 d-e show that for growth at $3 \times 10^{-2}\,\text{mbar}$ and $2 \times 10^{-1}\,\text{mbar}$ the island size distribution becomes more well-defined as the pressure increases. Moreover, the island size appears smaller and more uniform with increasing oxygen pressure. At an oxygen pressure of $5 \times 10^{-3}\,\text{mbar}$, two categories of islands with different sizes are present on the surface. This leads to the assumption that at a growth temperature of 700 °C and an oxygen pressure of $5 \times 10^{-3}\,\text{mbar}$, the species on the surface starts getting reduced. A mixture of already-reduced and still-oxidized species, and their (assumed) difference in surface diffusivity can be held responsible for the disordered appearance and the difference in size of the film islands. Therefore, the growth presented in Figure 4.8 c can be thought of corresponding to the edge of kinetically-limited growth.

As can be seen from Figure 4.8 c-e, the growth rate (16-18 pulses) is roughly constant at these kinetically-limited growth conditions. Compared to Figure 4.8 a, the growth rate is doubled, indicating a lower re-evaporation rate for highly-oxidized species.

Growth close to thermodynamic equilibrium conditions

As previously discussed, Figure 4.8 a and Figures 4.8 c-e suggest a strong dependence of the observed film morphology on the surface diffusion. Since the growth temperature in those growths is unchanged, the oxidation state of the species is apparently responsible for the difference in surface diffusion. Since growths at high oxygen pressures $\geq 3 \times 10^{-2}$ mbar and a substrate temperature of 700 °C turned out to be kinetically limited (Figure 4.8 c-e), an additional growth at an increased substrate temperature of 900 °C and an oxygen background pressure of 2×10^{-1} mbar was carried out and the result is presented in Figure 4.8 e. The increased growth temperature has a significant effect on the surface diffusion, which is reflected in the adopted surface morphology. Now large, separated quasi-hexagonal islands are formed on the YSZ substrates, instead of a small-grained, continuous film. These islands appear similar, but smaller in comparison to the islands presented in Figure 4.8 a (700 °C, 7×10^{-6} mbar). This fact strongly suggests that the surface diffusion at 900 °C and high O_2 pressures is still not as high as the surface diffusion at 700 °C and very low O_2 pressure.

The effect of the growth temperature on the surface diffusion is evident by comparing Figures 4.8 b and 4.8 e. Since the oxygen background pressure is the same in both cases, the difference in the surface diffusion is solely related to the increased growth temperature. The direct comparison shows that the increase in growth temperature to 900 °C changes the growth from a kinetically-limited to an almost thermodynamically-equilibrated growth. Thus, the diffusion of the species on the surface is high enough to cause a change from a growth characterized by a continuous film with flat islands to a growth resulting in a discontinuous film with separated, large, hexagonally-shaped islands.

At these conditions the growth rate (21 pulses) is slightly lower than the one for films grown at kinetically-limited conditions, and still significantly higher than for the film grown at 700 °C, 7×10^{-6} mbar. At an oxygen pressure of 2×10^{-1} mbar, increasing the temperature from 700 °C up to 900 °C leads to a decrease in the growth rate. This results suggests that the re-evaporation is higher at 900 °C.

4.2.1 Discussion

Considering of the data presented in Section 4.2 allows establishing the following simple qualitative model, based on the experimentally observed behaviour of the grown films. It should be emphasized that further experiments and calculations would be necessary to study the effects of different growth parameters in detail. Based on the available experimental results, it is suggested that the adopted surface morphology is governed mainly by the surface diffusion D and the flux Φ of the deposited atoms, which are in turn related to the oxidation state of the deposited species.

Surface diffusion considerations

According to our assumptions, the diffusion is primarily governed by the kinetic energy of the deposited species, hence, it is controlled by an interplay of substrate temperature and oxidation state of the adsorbed species. It should be noted that the oxidation state is strongly related to the oxygen chemical potential $\frac{1}{2}\mu_{O_2}$, which is controlled by both the oxygen pressure in the chamber, and the substrate temperature. The growth experiments suggest a strong dependence of the surface diffusion on the oxidation state of the deposited species, hence, the oxygen chemical potential is an appropriate quantity to investigate the growth behaviour. Thus, comparing the oxygen chemical potentials at the presented growth conditions, allows to order the growth parameters from the most reducing conditions (low $\frac{1}{2}\mu_{O_2}$) to the most oxidizing conditions (high $\frac{1}{2}\mu_{O_2}$), as presented in Table 4.1.

According to our model (see Table 4.1), strongly reduced In_2O_3 species ($\frac{1}{2}\mu_{O_2} = -1.85\,\text{eV}$) tend to diffuse much faster along the surface than fully oxidized In_2O_3 species ($\frac{1}{2}\mu_{O_2} = -1.42\,\text{eV}$). This can be explained by the fact that the fully oxidized In_2O_3 species can be thought of a complex of an In atom in combination with 1-2 oxygen atoms. If the species are heavily reduced, in an extreme case, it consists only of a single, metallic indium atom. Due to the reduced mass in comparison to the oxidized species, and/or due to a possible change in the bonding energy, the surface diffusion of the reduced species is higher, which is one possible explanation to legitimate the increased surface diffusion

Table 4.1: Comparison of the growth parameters (temperature, oxygen background pressure) and the correspondent oxygen chemical potential. The growth parameters are ordered from reducing conditions (top) to oxidizing conditions (bottom). In addition, the growth rates are evaluated, considering the number of pulses to complete the first In_2O_3 layer (p^*), or considering the compact film height per pulse (h_c). It should be noted that due to the morphology of the kinetically-limited growth it was not possible to calculate h_c at oxidizing conditions. Furthermore, it was not possible to track the RHEED intensity for the growth at 900° C, 1 mbar because of strong scattering of the electron beam at these high pressures.

Growth parameters	$\frac{1}{2}\mu_{O_2}$ (eV)	p^* (pulses)	h_c (pm/pulse)
700° C, 7×10^{-6} mbar	-1.85	38	8.0
900° C, 2×10^{-1} mbar	-1.75	21	11.5
900° C, 1 mbar	-1.67	–	17.4
700° C, 5×10^{-3} mbar	-1.57	18	–
700° C, 3×10^{-2} mbar	-1.50	16	–
700° C, 2×10^{-1} mbar	-1.42	17	–

of reduced In_2O_3 species. In addition, it should be noted that metallic In has a high vapour pressure (5.82×10^{-5} mbar), which reflects small In-In binding energies. This, in turn, can be qualitatively held responsilbe for the enhanced mobility of metallic or strongly-reduced InO_x species. Moreover, [45] reports that under reducing growth conditions it is possible to form the highly-volatile sub-oxide In_2O, with a vapour pressure of $\sim 10^{-6}$ mbar, which is another indication for a high mobility of reduced In_2O_3 species.

Deposition flux considerations

According to our model the second essential quantity to explain the observed film morphology is the deposition flux Φ. On the one hand, the flux is controlled by the amount of material that reaches the substrate. As described in Section 3.2.1, the oxygen background pressure during PLD growth can be used to regulate the amount of deposited material. Due to a high oxygen background pressure, the deposited atoms in PLD growth are scattered significantly by the background gas (broad plasma plume, see Figure 3.4), which is equivalent to a effective reduction of the deposition flux Φ. On the other hand,

the overall deposition flux is also controlled by the re-evaporation of deposited atoms. Moreover, re-evaporation again depends on the kinetic energy, thus on the oxidation state of the adatoms and the substrate temperature. As described above, the increased kinetic energy of the reduced species may lead to an increase of the re-evaporation rate. Additional parameters affecting the deposition flux are either assumed negligible or kept constant during the growth. All the presented growths were performed using the same ablation frequency and fluence (1 Hz, 2 J/cm^2). Thus, a significant change of the deposition flux caused by these parameters is assumed to be very unlikely.

As already described in Section 4.2, a simple way to evaluate the growth rate is by counting the number of laser pulses necessary to form the first In_2O_3 layer on the substrate (p^*). An alternative method to measure the deposition flux consists in evaluating the amount of deposited material, for some selected growths, where the film exhibits the thermodynamically favourable island growth, and the first, continuous In_2O_3 layer of the film is exposed (see Figure 4.8 a-b). Additionally, a growth close to thermodynamic equilibrium conditions at 900 °C, 1 mbar, which is not shown here, is considered in the presented measurements. For these three cases it is possible to evaluate the volume of deposited material present in a $1 \times 1\,\mu m^2$ AFM image by multiplying the area covered by islands A_{island} with the average island height h_{av}. The material necessary to form the wetting layer in the Stranski-Krastanov growth was neglected. For the sake of easier visualization, the deposited volume was divided by the size of the AFM image A_{image}, which allows to define the height of a 'compact' film, assuming the formation of a hypothetical, continuous, flat, layer-by-layer-like film. In order to compare the differences in the deposition fluxes, the evaluated compact film height was divided by the number of pulses n. The compact film height per pulse, h_c, was therefore calculated as

$$h_c = \frac{A_{island} \times h_{av}}{A_{image} \times n}. \tag{4.1}$$

The compact film height per pulse indicates the increased height in picometre per UV laser pulse, which makes it a suitable variable to compare the growth rates.

The results are presented in Table 4.1, which includes the number of pulses to form the first complete layer (p^*) and the compact film height per pulse (h_c). As it can be seen, a similar dependence on the oxygen chemical potential appears: Highly reducing growth conditions ($\frac{1}{2}\mu_{O_2} = -1.85\,\text{eV}$) lead to a low deposition flux, while increasing the oxygen chemical potential (oxidation state) leads to higher deposition fluxes. As discussed in Section 4.2, at an oxygen chemical potential around $-1.57\,\text{eV}$ the growth character changes to a kinetically-limited growth. In this regime the growth rates are not changing much, which suggests almost fully oxidized species on the surface.

The first row of Table 4.1 represents the growth at 700 °C, 7×10^{-6} mbar, which is characterized by very high surface diffusion. At this low oxygen background pressures, the scattering of the plasma plume can be neglected and the low growth rate ($h_c = 7.95\,\text{pm/pulse}$), *i.e.*, the low deposition flux, is solely related to the high re-evaporation rate, due to the highly reduced species on the surface ($\frac{1}{2}\mu_{O_2} = -1.85\,\text{eV}$).

Comparison of the second and third row of Table 4.1 shows a significant change of the growth rate per pulse from 11.5 pm/pulse to 17.4 pm/pulse if the oxygen pressure is slightly increased from 2×10^{-1} mbar to 1 mbar. Apparently the higher oxygen chemical potential is sufficient to oxidize the species on the surface more heavily, and, in turn, decrease the re-evaporation rate significantly. It should be noted that upon increasing the background pressure, a decrease of the rate of impinging species is expected due to the enhanced scattering in the background gas. Nevertheless, this effect appears minor with respect to the enhanced re-evaporation of reduced species, that mostly governs the increase in growth rate with pressure.

A possible explanation to justify the low deposition flux at highly-reducing conditions is provided in [45]. As already discussed, at reducing conditions the volatile sub-oxide In_2O is formed. According to [45] the formed sub-oxide can desorb easily from the surface, resulting in an effectively lower deposition flux. In an extreme case of a pure metallic In growth without oxygen by MBE, 'etching' of the surface can be observed, since the deposited In will form the sub-oxide In_2O with the O from the In_2O_3 substrate, resulting in a reduction of the surface.

4.2.2 Effects of film thickness on the surface morphology

After investigating the effects of different growth parameters (substrate temperature and oxygen background pressure) on the surface morphology of the In_2O_3 films, the effect of changing film thickness is discussed in the following.

Thickness dependence of In_2O_3 films grown at 700 °C, 3×10^{-2} mbar

As discussed in Section 4.2, the growth at 700 °C in high oxygen pressures ($> 10^{-3}$ mbar) leads to a kinetically-limited growth, characterized by small islands completely covering the sample surface. Figure 4.9 shows a film grown with the same parameters as in Figure 4.8 b, but 10× thicker (6500 pulses). The film is still covered with small islands and its appearance did not change significantly. The size of the islands is slightly increased, and they appear more triangular and more ordered. The average island height changed from initially 4.9 nm to 11.5 nm. Thus, increasing the thickness leads to a rougher surface, since the islands apparently do not grow uniformly in height. To conclude, increasing the thickness has no significant impact on the morphology of the deposited film at these kinetically limited growth conditions, apart from a general roughening.

Thickness dependence of In_2O_3 films grown at 900 °C, 2×10^{-1} mbar

The films grown at 900 °C, using a high oxygen background pressure ($2\times10^{-1} - 1$ mbar), exhibit the most promising properties to form a continuous, flat film with increasing thickness. This arises from the fact that the islands are very flat on top and have a roughly uniform height distribution, as it can be seen in Figure 4.8 b. Thus, we assumed that, in an ideal picture, further growth would result in a continuous flat film, due to the fact that the islands will grow in lateral dimensions and in height, and eventually coalesce.

The experimental results of the thickness dependence study of In_2O_3 growth, using a substrate temperature of 900 °C and a oxygen background pressure of 2×10^{-1} mbar, is presented in Figure 4.10. The left image shows the surface of the thin film, which is also presented in Figure 4.8. The denoted film thickness was calculated in a similar way as presented in Section 4.2. Multiplying the number of pulses n with the compact

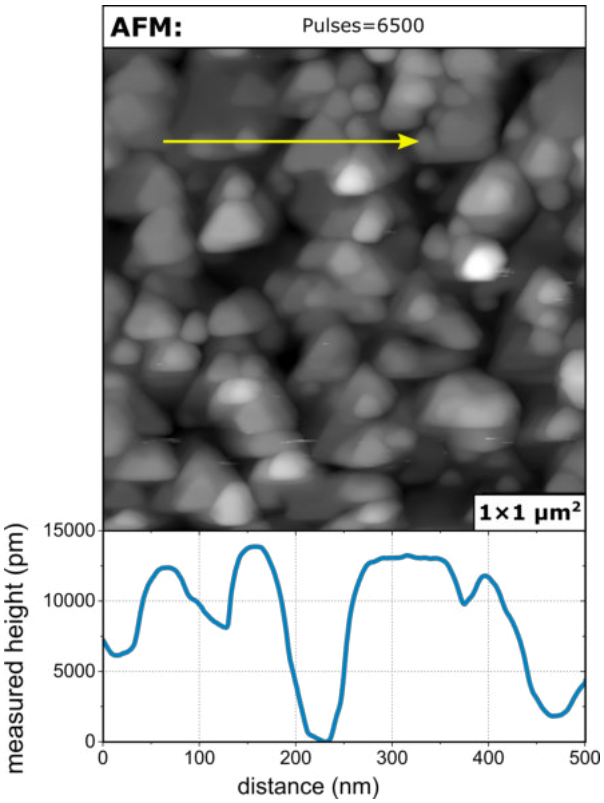

Figure 4.9: ($1 \times 1\,\mu m^2$) AFM image of a In_2O_3 film grown at 700 °C, $3{\times}10^{-2}$ mbar

film height per pulse, h_c, allows to calculate a theoretical film thickness of the compact film. The amount of material deposited on the surface is sufficient to form a 8.5 nm-thick continuous film.

After increasing the thickness by a factor of 10 up to $\sim$ 85 nm, the surface morphology changes significantly, as it can be seen in the central image of Figure 4.10. As predicted, the islands merged to form a continuous film. It should be noted that the film is not perfectly flat, as it exhibits a large number of pits. A line scan across the pits shows that the depth of the largest pits is more than 25 nm. Further growth up to a total thickness of $\sim$170 nm is presented in the right image of Figure 4.10. Doubling the thickness helped to reduce the amount and the depth ($\sim$ 20 nm) of the pits.

It should be noticed that despite the pits, the film was flat enough to measure STM on the 170 nm-thick In_2O_3 film. A $100 \times 100\,nm^2$ overview image of the film is presented in Figure 4.11. The image was measured in a flat area without pits. A detailed STM analysis of the grown films is shown later in Section 4.4.4.

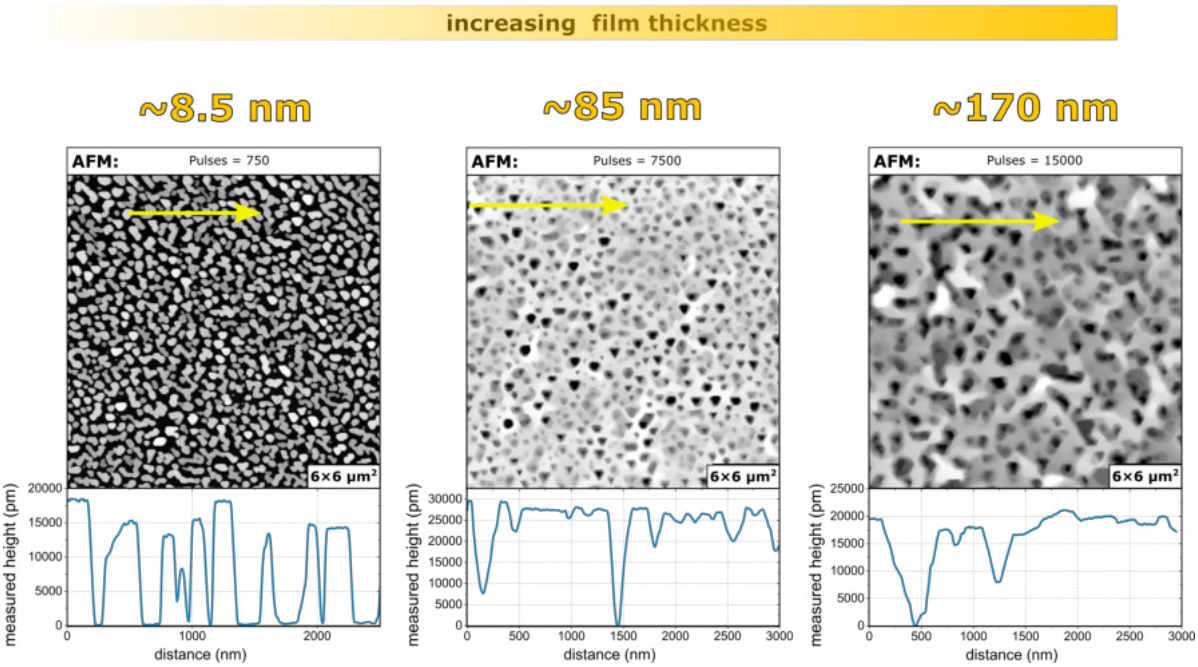

Figure 4.10: Series of ($6 \times 6\,\mu m^2$) AFM images indicating the change in the surface morphology with increasing film thickness.

The origin of the pits can not be evaluated easily and further experiments investigating the formation of the pits would be needed. One explanation could be that the pits are formed when islands merge that have a significant difference in heights merge. In addition, the pits may also help to partly relax the built-up stress within the film due to the lattice mismatch.

4.3 Growth recipe to prepare atomically-flat In_2O_3 thin films on YSZ(111) substrates

Due to the promising results of the STM measurements (see Figure 4.11), the previously presented film can be considered as a successful attempt to grow atomically-flat In_2O_3 thin films. Nevertheless, the surface exhibits many pits, leading to an overall high density of steps, which can, *e.g.*, change the observed behaviour of adsorbed molecules (STM, TPD,...) in comparison to an In_2O_3 single crystal. This fact motivated us to further investigate the growth of In_2O_3 on YSZ(111), aiming for a significant reduction

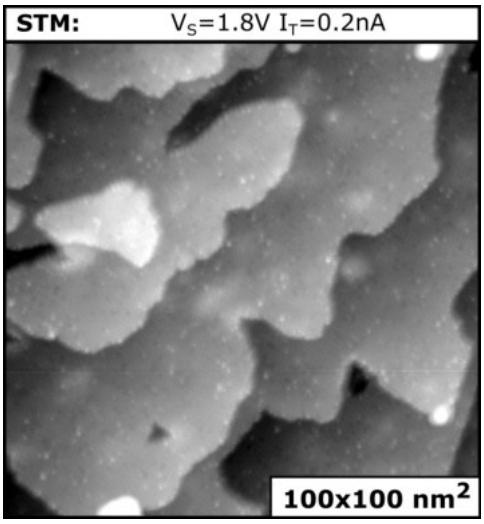

Figure 4.11: STM image of the $\sim 170\,\text{nm}$-thick film grown at $900\,^\circ\text{C}$, $2 \times 10^{-1}\,\text{mbar}$, showing the reduced $In_2O_3(111)$ surface.

of pits on the surface.

Taking into account all the presented effects of growth temperature, oxygen background pressure and film thickness on the surface morphology leads to the following conclusion. Due to the thermodynamically favourable Stranski-Krastanov growth mode of In_2O_3 on YSZ(111) it is not possible to get a flat, continuous film at growth parameters close to thermodynamic equilibrium. In the best case the film is characterized by a rather flat surface, but exhibits many pits. Conversely, if the growth parameters are chosen to promote a kinetically-limited growth, the surface will not exhibit pits, but is characterized by a continuous film consisting of small 3D islands. In order to combine the desired properties of having a flat, continuous film (thick growth at thermodynamic equilibrium conditions) and avoiding the formation of pits (kinetically-limited growth), a combination of both growths was performed. As depicted in Figure 4.12, our growth recipe consists of three main steps:

- Step 1: The first step of the growth recipe is to perform a growth at kinetically-limited conditions ($700\,^\circ\text{C}$, $2 \times 10^{-1}\,\text{mbar}$, $\sim 15\,\text{nm}$). As already discussed, growth at these conditions lead to a flat, continuous film consisting of small islands (see also Figure 4.8 e).

- Step 2: After growth, the temperature is increased up to $900\,^\circ\text{C}$, while keeping the

oxygen pressure constant. The idea is to anneal the grown film at 900 °C for 1 h in order to provide additional kinetic energy, allowing a rearrangement of the atoms to form a film that is as flat as possible.

- Step 3: The final step is to grow a thick film (another 175 nm) on top of the already existing 15 nm-thin film. The growth is performed at 900 °C and an oxygen background pressure of 2×10^{-1} mbar. This growth can be thought of some sort of *homoepitaxial* growth, since In_2O_3 is deposited on a rather flat In_2O_3 thin film. As we saw in Section 4.2, this growth parameters result in flat topped islands, which strongly suggests a layer-by-layer-like growth mode for In_2O_3 on In_2O_3.

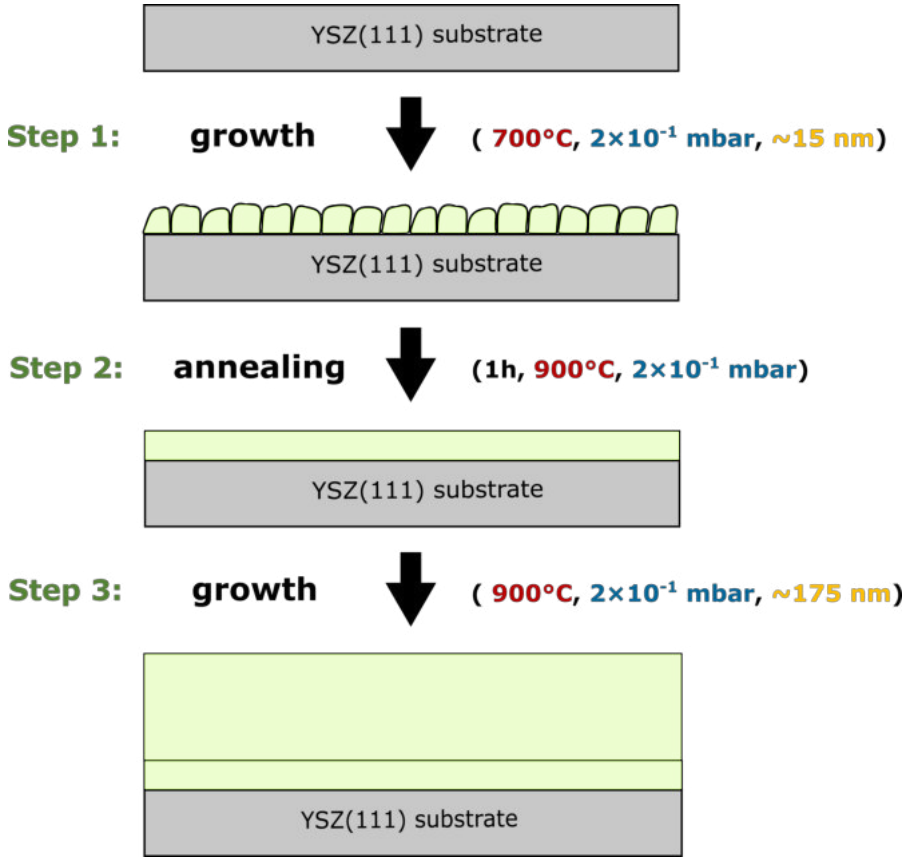

Figure 4.12: Sketch of the recipe which was used to grow atomically-flat In_2O_3 thin films.

It was found that performing the described growth recipe results in In_2O_3 films that exhibit large, well-ordered, mono-atomic terraces. As a result the surface is very flat, and in contrast to the growth presented in Figure 4.10, the film does not exhibit pits.

Figure 4.13 presents an overview of the appearance of the film after each step in AFM, LEED and RHEED.

As expected from the results of Section 4.2, performing Step 1 results in a continuous film with small islands typical for these kinetically-limited growth conditions. The LEED pattern appears a bit blurry, indicating a not perfectly ordered surface. Nevertheless, it is possible to identify the three-fold symmetry of In_2O_3, emphasized by a yellow hexagon. The RHEED diffraction pattern consists mainly of 3D-island-like diffraction spots, which is in good agreement with the AFM results. The Laue circles are barely visible, indicating a weak 2D-behaviour.

Considering Step 2 of Figure 4.13, one sees that the annealing at 900 °C of the thin film indeed provides enough energy to cause a significant change in the surface morphology. AFM reveals that, due to the annealing, the small islands merge and form larger islands. Additionally, the presented surface shows the initial stages of the formation of pits (∼3-4 nm deep), which could be caused by the increased evaporation rate at the substrate temperature of 900 °C. The fact that the annealing leads to a flatter, more ordered surface is also reflected in the LEED and RHEED diffraction patterns. The LEED pattern appears slightly sharper than before the annealing and the RHEED pattern shows a more streaky behaviour and a clearer appearance of the Laue circles, which are both indications for an enhanced 2D-character of the surface.

Growing a ~ 175 nm-thick In_2O_3 layer on top of this film results in a morphology exhibiting large, flat terraces separated by single atomic steps, as can be seen by AFM (see Figure 4.13). Moreover, there are no pits visible. A detailed AFM analysis is presented in Section 4.4.2. The LEED pattern shows very bright and sharp diffraction spots indicating a high crystalline quality of the film surface. Likewise, the RHEED pattern shows an almost perfect 2D-behaviour with very pronounced Laue circles. Furthermore, no 3D-like diffraction pattern is visible.

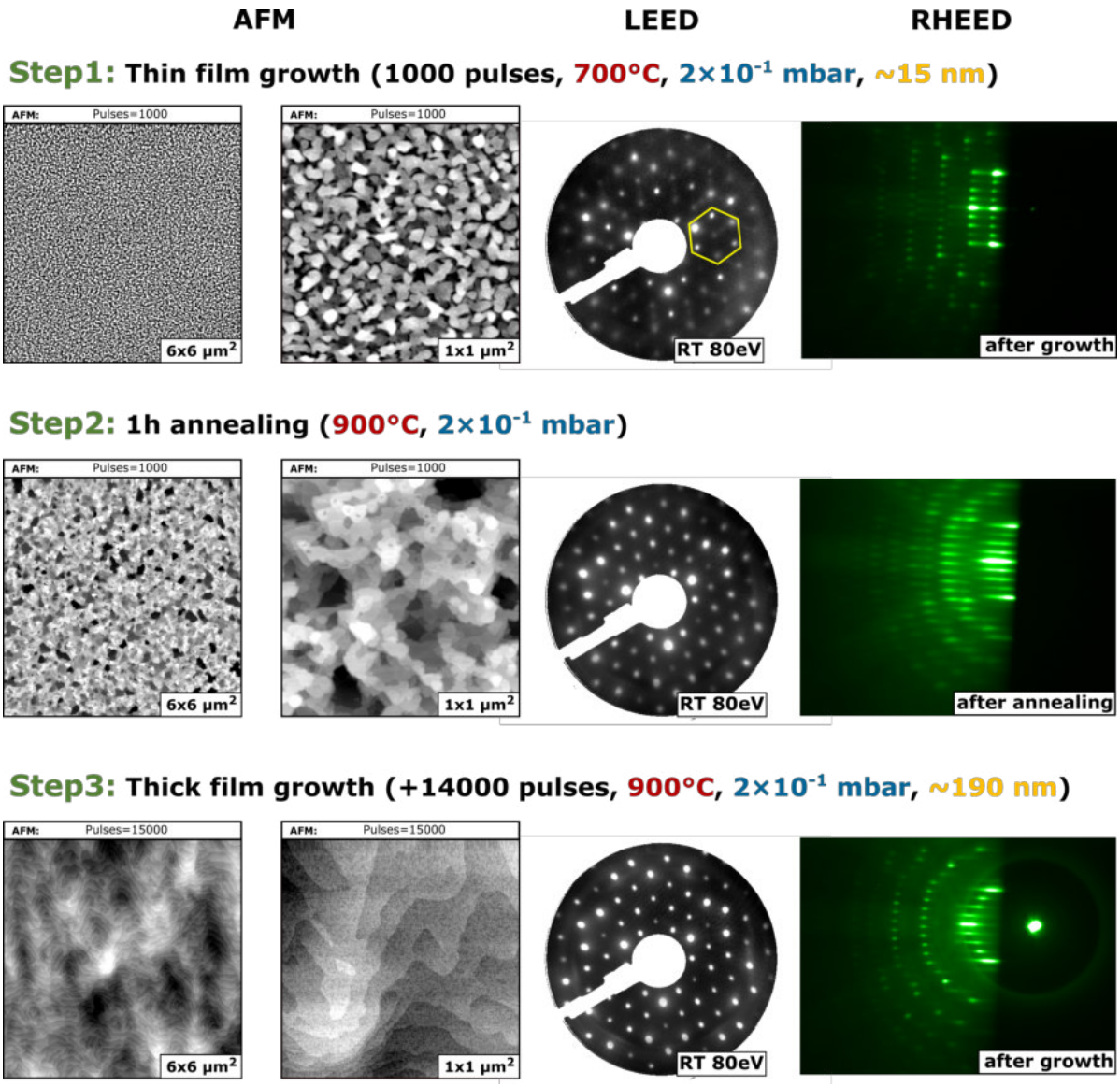

Figure 4.13: Stepwise overview of the growth recipe in AFM, LEED and RHEED.

4.4 Characterization of atomically-flat In_2O_3 thin films

As discussed in the previous section, the final growth recipe made it possible to achieve well-ordered, atomically-flat In_2O_3 thin films. Since the initial goal of this thesis was to provide samples that can be used as a replacement of In_2O_3 single crystals in different experimental setups, the following sections provide a detailed analysis of the final film with various surface and bulk-sensitive techniques. Furthermore, the measurements were

compared with corresponding results from measurements of In_2O_3 single crystals.

4.4.1 XPS measurements

XPS measurements were performed *in situ* on the freshly-grown films to exclude possible contaminations from the environment, and to investigate the surface composition right after the growth. In Figure 4.14, the XPS spectra of three different films are presented together with a spectrum of a bare YSZ substrate.

The blue spectrum represents a characteristic spectrum of a bare YSZ(111) substrate without an In_2O_3 film. In addition to the expected oxygen peaks, the $3p$ and $3d$ peaks of yttrium and zirconium are clearly present. The red curve indicates the XPS spectrum of the flat 190 nm-thick film (Step 3), while the dark-cyan curve indicates the spectrum of the thin film, grown in Step 1 of the growth recipe, at kinetically limited conditions. The XPS spectrum of a film grown at growth parameters close to thermodynamic equilibrium is shown in purple. More precisely, the spectrum belongs to the film grown at 900 °C using a background pressure of 2×10^{-1} mbar (see Figure 4.8 b).

The spectra of all three In_2O_3 films show the characteristic XPS peaks of In and O, which are labelled in Figure 4.14. As it can be seen, the thin film grown at kinetically limited conditions (dark cyan) and the atomically-flat, 190 nm-thick film (red) appear essentially identical in XPS. In both cases no substrate peaks from the YSZ are visible, which strongly suggests a continuous In_2O_3 film. As can be seen from the spectrum of the film grown at conditions close to thermodynamic equilibrium (purple, see also Figure 4.8 b), the substrate peaks of Zr and Y are still visible. Apparently the thin Stranski-Krastanov layer between the In_2O_3 islands is not thick enough to shade the substrate peaks.

The small inset in Figure 4.14 shows that the O $1s$ peak of the YSZ crystal and the one of the discontinuous In_2O_3 film (purple) appear shifted towards higher binding enrgies (~ 6 eV) compared to the O $1s$ peak of the two continuous In_2O_3 films, due to charging. This is arises from the fact that both continuous In_2O_3 films fully cover the insulating YSZ and are in good electrical contact with the Pt electrodes, which ensures electrical grounding of the film. Conversely, the film exhibiting large, separated islands has no

continuous conducting layer. Thus, the sample surface becomes positively charged when the emitted photoelectrons cannot be effectively replenished via electrical contact to the sample plate; thus the apparent binding energy of all peaks increases. Comparison of the O 1*s* peak positions reveal that the charging of the discontinuous film is almost identical to the one of the bare YSZ substrate.

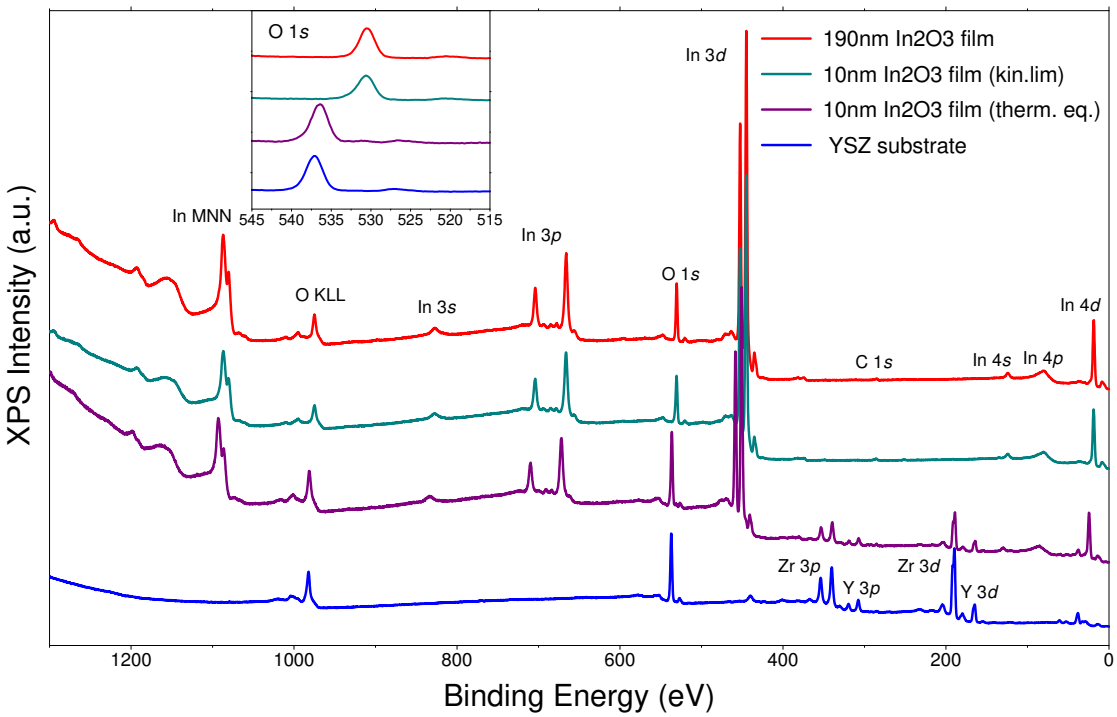

Figure 4.14: XPS spectra of a bare YSZ(111) substrate and In_2O_3 films with different thickness and different growth parameters. The inset shows a detailed scan of the O 1*s* peaks of the samples.

4.4.2 AFM measurements

The sample had to be taken out from the vacuum chamber to perform the AFM measurements. In order to reduce the amount of absorbed water from the atmosphere on the surface, the measurements were performed under Ar flow.

As already briefly discussed, AFM measurements of the film grown according to the presented growth recipe show a flat surface without any deep pits. A detailed illustration of the AFM results including two line scans (yellow arrows) is presented in Figure

4.15. The left panel of Figure 4.15 shows a $6 \times 6\,\mu m^2$ AFM image with a $5\,\mu m$ line scan. The line scan includes the highest and the lowest point of the $6 \times 6\,\mu m^2$ image and shows an overall height difference of only 2.25 nm.
The right panel provides a $1 \times 1\,\mu m^2$ image of the surface, allowing a detailed investigation of the terraces. The line scan shows that the terraces are separated by steps of a magnitude expected for the theoretical step height for the $In_2O_3(111)$ surface according to literature ($\sim$292 pm [11]). To allow an easy comparison, the literature step height is illustrated with an orange arrow in the presented line scan. Furthermore, the line scan suggests a terrace width of roughly 100 nm, while averaging over a large amount of terraces results in an average terrace size of ~ 150 nm. According to STM measurements, the terrace size of a typical In_2O_3 single crystal is in the $20 - 50$ nm range. In addition, AFM shows that the film surface exhibits a large number of screw dislocations (see the orange circles in Figure 4.15). The formation of these screw dislocations most probably is related to the stress within the film due to the lattice mismatch of YSZ and In_2O_3.

4.4.3 XRD measurements and comparison to In_2O_3 single crystal

Subsequently to the AFM measurements, the bulk crystal properties of the grown films were analysed using various XRD measurement techniques. The XRD results of the atomically-flat $\sim$ 190 nm-thick In_2O_3 film (see Figure 4.15) are presented in Figure 4.16. As can be seen, the film was analysed and compared to the results of an In_2O_3 single crystal using the following techniques:

- $\Theta - 2\Theta$ scan (see Figure 4.16 a),
- Grazing incidence detector scan (see Figure 4.16 c),
- Rocking curve measurement (see Figure 4.16 d),
- Azimuthal scan (see Figure 4.16 e),
- Symmetric reciprocal space mapping (see Figure 4.16 f).

The symmetric coupled scan ($\Theta - 2\Theta$ scan) was performed in the Bragg-Brentano geometry to investigate the lattice spacing of the crystal planes along the [111] direction.

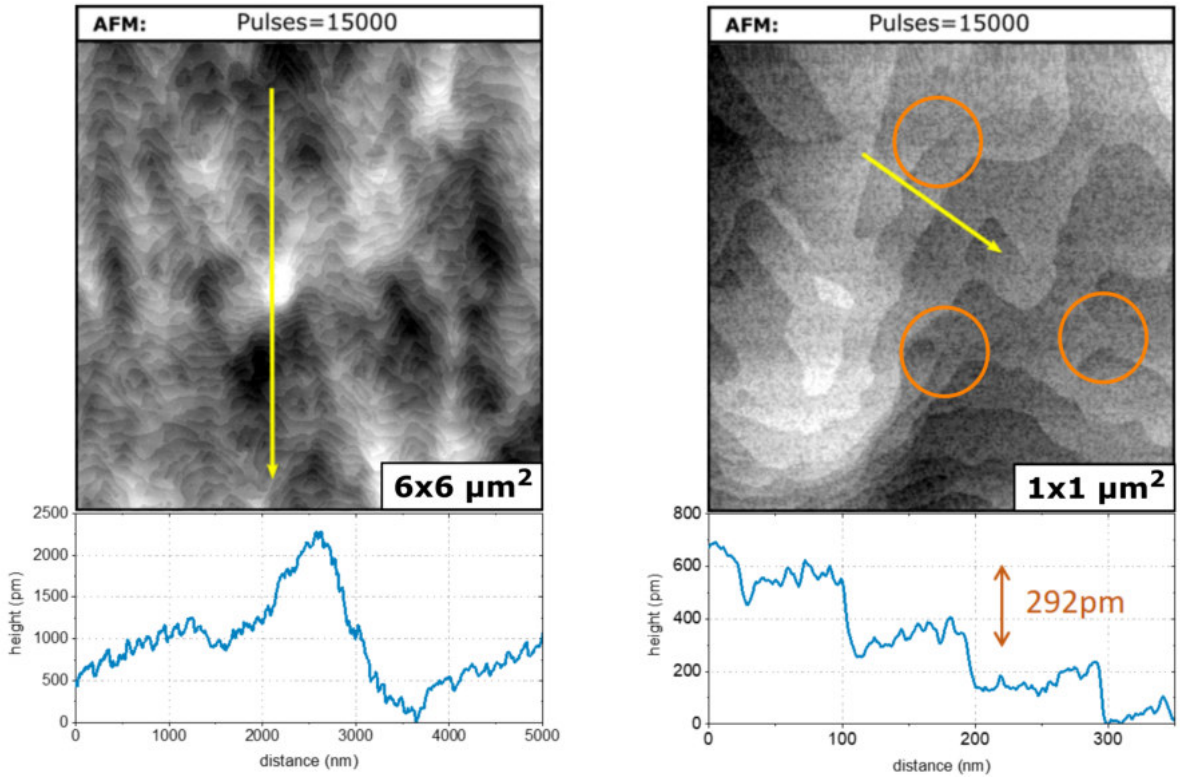

Figure 4.15: A $6 \times 6\,\mu m^2$ and $1 \times 1\,\mu m^2$ AFM images of the surface of a film grown according to the final growth recipe. Line scans are presented at the bottom of each AFM image. The line scan position is indicated with a yellow arrow. The orange circle indicate screw dislocations.

Figure 4.16 a presents the spectra of a $\Theta - 2\Theta$ scan of a In_2O_3 single crystal (black) and the flat In_2O_3 film (red). The red spectrum shows two separated peaks, which are identified as the YSZ(111) and the In_2O_3(222) peaks, by compairing their peak position with the reference values of YSZ and In_2O_3 powder diffraction measurements [46]. These literature values are presented in the inset above the spectra. The peaks are labelled accordingly to their 2Θ position.

Comparison with the spectrum of a In_2O_3 single crystal shows that the In_2O_3(222) peak is shifted about 0.12° to higher values. This shift can be related to the fact that the In_2O_3 film on the YSZ adopts a slightly different structure due to the lattice mismatch of YSZ and In_2O_3. As depicted in the sketch in Figure 4.16 b, the slightly larger in-plane lattice parameter of the YSZ forces the In_2O_3 to expand its unit cell in order to match the substrate during growth. This increase in the in-plane dimensions results in a de-

crease in the out-of-plane lattice parameter in order to preserve the unit cell volume. Thus, the deformation of the unit cell, respectively the induced strain due to the lattice mismatch, causes a reduction of the out-of-plane lattice parameter, which is observed in Figure 4.16 a as a shift of the peak to the right.
Considering the 2Θ value of the In_2O_3 (222) single crystal peak and the X-ray wavelength of 0.1542 nm ($\lambda = 8.04\,\text{keV}$) it is possible to calculated the inter-planar distance between the In_2O_3 (222) planes using the Bragg equation $d_{222} = \frac{\lambda}{2\sin\Theta}$. Performing the same operation, considering the 2Θ value of the grown In_2O_3 (222) film peak, results in an inter-planar distance of 292.4 pm (single crystal) and 291.3 pm (thin film), respectively. The result of the single crystal is in good agreement with the literature value for the step height of the In_2O_3 (111) surface, while the out-of-plane lattice parameter of the grown film is 1.1 pm shorter.

It should be emphasized that the observed film peak at $2\Theta = 30.7°$ is located between the literature values of the (222) cubic and the (104) rhombohedral reflection (see inset of Figure 4.16 a). Despite the plausible lattice mismatch explanation of the observed shift towards higher 2Θ values, further experiments were carried out to prove that the film exhibits a cubic structure and does not adopt the rhombohedral structure of the high pressure phase.
The idea was to measure the reflection of a cubic plane other than the (222) reflection, with no rhombohedral reflection in the immediate vicinity. In order to prove that the film adopts the desired cubic structure, a grazing incidence detector scan was performed to measure the reflection of the cubic (622) plane. The sample was irradiated under very grazing angles ($\omega = 1.1818°$), which made it possible to measure the (622) peak. As presented in Figure 4.16 c, the GID scan exhibits a clear peak close to the literature value of the cubic (622) reflection, which proves that the film indeed exhibits the desired cubic bixbyite structure. Furthermore this setup was used to demonstrate the intrinsic three-fold symmetry of the In_2O_3. First, the intensity of the 622 peak was maximized and then the sample was rotated 360° in plane along the angle Φ. Figure 4.16 e shows that rotating the angle reduces the measured intensity immediately to 0. Further rotation results in a sharp peak at azimuthal angles $\Phi = \pm 120°$. Due to a slight

misalignment of the azimuth rotation axis with respect to the surface normal, the three peaks are slightly different in intensity.

Finally, after proving that the film shows the desired cubic structure, the crystalline quality of the film was investigated by performing rocking curve measurements on the YSZ(222) peak and In_2O_3(444) peaks of film and single crystal, respectively (see Figure 4.16 d). Similarly to a sharp LEED pattern for the sample surface, a sharp rocking curve peak indicates high bulk crystalline quality. As can be seen, the peaks from the YSZ(111) substrate and the In_2O_3 (222) peak of the single crystal are clearly sharper than the In_2O_3 (222) peak of the grown film. This most probably arises from the fact that, again, the In_2O_3 film is under stress due to the substrate underneath. As discussed in Section 2.1, during heteroepitaxial growth the stress increases with the film thickness until it is energetically more favourable to introduce defects (screw dislocations, see also Section 4.4.2). A high number of defects in the lattice is equivalent to a lower crystalline quality and could explain the broadening of the rocking curve peak.

The reciprocal space map, presented in Figure 4.16 f was acquired around the YSZ(222) and In_2O_3(444) diffraction spots. As expected for heteroepitaxial growth, the peaks are clearly separated from each other in reciprocal space, which arises from the different out-of-plane lattice parameters of film and substrate. The corresponding difference in $q_\perp$ confirms the separated peaks of film and substrate observed in the Θ-2Θ measurement. The broader appearance of the In_2O_3(444) peak in comparison to the YSZ(222) peak is in good agreement with the results of the rocking curve measurement, indicating a slightly worse crystalline quality due to stress and/or defects. The clear separation of the two peaks in Figure 4.16 f indicates that there is no thickness-dependent stress gradient within the film. However, from this symmetric measurement it is not possible to distinguish between a pseudomorphic and a fully-relaxed film. A pseudomorphic film exhibits a different out-of-plane-, while a fully-relaxed film is characterized by a different in- and out-of-plane lattice parameter. In order to investigate the in-plane lattice parameter, a reciprocal space map of an asymmetric diffraction spot, characterized by a Q-vector with a non-zero $q_\parallel$-component, is necessary.

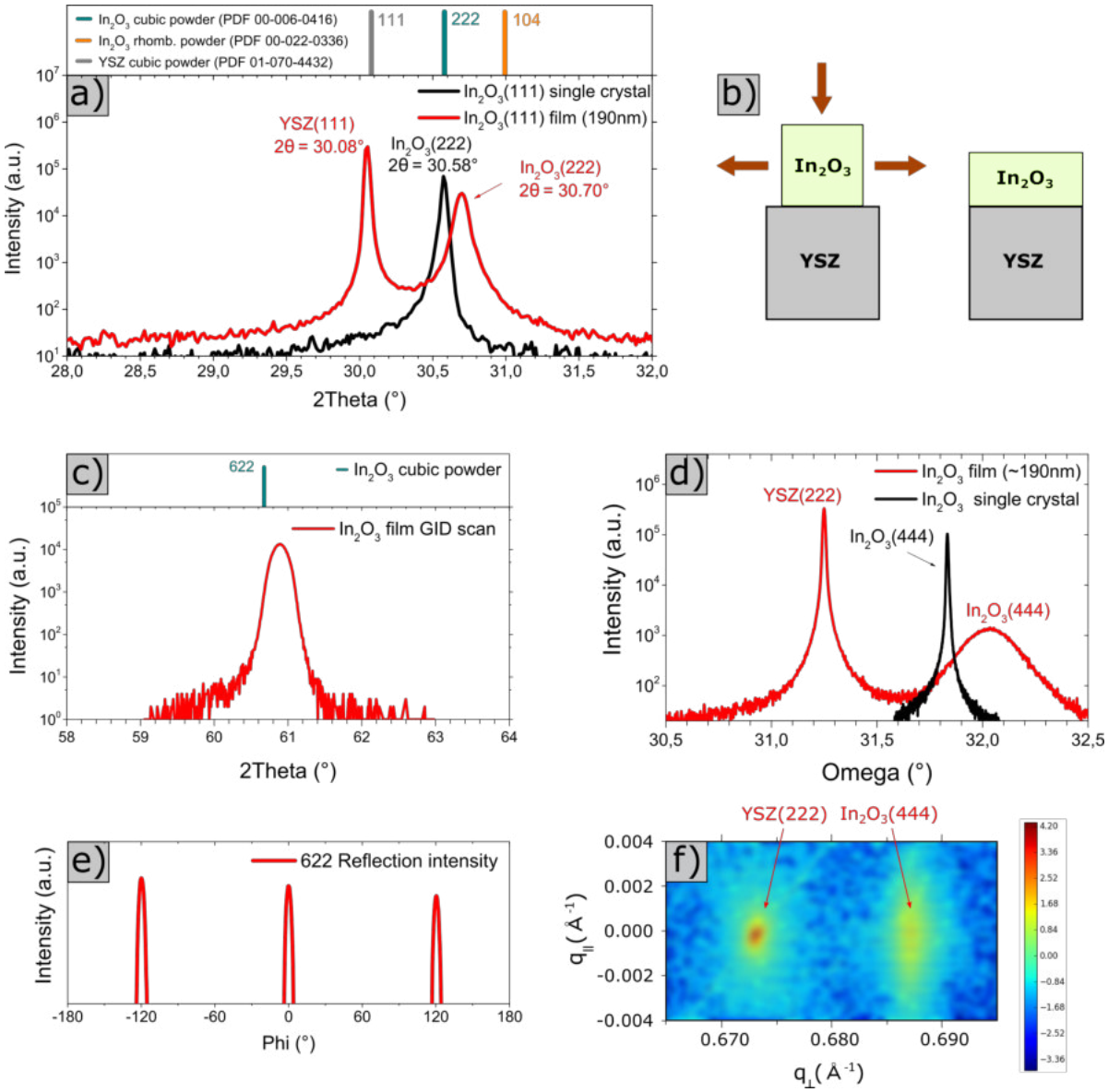

Figure 4.16: Results of XRD measurements performed on the film grown with the growth recipe established in this thesis. Scans of the grown film are presented in red and scans of the single crystal are depicted black.

4.4.4 STM measurements and comparison to In_2O_3 single crystal

As a last step the grown film was measured in STM and compared with the STM results of the (111) surface of a single crystal. Since STM delivers atomic-resolution images, this comparison is of primary importance for our aim to produce samples which can be used as a replacement of In_2O_3 single crystals. The STM images presented in this

section were obtained after the sample (with the film) was annealed up to 550 °C using radiative heating. The temperature was measured using a infra-red pyrometer (emissivity 80%). The annealing was performed in UHV or at an oxygen background pressure of 5×10^{-7} mbar in order to prepare the reduced or oxidized surface, respectively.

Figure 4.17 shows a comparison of the large- and small-scale surface morphology of an In_2O_3 thin film (left) with an In_2O_3 single crystal (right) at STM level. Two large-scale overview STM images ($200 \times 200\,nm^2$) are presented in Figures 4.17 a-b. The large-scale STM image of the single crystal shows well-ordered terraces, running along the diagonal of the presented STM image. The average width of the terraces is approximately 20 nm. The large-scale STM image of the grown film shows that the terraces are not as easy to identify as on the single crystal, as the film exhibits a large number of triangularly-shaped islands (top left corner) or triangularly-shaped pits (top right corner), which protrude exactly one monoatomic step in positive or negative direction, respectively. Line scan i) is drawn across a pit and an island, and demonstrate that the step is indeed one step-height of the $In_2O_3(111)$ surface ($\sim$292 pm). Due to the adoption of a mixture of separated and connected islands, the terraces appear discontinuous and it is hard to define a clear step towards a neighbouring terrace. Nevertheless, it should be emphasized that also the surface of the In_2O_3 single crystal exhibits these mono-atomic pits and protrusions, as highlighted in orange in Figure 4.17 b. Furthermore, the step height of the terraces in both cases, for the single crystal and the grown film, is identical and in good agreement with the literature values, as shown in line scan ii).

As a next step, apart from the large-scale properties, the small-scale appearances of the $In_2O_3(111)$ surface of the film and the single crystal were compared. As presented in [11] and shown in Figure 4.17 iv)-v), it is possible to distinguish two surface structures for the $In_2O_3(111)$ surface, which can be controlled by reducing or oxidizing the surface. As presented in Figure 4.17 c-d, the reduced (111) surface of the film and the single crystal appear very similar. In both cases the presence of the In-adatoms (bright dots) is observed. Additionally, the line scan across the indium adatoms in Figure 4.17 iii) shows that the indium atoms are roughly 1.4 nm apart, which is in good agreement with

the results from [11].
The comparison of the oxidized surface is presented in Figure 4.17 e-f and again shows that the film exhibits the same small-scale characteristics as the single crystal. In both cases the 6-fold coordinated indium atoms, imaged as black triangles, can be identified. Moreover, the unit cell of the reduced and oxidized $In_2O_3(111)$ surface is outlined in yellow in Figure 4.17 c and Figure 4.17 e, respectively.

As described in Section 3.1.2, all the STM measurements were performed in the 'LT-STM' vacuum chamber and the presented images were acquired at 78 K. Once again it should be emphasized that the STM measurements were performed *ex situ*. Thus, after inserting the sample into the LT vacuum chamber, the surface had to be cleaned from possible contaminations using cycles of argon sputtering (10 min, 1 keV, $p_{Ar} = 1.8 \times 10^{-6}$ mbar) and annealing in UHV up to 550 °C for 1 hour. Considering the AFM results presented in Section 4.4.2, the observed surface morphology in STM is not expected, since AFM shows much larger monoatomic terraces. The appearance of smaller island instead of large terraces can be explained considering the sputtering and the annealing at lower temperatures than during growth. During sputtering the surface becomes very rough and apparently annealing at much lower temperatures and oxygen pressure than during growth can not restore the original flatness of the surface. Preliminary trials meant to optimize the annealing temperature have been performed with little success during this thesis, and further, more thorough, investigations still have to be performed at a later stage, as it is discussed in Chapter 6.

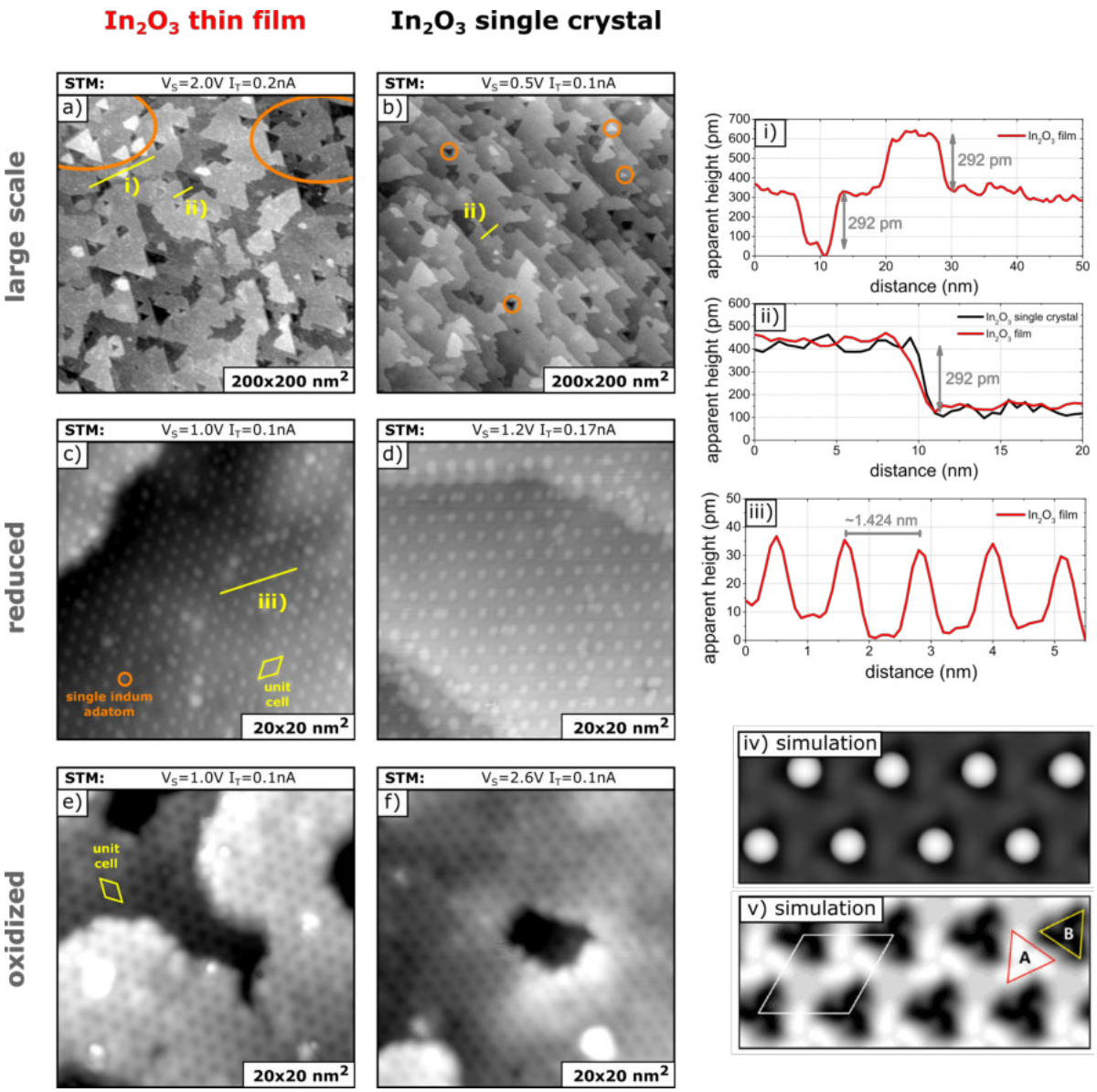

Figure 4.17: Overview of STM measurements. The Figure presents a comparison of the STM images of the grown thin film and the single crystal on a large scale and on a small scale. In addition, line scans, indicated by yellow arrows, and simulated STM images ([11]) of the reduced and oxidized surface are presented.

5 Conclusion

Due to the fact that undoped In_2O_3 single crystals are not commercially available, and synthetically grown ones are usually very small, it is not possible to perform area-averaging techniques such as TPD and XPS. Thus, this thesis was focused on producing atomically-flat, several-hundreds-of-nanometres-thick In_2O_3 thin films, which should serve as promising candidates to be used as an equivalent replacement of $In_2O_3(111)$ single crystals, and which are big enough to be used in a variety of area averaging techniques. The films were grown in a vacuum system equipped with a PLD setup. Commercially available YSZ(111) samples from CrysTec were used as a substrate and the In_2O_3 sputter target was bought from China Rare Metal Material Co., Ltd.

Prior to the growth, the YSZ substrates were cleaned and equipped with Pt-Ti electrodes on the front surface, as well as an infra-red absorbing Pt-Ti layer at the backside of the substrates. During this thesis, a reliable recipe was found to deposit the Pt and Ti with a magnetron sputtering machine, while avoiding a contamination or a destruction of the polished front surface of the YSZ(111) crystals. Furthermore, growing Pt electrodes on top of a YSZ sample ensures electrical grounding of the deposited In_2O_3 thin film.

Due to our lack of experience with In_2O_3 growth and due the fact that growth parameters in the suggested literature did not lead to the desired results, the effect of different growth parameters (growth temperature, oxygen background pressure, film thickness) on the observed growth mode of In_2O_3 on YSZ(111) was investigated as a first step. Trying out different growth parameters allowed us to roughly distinguish between two different observed growth modes. On the one hand, at high growth temperatures ($T = 900\,^{\circ}C$)

or low oxygen background pressures ($p_{ox} \sim 10^{-6}$ mbar) the kinetic energy of the deposited atoms is high enough to adopt the thermodynamically favourable configuration, which turned out to be a Stranski-Krastanov growth mode, characterized by large, separated, flat-topped and triangularly-shaped islands. On the other hand, at high oxygen pressure and low growth temperatures ($T = 700\,°C$, $p_{ox} > 3 \times 10^{-2}$ mbar), the growth appears kinetically limited, since a continuous film consisting of small-grained islands is formed. In both cases, increasing the thickness of the films leads to either rough surfaces (kinetically-limited growth) or rather flat surfaces exhibiting many deep pits (thermodynamically equilibrium growth).

In order to obtain an atomically-flat In_2O_3 film without pits, a combination was performed, combining the desired effects of both growth conditions. The idea, namely to grow a film at kinetically-limited conditions, which covers the whole sample surface, followed by annealing at high temperatures and high oxygen background pressure, in order to obtain a film as flat as possible, turned out to work well. The small islands merged to form larger and overall flatter islands due to the increased surface diffusion at higher temperatures. Growing at growth conditions close to thermodynamic equilibrium ($T = 900\,°C$, $p_{ox} > 3 \times 10^{-2}$ mbar) on top of the thin In_2O_3 film resulted in growth exhibiting a step-flow growth mode character, and in very flat In_2O_3 films.

In the end, the produced atomically-flat In_2O_3 films were thoroughly characterized by different surface- and bulk-sensitive techniques. Furthermore, the results were compared to measurements on In_2O_3 single crystals, in order to demonstrate that our film indeed behaves similarly, and exhibits the same properties as the single crystal itself. *In-situ* XPS measurements were performed in order to demonstrate the cleanliness of both, the substrate before, and the In_2O_3 film after the growth. A detailed AFM analysis reveals that these films exhibit large terraces (∼150 nm) separated by monoatomic steps. Furthermore, there were no pits observed on a large $6 \times 6\,\mu m^2$ image. XRD revealed that the film adopts the cubic bixbyite structure, while being under in-plane tensile stress because of the small lattice mismatch with the substrate, resulting in a slightly worse crystalline quality compared to a single crystal. Nevertheless, the goal to produce

well-ordered, atomically-flat In_2O_3 films, which can replace In_2O_3 single crystals, can be considered as a success, due to the fact that STM investigations show a very good agreement with the STM results of In_2O_3 single crystals. Since STM provides surface images with atomic resolution, a similar appearance in STM was considered as a key requirement to support our claim that the surface of the single crystal and of the grown film behave similarly. The film adopts a comparable large-scale morphology as the single crystal, and it was possible to observe both, the oxidized, as well as the reduced $In_2O_3(111)$ surface reconstruction similarly to what is reported in the literature [11]. Therefore, the STM results strongly promotes the use of the grown films as an equivalent single crystal replacement in different experimental setups.

6 Outlook

Despite the satisfying results achieved during this work, there is still some room for improvement and for more detailed investigations.
The growth mode investigations, which were performed during this thesis, only allowed us to establish a rough model of the complicated processes occurring during growth. As stated in Section 2.1, further experiments would be necessary to investigate the growth behaviour and the effects of changing growth parameters in detail. Our model strongly suggests a sensitive balance of surface diffusion and re-evaporation, which are both strongly dependent on the oxidation state (oxygen background pressure) and the substrate temperature. Further growths would have to be performed in order to improve the fine tuning of this parameters.
Moreover, it should be stated that the presented growth recipe to produce atomically-flat In_2O_3 thin films was not 100% reproducible, and in some cases resulted in flat surfaces with a small number of pits. Again, this problem would require a better understanding and improved growth parameters in order to avoid the formation of the pits. In general it would be necessary to investigate the formation of the pits in detail, since the presented experiments have not revealed a reasonable conclusion to explain their formation.
Nevertheless, during this thesis we succeeded to produce atomically-flat In_2O_3 thin films, which appear promising candidates to be used as a single crystal replacement in future experiments. Especially, in order to do perform TPD measurements, which require a high number of sputtering and annealing cycles, it is of crucial importance to find an optimized recipe to prepare the film surface after sputtering. Thus, further trials to investigate the optimum annealing temperature and annealing time for the grown films still have to be performed. In fact, it turned out that In_2O_3 apparently is very sensitive towards annealing in vacuum, since the film is very easily reduced. In a worst case

scenario, a too high annealing temperature in UHV (probably in the range of 900 °C) can lead to an almost complete de-wetting of the film. Additionally, it was observed that too high and too long annealing in UHV led to a strong reduction of the film, characterized by the formation of $1 - 2$ nm-deep trenches. This fact again emphasizes the importance of identifying the optimum annealing parameters, which, in the best case, will also help to further improve the surface morphology of the film after sputtering.

7 Acknowledgement

First of all, I want to give thanks to my family and my study colleagues, who supported me and gave me the possibility to complete this thesis. A special thanks goes to my girlfriend for all the productive working sessions at her place and for her help to overcome all the small (linguistic) obstacles while writing. Additionally, I would like to express my gratitude to all the members of the Surface Physics Group at the Vienna University of Technology for their help and time and the good working atmosphere, which I was allowed to enjoy the last 10 months. Moreover, I would like to give a special thanks to the head of this group Prof. Ulrike Diebold for her supervision and for the opportunity to write my diploma thesis. I would like to express my very great appreciation to my supervisors Dr. Michele Riva and Dott.mag. Giada Franceschi for their help and guidance in the lab as well as during the writing process. Without their great effort and enthusiasm it would not have been possible to complete this work.

8 Bibliography

[1] P. D. C. King, T. D. Veal, F. Fuchs, C. Y. Wang, D. J. Payne, A. Bourlange, H. Zhang, G. R. Bell, V. Cimalla, O. Ambacher, R. G. Egdell, F. Bechstedt, and C. F. McConville, "Band gap, electronic structure, and surface electron accumulation of cubic and rhombohedral In_2O_3," Phys. Rev. B **79**, 1 (2009).

[2] C. I. Bright, "50 years of vacuum coating technolgy and growth," (Society of Vacuum Coaters, 2007) Chap. Review of Transparent Conductive Oxides (TCO).

[3] C. G. Granqvist and A. Hultaker, "Transparent and conducting ITO films: new developments and applications," Thin Solid Films **411**, 1 (2002).

[4] D. S. Ginley, H. Honsono, and D. C. Paine, *Handbook of Transparent Conductors* (Springer, 2010).

[5] R. G. Egdell, "Defects at Oxide Surfaces," (Springer, 2015) Chap. Chapter 12: Dopant and Defect Induced Electronic States at In_2O_3 Surfaces.

[6] A. Galdikas, Z. Martunas, and A. Setkus, "SnInO-based Chlorine Gas Sensor," Sens. Actuators, B **7**, 633 (1992).

[7] T. Takada, K. Suzuki, and M. Nakane, "Highly sensitive ozone sensor," Sens. Actuators, B **13**, 404 (1993).

[8] H. Yamaura, T. Jinkawa, J. Tamaki, K. Moriya, N. Miura, and N. Yamazoe, "Indium oxide based gas sensor for selective detection of CO," Sens. Actuators, B **36**, 325 (1996).

[9] K. K. Ghuman, T. E. Wood, L. B. Hoch, C. A. Mims, G. A. Ozin, and C. V. Singh, "Illuminating CO_2 reduction on frustrated Lewis pair surfaces: investigating the role of surface hydroxides and oxygen vacancies on nanocrystalline $In_2O_{3-x}(OH)_y$," Phys. Chem. Chem. Phys. **17**, 14623 (2015).

[10] L. B. Hoch, T. E. Wood, P. G. O'Brien, K. Liao, L. M. Reyes, C. A. Mims, and G. A. Ozin, "The Rational Design of a Single-Component Photocatalyst for Gas-Phase CO_2 Reduction Using Both UV and Visible Light," Adv. Sci. **1**, 1400013 (2014).

[11] M. Wagner, S. Seiler, B. Meyer, L. A. Boatner, M. Schmid, and U. Diebold, "Reducing the In_2O_3(111) Surface Results in Ordered Indium Adatoms," Adv. Mater. Interfaces **1**, 1 (2014).

[12] M. Wagner, J. Hofinger, M. Setvin, L. A. Boatner, M. Schmid, and U. Diebold, "The prototypical organic-oxide interface: intra-molecular resolution of sexiphenyl on In_2O_3(111)," Submitted.

[13] M. B. Maccioni, F. Ricci, and V. Fiorentini, "Properties of $(Ga_{1-x}In_x)_2O_3$ over the whole x range," J. Phys.: Condens. Matter **28**, 224001 (2015).

[14] E. Morales, *Growth and surface characterization of tin-doped indium oxide thin films*, Ph.D. thesis, Tulane University (2010).

[15] E. H. Morales, Y. He, M. Vinnichenko, B. Delley, and U. Diebold, "Surface structure of Sn-doped In_2O_3(111) thin films by STM," New J. Phys. **10**, 1 (2008).

[16] P. W. Tasker, "The stability of ionic crystal surfaces," J. Phys. C **12**, 4977 (1979).

[17] University of Cambridge, `https://www.doitpoms.ac.uk/tlplib/fuel-cells/printall.php`, accessed: 2017-12-19.

[18] S. Ikeda, O. Sakurai, K. Uematsu, N. Mizutani, and M. Kato, "Electrical conductivity of yttria-stabilized zirconia single crystals," J. Mater. Sci. **20**, 4593 (1985).

[19] R. Stevens, *An introduction to zirconia* (Magnesium Elektron LTd., 1986).

[20] K. Oura and V. Lifshits, "Surface science," (Springer, 2003) Chap. Growth of Thin Films.

[21] H. Lüth, "Solid Surfaces, Interfaces and Thin films," (Springer, 2010) Chap. 4 Scattering from Surfaces and Thin films.

[22] M. Birkholz, *Thin Film Analysis by X-Ray Scattering* (Wiley-VCH, 2006).

[23] C. D. N. Chan, `https://commons.wikimedia.org/wiki/File:Diffusion{_}rayleigh{_}et{_}diffraction.png`, accessed: 2017-12-11.

[24] G. Wang and T. Lu, "RHEED transmission mode and pole figure," (2014) Chap. 2.

[25] W. L. Bragg, "The Diffraction of Short Electromagnetic Waves by a Crystal," (1913) pp. 43–57.

[26] C. Hammond, *The Basics of Crystallography and Diffraction* (Oxford University Press, 2015).

[27] A. Zangwill, *Physics at Surfaces* (Cambridge University Press, 1988).

[28] J. Tersoff and D. R. Hamann, "Theory and application for the scanning tunneling microscope," Phys. Rev. Lett. **50**, 1998 (1983).

[29] J. Tersoff and D. R. Hamann, "Theory of the scanning tunneling microscope," Phys. Rev. B **31**, 805 (1985).

[30] R. L. Weiher and R. P. Ley, "Optical Properties of Indium Oxide," J. Appl. Phys. **37**, 299 (1966).

[31] M. Henzler and W. Göpel, *Oberflächenphysik des Festkörpers* (Teubner Verlag, 1994).

[32] G. Held, "Low-energy electron diffraction: Crystallography of surfaces and interfaces," Bunsenmagazin **12**, 124 (2010).

[33] P. van der Heide, "X-Ray Photoelectron Spectroscopy: An Introduction to Principles and Practices," (Wiley, 2011) Chap. 1 Introduction.

[34] F. Müller, http://jacobs.physik.uni-saarland.de/instrumentation/uhvl.htm, accessed: 2018-02-06.

[35] M. S. J. Marshall and M. R. Castell, "Scanning tunnelling microscopy of epitaxial nanostructures." Chem. Soc. Rev. **43**, 2226 (2014).

[36] G. Binnig, H. Rohrer, C. Gerber, and E. Weibel, "Tunneling through a controllable vacuum gap," Appl. Phys. Lett. **40**, 178 (1982).

[37] G. Binnig and H. Rohrer, "Scanning tunneling microscopy," Surf. Sci. **126**, 236 (1983).

[38] J. A. Stroscio and W. J. Kaiser, eds., *Scanning Tunneling Microscopy* (Academic Press, San Diego, 1993).

[39] "The Opensource Handbook of Nanoscience and Nanotechnology," https://en.wikibooks.org/wiki/Nanotechnology/AFM, accessed: 2018-02-06.

[40] G. Binnig and C. F. Quate, "Atomic Force Microscope," Phys. Rev. Lett. **56**, 930 (1986).

[41] http://www.parkafm.com/index.php/park-spm-modes/91-standard-imaging-mode/223-basic-contact-afm-dynamic-force-microscope-dfm, accessed: 2018-02-06.

[42] R. N. Jagtap and A. H. Ambre, "Overview literature on atomic force microscopy (AFM): Basics and its important applications for polymer characterization," Indian J. Eng. Mater. Sci. **13**, 368 (2006).

[43] H. Ohta, M. Orita, M. Hirano, and H. Hosono, "Surface morphology and crystal quality of low resistive indium tin oxide grown on yittria-stabilized zirconia," J. Appl. Phys. **91**, 3547 (2002).

[44] K. H. L. Zhang, V. K. Lazarov, H. H. Lai, and R. G. Egdell, "Influence of temperature on the epitaxial growth of In_2O_3 thin films," J. Cryst. Growth **318**, 345 (2011).

[45] P. Vogt and O. Bierwagen, "The competing oxide and sub-oxide formation in metal-oxide molecular beam epitaxy," Appl. Phys. Lett. **106**, 081910 (2015).

[46] H. E. Swanson, "Standard X-ray diffraction powder patterns," J. Res. Natl. Bur. Stand. (U. S.) (1955).